

Astronomy 233 Winter 2009

# Physical Cosmology

Week 10

*Cosmic Web*

Joel Primack

University of California, Santa Cruz

# Outline

- Wk8 Cosmic Microwave Background  
GUTs, Cosmic Phase Transitions, Defects
- Wk9 Cosmic Inflation  
Baryogenesis = Generation of Baryon Asymmetry
- Wk10 GUT, ElectroWeak, Leptogenesis, Affleck-Dine

Special SCIPP Astro-Particle Seminar - Tuesday March 10 -  
ISB 310 - 12:30-1:30 pm - Karsten Jedamzik (LPTA,  
Montpellier) - "The Cosmic Lithium Problem(s) and Physics  
beyond the Standard Model"

Several mechanisms have been proposed to understand the baryon asymmetry:

1. **GUT Baryogenesis**. Grand Unified Theories unify the gauge interactions of the strong, weak and electromagnetic interactions in a single gauge group. They inevitably violate baryon number, and they have heavy particles, with mass of order  $M_{\text{GUT}} \approx 10^{16}$  GeV, whose decays can provide a departure from equilibrium. The main objections to this possibility come from issues associated with inflation. While there does not exist a compelling microphysical model for inflation, in most models, the temperature of the universe after reheating is well below  $M_{\text{GUT}}$ . But even if it were very large, there would be another problem. Successful unification requires supersymmetry, which implies that the graviton has a spin-3/2 partner, called the gravitino. In most models for supersymmetry breaking, these particles have masses of order TeV, and are very long lived. Even though these particles are weakly interacting, **too many gravitinos are produced unless the reheating temperature is well below the unification scale -- too low for GUT baryogenesis to occur.**

2. **Electroweak baryogenesis**. The Standard Model satisfies all of the conditions for baryogenesis, but any baryon asymmetry produced is far too small to account for observations. In certain extensions of the Standard Model, it is possible to obtain an adequate asymmetry, but in most cases **the allowed region of parameter space is very small.**

3. **Leptogenesis**. The possibility that the weak interactions will convert some lepton number to baryon number means that if one produces a large lepton number at some stage, this will be processed into a net baryon and lepton number at the electroweak phase transition. **The observation of neutrino masses makes this idea highly plausible.** Many but not all of the relevant parameters can be directly measured.

4. **Production by coherent motion of scalar fields (the Affleck-Dine mechanism)**, which can be highly efficient, **might well be operative if nature is supersymmetric.**

## 2. Electroweak baryogenesis.

Below the electroweak scale of  $\sim 100$  GeV, the **sphaleron** quantum tunneling process that violates B and L conservation (but preserves B - L) in the Standard Model is greatly suppressed, by  $\sim \exp(-2\pi/\alpha_W) \sim 10^{-65}$ . But at  $T \sim 100$  GeV this process can occur. It can satisfy all three Sakharov conditions, but it cannot produce a large enough B and L for baryogenesis. However, it can easily convert L into a mixture of B and L (**Leptogenesis**). Here's an introduction to sphalerons:

When one quantizes the Standard Model, one finds that the baryon number current is not exactly conserved, but rather satisfies

$$\partial_\mu j_B^\mu = \frac{3}{16\pi^2} F_{\mu\nu}^a \tilde{F}_{\mu\nu}^a = \frac{3}{8\pi^2} \text{Tr} F_{\mu\nu} \tilde{F}_{\mu\nu}.$$

The same parity-violating term occurs in the divergence of the lepton number current, so the difference (the B - L current) is exactly conserved. The parity-violating term is a total divergence

$$\text{Tr} F_{\mu\nu} \tilde{F}_{\mu\nu} = \partial_\mu K^\mu \quad \text{where} \quad K^\mu = \epsilon^{\mu\nu\rho\sigma} \text{tr} [F_{\nu\rho} A_\sigma + \frac{2}{3} A_\nu A_\rho A_\sigma] \quad , \quad \text{so}$$

$$\tilde{j} = j_B^\mu - \frac{3g^2}{8\pi^2} K^\mu \quad \text{is conserved. In perturbation theory (i.e., Feynman diagrams)}$$

$K^\mu$  falls to zero rapidly at infinity, so B and L are conserved.

In abelian -- i.e. U(1) -- gauge theories, this is the end of the story. In non-abelian theories, however, there are non-perturbative field configurations, called instantons, which lead to violations of B and L. They correspond to calculation of a tunneling amplitude. To understand what the tunneling process is, one must consider more carefully the ground state of the field theory. Classically, the ground states are field configurations for which the energy vanishes. The trivial solution of this condition is  $A = 0$ , where  $A$  is the vector potential, which is the only possibility in U(1). But a “pure gauge” is also a solution, where

$$\vec{A} = \frac{1}{i} g^{-1} \vec{\nabla} g,$$

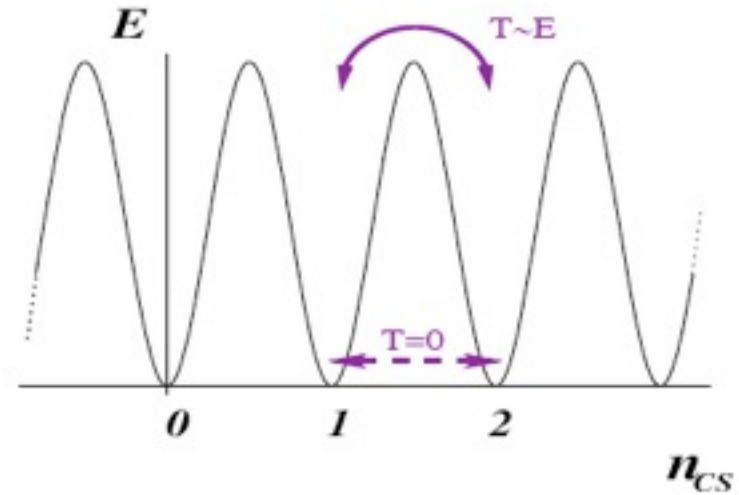
where  $g$  is a gauge transformation matrix. There is a class of gauge transformations  $g$ , labeled by a discrete index  $n$ , which must also be considered. These have the form

$$g_n(\vec{x}) = e^{in f(\vec{x}) \hat{x} \cdot \tau / 2} \quad \text{where } f(x) \rightarrow 2\pi \text{ as } \vec{x} \rightarrow \infty, \text{ and } f(\vec{x}) \rightarrow 0 \text{ as } \vec{x} \rightarrow 0.$$

The ground states are labeled by the index  $n$ . If we evaluate the integral of the current  $K^\mu$  we obtain a quantity known as the Chern-Simons number

$$n_{CS} = \frac{1}{16\pi^2} \int d^3x K^0 = \frac{2/3}{16\pi^2} \int d^3x \epsilon_{ijk} \text{Tr}(g^{-1} \partial_i g g^{-1} \partial_j g g^{-1} \partial_k g). \quad \text{For } g = g_n, n_{CS} = n.$$

Schematic Yang-Mills vacuum structure. At zero temperature, the instanton transitions between vacua with different Chern-Simons numbers are suppressed. At finite temperature, these transitions can proceed via [sphalerons](#).



In tunneling processes which change the Chern-Simons number, because of the anomaly, the baryon and lepton numbers will change. The exponential suppression found in the instanton calculation is typical of tunneling processes, and in fact the instanton calculation is nothing but a field-theoretic WKB calculation. The probability that a single proton has decayed through this process in the history of the universe is infinitesimal. But this picture suggests that, at finite temperature, the rate should be larger. One can determine the height of the barrier separating configurations of different  $n_{CS}$  by looking for the field configuration which corresponds to sitting on top of the barrier. This is a solution of the static equations of motion with finite energy. It is known as a “[sphaleron](#)”. It follows that when the temperature is of order the ElectroWeak scale  $\sim 100$  GeV, B and L violating (but B - L conserving) processes can proceed rapidly.

This result leads to three remarks:

1. If in the early universe, one creates baryon and lepton number, but no net  $B - L$ ,  $B$  and  $L$  will subsequently be lost through sphaleron processes.
2. If one creates a net  $B - L$  (e.g. creates a lepton number) the sphaleron process will leave both baryon and lepton numbers comparable to the original  $B - L$ . This realization is crucial to the idea of Leptogenesis.
3. The Standard Model satisfies, by itself, all of the conditions for baryogenesis. However, detailed calculations show that in the Standard Model the size of the baryon and lepton numbers produced are much too small to be relevant for cosmology, both because the Higgs boson is more massive than  $\sim 80$  GeV and because the CKM CP violation is much too small. In supersymmetric extensions of the Standard Model it is possible that a large enough matter-antimatter asymmetry might be generated, but the parameter space for this is extremely small. (See Dine and Kusenko for details and references.)

This leaves Leptogenesis and Affleck-Dine baryogenesis as the two most promising possibilities. What is exciting about each of these is that, if they are operative, they have consequences for experiments which will be performed at accelerators over the next few years.

### 3. Leptogenesis.

There is now compelling experimental evidence that neutrinos have mass, both from solar and atmospheric neutrino experiments and accelerator and reactor experiments. The masses are tiny, fractions of an eV. The “see-saw mechanism” is a natural way to generate such masses. One supposes that in addition to the neutrinos of the Standard Model, there are some SU(2)xU(1)-singlet neutrinos, N. Nothing forbids these from obtaining a large mass. This could be of order  $M_{\text{GUT}}$ , for example, or a bit smaller. These neutrinos could also couple to the left handed doublets  $\nu_L$ , just like right handed charged leptons. Assuming that these couplings are not particularly small, one would obtain a mass matrix, in the  $\{N, \nu_L\}$  basis, of the form

$$M_\nu = \begin{pmatrix} M & M_W \\ M_W^T & 0 \end{pmatrix}$$

This matrix has an eigenvalue  $\frac{M_W^2}{M}$ .

The latter number is of the order needed to explain the neutrino anomaly for  $M \sim 10^{13}$  or so, i.e. not wildly different than the GUT scale and other scales which have been proposed for new physics. For **leptogenesis** (Fukugita and Yanagida, 1986), what is important in this model is that the couplings of N break lepton number. N is a heavy particle; it can decay both to  $h + \nu$  and  $h + \bar{\nu}$ , for example. The partial widths to each of these final states need not be the same. CP violation can enter through phases in the Yukawa couplings and mass matrices of the N's.



As the universe cools through temperatures of order the of masses of the  $N$ 's, they drop out of equilibrium, and their decays can lead to an excess of neutrinos over antineutrinos. Detailed predictions can be obtained by integrating a suitable set of Boltzmann equations. These decays produce a net lepton number, but not baryon number (and hence a net  $B - L$ ). The resulting lepton number will be further processed by sphaleron interactions, yielding a net lepton and baryon number (recall that sphaleron interactions preserve  $B - L$ , but violate  $B$  and  $L$  separately). Reasonable values of the neutrino parameters give asymmetries of the order we seek to explain.

It is interesting to ask: assuming that these processes are the source of the observed asymmetry, how many parameters which enter into the computation can be measured, i.e. can we relate the observed number to microphysics. It is likely that, over time, many of the parameters of the light neutrino mass matrices, including possible CP-violating effects, will be measured. But while these measurements determine some of the couplings and masses, they are not, in general, enough. In order to give a precise calculation, analogous to the calculations of nucleosynthesis, of the baryon number density, one needs additional information about the masses of the fields  $N$ . One either requires some other (currently unforeseen) experimental access to this higher scale physics, or a compelling theory of neutrino mass in which symmetries, perhaps, reduce the number of parameters.

#### 4. Production by coherent motion of scalar fields (the Affleck-Dine mechanism)

The formation of an AD condensate can occur quite generically in cosmological models. Also, the AD scenario potentially can give rise simultaneously to the ordinary matter and the dark matter in the universe. This can explain why the amounts of luminous and dark matter are surprisingly close to each other, within one order of magnitude. If the two entities formed in completely unrelated processes (for example, the baryon asymmetry from leptogenesis, while the dark matter from freeze-out of neutralinos), the observed relation  $\Omega_{\text{DM}} \sim \Omega_{\text{baryon}}$  is fortuitous.

In supersymmetric theories, the ordinary quarks and leptons are accompanied by scalar fields. These scalar fields carry baryon and lepton number. A coherent field, i.e., a large classical value of such a field, can in principle carry a large amount of baryon number. As we will see, it is quite plausible that such fields were excited in the early universe. To understand the basics of the mechanism, consider first a model with a single complex scalar field. Take the Lagrangian to be

$$\mathcal{L} = |\partial_\mu \phi|^2 - m^2 |\phi|^2$$

This Lagrangian has a symmetry,  $\phi \rightarrow e^{i\alpha\phi}$ , and a corresponding conserved current, which we will refer to as baryon current:

$$j_B^\mu = i(\phi^* \partial^\mu \phi - \phi \partial^\mu \phi^*).$$

It also possesses a “CP” symmetry:  $\phi \leftrightarrow \phi^*$ . With supersymmetry in mind, we will think of  $m$  as of order  $M_W$ .

Let us add interactions in the following way, which will closely parallel what happens in the supersymmetric case. Include a set of quartic couplings:

$$\mathcal{L}_I = \lambda|\phi|^4 + \epsilon\phi^3\phi^* + \delta\phi^4 + c.c.$$

These interactions clearly violate B. For general complex  $\epsilon$  and  $\delta$ , they also violate CP. In supersymmetric theories, as we will shortly see, the couplings will be extremely small. In order that these tiny couplings lead to an appreciable baryon number, it is necessary that the fields, at some stage, were very large.

To see how the cosmic evolution of this system can lead to a non-zero baryon number, first note that at very early times, when the Hubble constant,  $H \gg m$ , the mass of the field is irrelevant. It is thus reasonable to suppose that at this early time  $\phi = \phi_0 \gg 0$ . How does the field then evolve? First ignore the quartic interactions. In the expanding universe, the equation of motion for the field is as usual

$$\ddot{\phi} + 3H\dot{\phi} + \frac{\partial V}{\partial \phi} = 0.$$

At very early times,  $H \gg m$ , and so the system is highly overdamped and essentially frozen at  $\phi_0$ . At this point,  $B = 0$ .

Once the universe has aged enough that  $H \ll m$ ,  $\phi$  begins to oscillate. Substituting  $H = 1/2 t$  or  $H = 2/3 t$  for the radiation and matter dominated eras, respectively, one finds that

$$\phi = \begin{cases} \frac{\phi_o}{(mt)^{3/2}} \sin(mt) & \text{(radiation)} \\ \frac{\phi_o}{(mt)} \sin(mt) & \text{(matter)}. \end{cases}$$

In either case, the energy behaves, in terms of the scale factor,  $R(t)$ , as

$$E \approx m^2 \phi_o^2 \left( \frac{R_o}{R} \right)^3$$

Now let's consider the effects of the quartic couplings. Since the field amplitude damps with time, their significance will decrease with time. Suppose, initially, that  $\phi = \phi_o$  is real. Then the imaginary part of  $\phi$  satisfies, in the approximation that  $\epsilon$  and  $\delta$  are small,

$$\ddot{\phi}_i + 3H\dot{\phi}_i + m^2\phi_i \approx \text{Im}(\epsilon + \delta)\phi_r^3.$$

For large times, the right hand falls as  $t^{-9/2}$ , whereas the left hand side falls off only as  $t^{-3/2}$ . As a result, baryon number violation becomes negligible. The equation goes over to the free equation, with a solution of the form

$$\phi_i = a_r \frac{\text{Im}(\epsilon + \delta)\phi_o^3}{m^2(mt)^{3/4}} \sin(mt + \delta_r) \quad \text{(radiation)}, \quad \phi_i = a_m \frac{\text{Im}(\epsilon + \delta)\phi_o^3}{m^3t} \sin(mt + \delta_m) \quad \text{(matter)},$$

The constants can be obtained numerically, and are of order unity

$$a_r = 0.85 \quad a_m = 0.85 \quad \delta_r = -0.91 \quad \delta_m = 1.54.$$

But now we have a non-zero baryon number; substituting in the expression for the current,

$$n_B = 2a_r \text{Im}(\epsilon + \delta) \frac{\phi_o^2}{m(mt)^2} \sin(\delta_r + \pi/8) \quad (\text{radiation})$$

$$n_B = 2a_m \text{Im}(\epsilon + \delta) \frac{\phi_o^2}{m(mt)^2} \sin(\delta_m) \quad (\text{matter}).$$

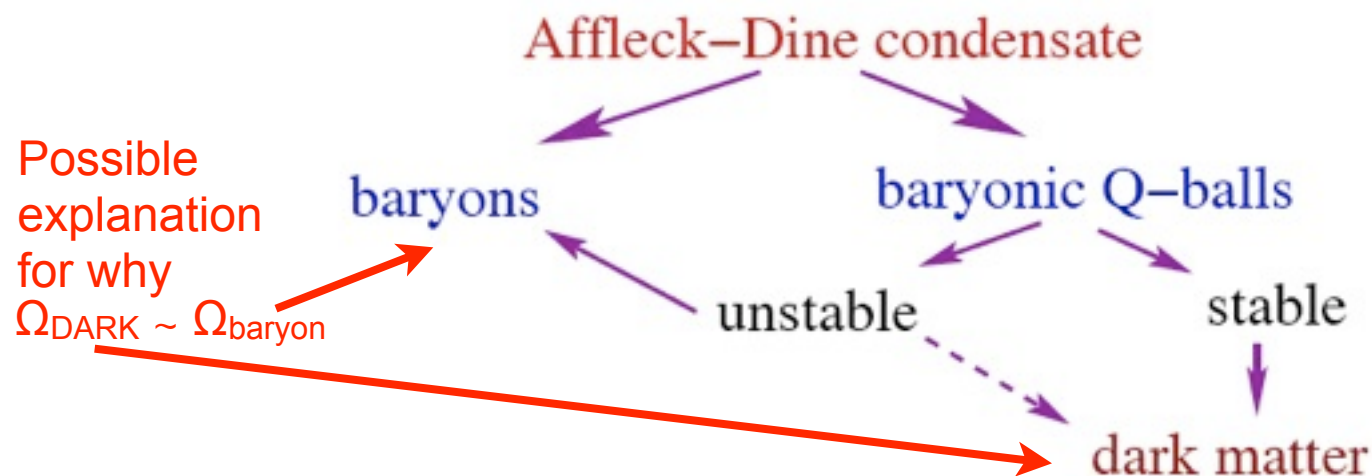
Two features of these results should be noted. First, if  $\epsilon$  and  $\delta$  vanish,  $n_B$  vanishes. If they are real, and  $\phi_o$  is real,  $n_B$  vanishes. It is remarkable that the Lagrangian parameters can be real, and yet  $\phi_o$  can be complex, still giving rise to a net baryon number. Supersymmetry breaking in the early universe can naturally lead to a very large value for a scalar field carrying B or L. Finally, as expected,  $n_B$  is conserved at late times.

This mechanism for generating baryon number could be considered without supersymmetry. In that case, it begs several questions:

- What are the scalar fields carrying baryon number?
- Why are the  $\phi^4$  terms so small?
- How are the scalars in the condensate converted to more familiar particles?

In the context of supersymmetry, there is a natural answer to each of these questions. First, there are scalar fields (squarks and sleptons) carrying baryon and lepton number. Second, in the limit that supersymmetry is unbroken, there are typically directions in the field space in which the quartic terms in the potential vanish. Finally, the scalar quarks and leptons will be able to decay (in a baryon and lepton number conserving fashion) to ordinary quarks.

In addition to topologically stable solutions to the field equations such as strings or monopoles, it is sometimes also possible to find non-topological solutions, called Q-balls, which can form as part of the Affleck-Dine condensate. These are usually unstable and could decay to the dark matter, but in some theories they are stable and could be the dark matter. The various possibilities are summarized as follows:



The parameter space of the MSSM consistent with LSP dark matter is very different, depending on whether the LSPs froze out of equilibrium or were produced from the evaporation of AD baryonic Q-balls. If supersymmetry is discovered, one will be able to determine the properties of the LSP experimentally. This will, in turn, provide some information on the how the dark-matter SUSY particles could be produced. The discovery of a Higgsino-like LSP would be a evidence in favor of Affleck-Dine baryogenesis. This is a way in which we might be able to establish the origin of matter-antimatter asymmetry.

## Review of mechanisms that have been proposed to generate the baryon asymmetry:

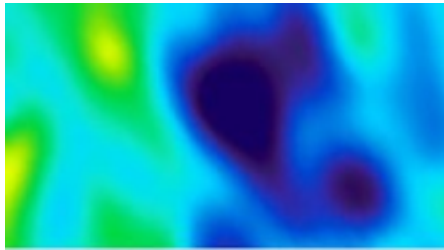
1. **GUT Baryogenesis.** Grand Unified Theories unify the gauge interactions of the strong, weak and electromagnetic interactions in a single gauge group. They inevitably violate baryon number, and they have heavy particles, with mass of order  $M_{\text{GUT}} \approx 10^{16}$  GeV, whose decays can provide a departure from equilibrium. The main objections to this possibility come from issues associated with inflation. While there does not exist a compelling microphysical model for inflation, in most models, the temperature of the universe after reheating is well below  $M_{\text{GUT}}$ . But even if it were very large, there would be another problem. Successful unification requires supersymmetry, which implies that the graviton has a spin-3/2 partner, called the gravitino. In most models for supersymmetry breaking, these particles have masses of order TeV, and are very long lived. Even though these particles are weakly interacting, **too many gravitinos are produced unless the reheating temperature is well below the unification scale -- too low for GUT baryogenesis to occur.**

2. **Electroweak baryogenesis.** The Standard Model satisfies all of the conditions for baryogenesis, but any baryon asymmetry produced is far too small to account for observations. In certain extensions of the Standard Model, it is possible to obtain an adequate asymmetry, but in most cases **the allowed region of parameter space is very small.**

3. **Leptogenesis.** The possibility that the weak interactions will convert some lepton number to baryon number means that if one produces a large lepton number at some stage, this will be processed into a net baryon and lepton number at the electroweak phase transition. **The observation of neutrino masses makes this idea highly plausible.** Many but not all of the relevant parameters can be directly measured.

4. **Production by coherent motion of scalar fields (the Affleck-Dine mechanism),** which can be highly efficient, **might well be operative if nature is supersymmetric.**

# Late Cosmological Epochs



380 kyr  $z \sim 1000$

recombination  
last scattering



dark ages



$\sim 100$  Myr  $z \sim 30$

first stars

$\sim 480$  Myr  $z \sim 10$

reionization



galaxy formation



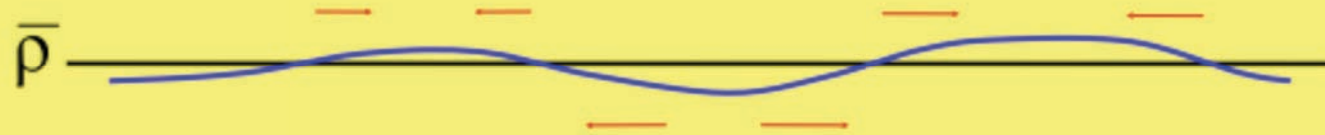
13.7 Gyr  $z=0$

today

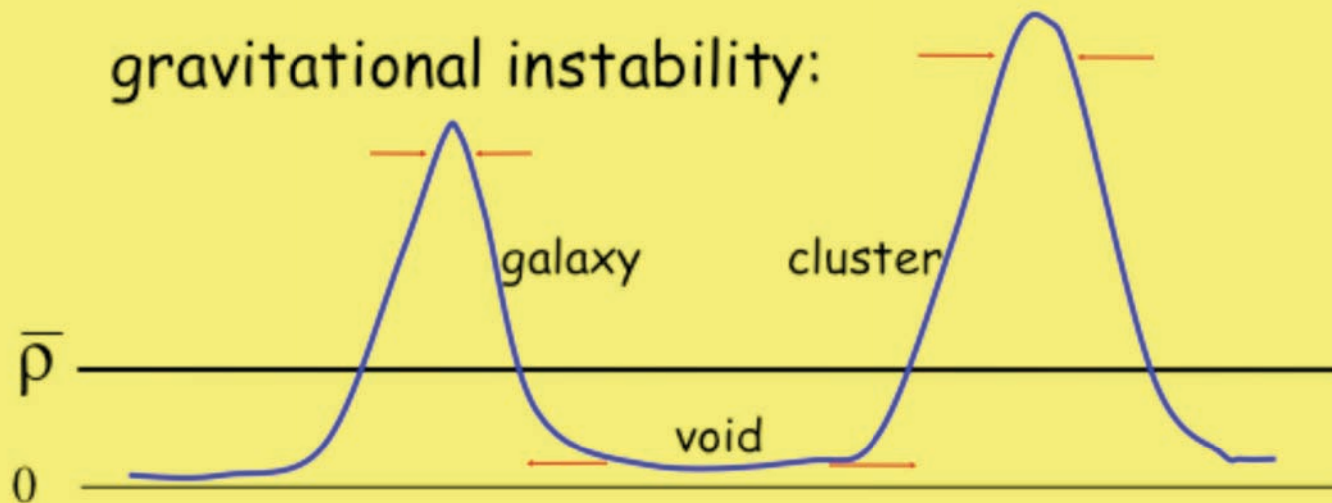


# Gravitational instability

small-amplitude fluctuations:



gravitational instability:



# FLUCTUATIONS: LINEAR THEORY

## "TOP HAT" MODEL

MASS CONS.  $\Rightarrow$

$$\rho_m (1+\delta) R^3 (1+a)^3 = \text{const.} \Rightarrow$$

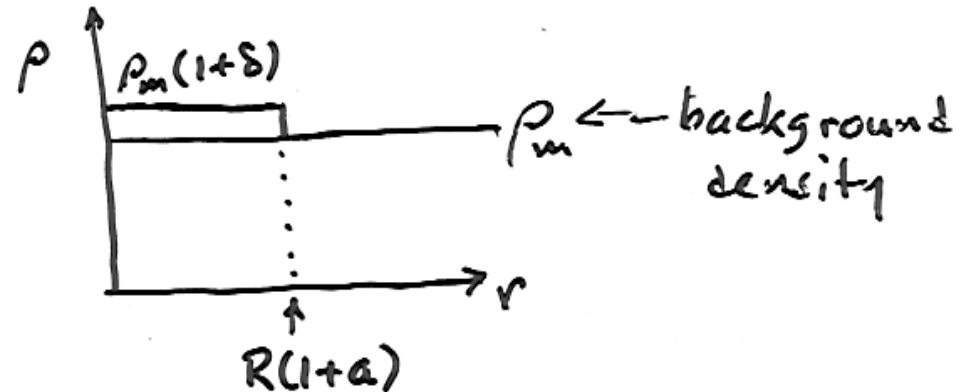
$$\delta = -3a$$

GRAVITY:  $\ddot{R} = -\frac{4\pi G}{3} (\rho + 3p) R$

$$\ddot{\delta} + 2\frac{\dot{R}}{R}\dot{\delta} = 4\pi G \rho_m \delta$$

RAD ERA  $\dot{R}/R = \frac{1}{2}t^{-1}$ ,

MATTER ERA  $= \frac{2}{3}t^{-1}$ ,



APPLIED BOTH TO FLUCT. + BCG.  $\Rightarrow$

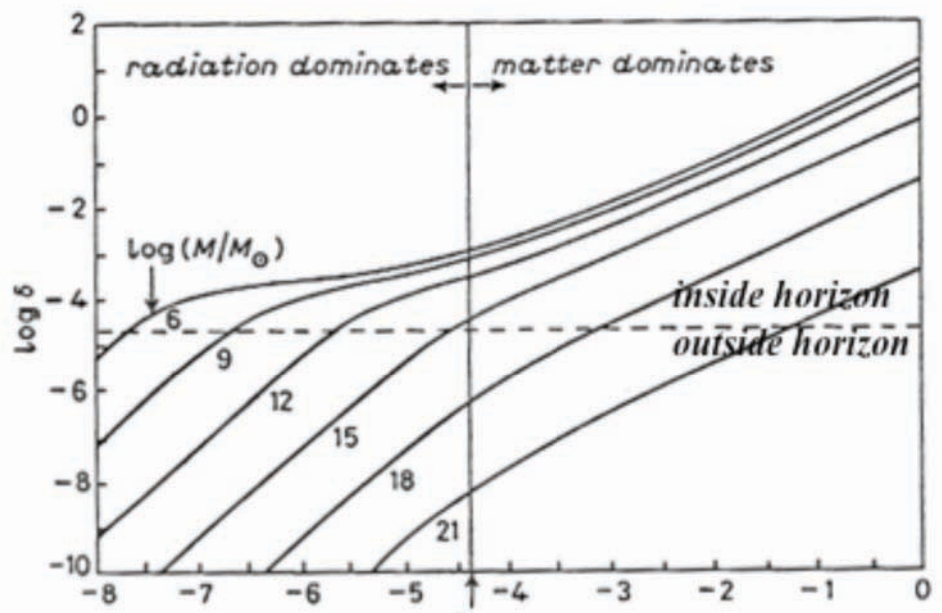
Try  $\delta = t^\alpha$

$$\delta = At + Bt^{-1} = \underline{AR^2} + BR^{-2}$$

$$\delta = At^{2/3} + Bt^{-1} = \underline{AR} + BR^{-3/2}$$

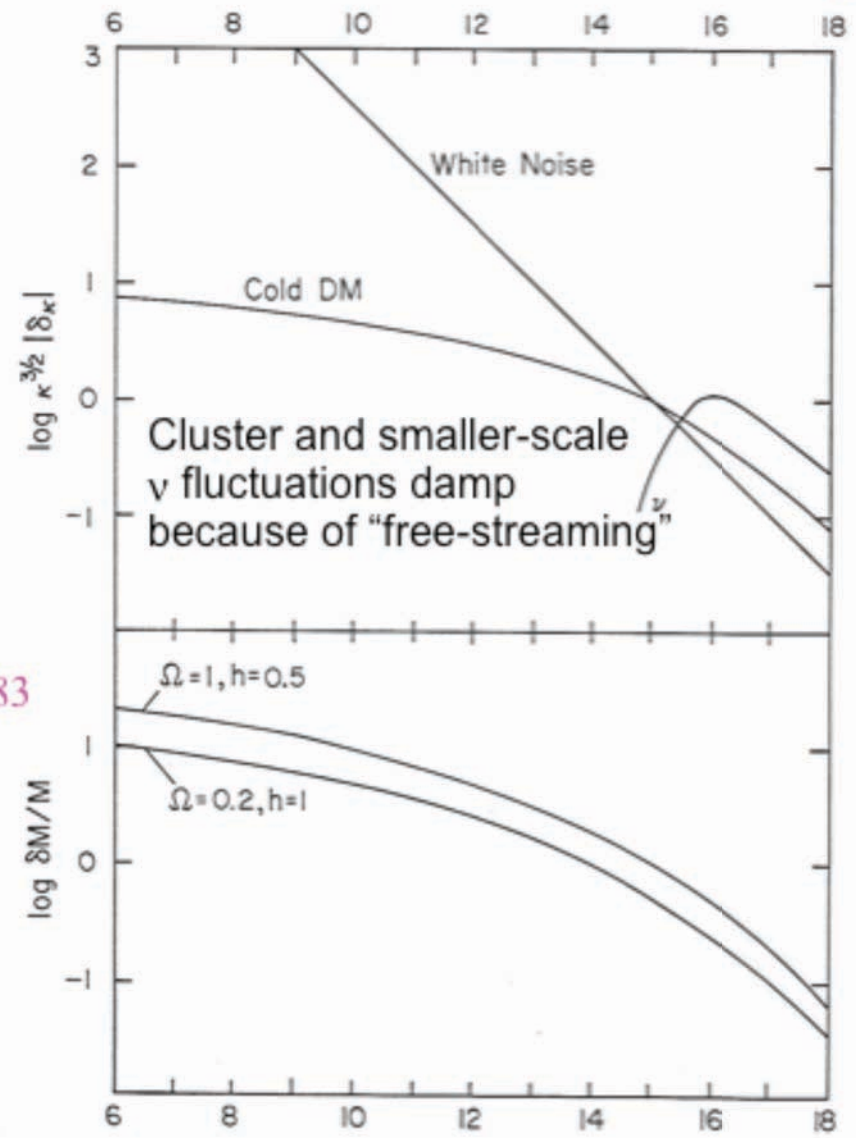
**GROWING MODE**

# CDM Structure Formation: Linear Theory



$\log a$  Primack & Blumenthal 1983

Matter fluctuations that enter the horizon during the radiation dominated era, with masses less than about  $10^{15} M_{\odot}$ , grow only  $\propto \log a$ , because they are not in the gravitationally dominant component. But matter fluctuations that enter the horizon in the matter-dominated era grow  $\propto a$ . This explains the characteristic shape of the CDM fluctuation spectrum, with  $\delta(k) \propto k^{-n/2-2} \log k$  for  $k \gg k_{eq}$ .



$\log M/M_{\odot}$  Blumenthal, Faber, Primack, & Rees 1984

# The Initial Fluctuations

At Inflation: Gaussian, adiabatic

Fourier transform:

$$\delta(\vec{x}) = \sum_{\vec{k}} \delta_{\vec{k}} e^{i\vec{k}\cdot\vec{x}}$$

Power Spectrum:

$$P(k) \equiv \langle |\tilde{\delta}(\vec{k})|^2 \rangle \propto k^n$$

rms perturbation:

$$\delta_{rms} = \langle \delta^2 \rangle^{1/2} \propto \int_{k=0}^{k_{max}} P_k d^3k \propto M^{-(n+3)/6}$$

Correlation function:

$$\xi(r) \equiv \langle \delta(\vec{x})\delta(\vec{x}+\vec{r}) \rangle \propto \int |\tilde{\delta}(\vec{k})|^2 e^{-i\vec{k}\cdot\vec{r}} d^3k \propto r^{-(n+3)}$$

$$dP = [1 + \xi(r)] n dV$$

# Gravitational Instability

Small fluctuations:  $\delta, v, \varphi$  ( $x, t$ ) comoving coordinates

$$r = a(t)x \text{ etc.}$$

Continuity:

$$\dot{\delta} + \nabla \cdot v + \nabla \cdot (v\delta) = 0$$

$$H \equiv \dot{a}/a, \quad \Omega(t)$$

Euler:

$$\dot{v} + 2Hv + (v \times \nabla)v = -\nabla\varphi$$

matter era

Poisson:

$$\nabla^2\varphi = (3/2)H^2\Omega\delta$$

Linear approximation:

$$\ddot{\delta} + 2H\dot{\delta} = (3/2)H^2\Omega\delta$$

growing mode:

$$\delta \propto D(t) = t^{2/3} \xrightarrow{\Omega_m \rightarrow 0} t^0$$

$$\delta \equiv -\nabla \cdot v / [Hf(\Omega)]$$

$$f(\Omega) \equiv \dot{D}/(HD) \approx \Omega^{0.6}$$

irrotational, potential flow:

$$\nabla \times v = 0 \quad v = -\nabla\varphi_v$$

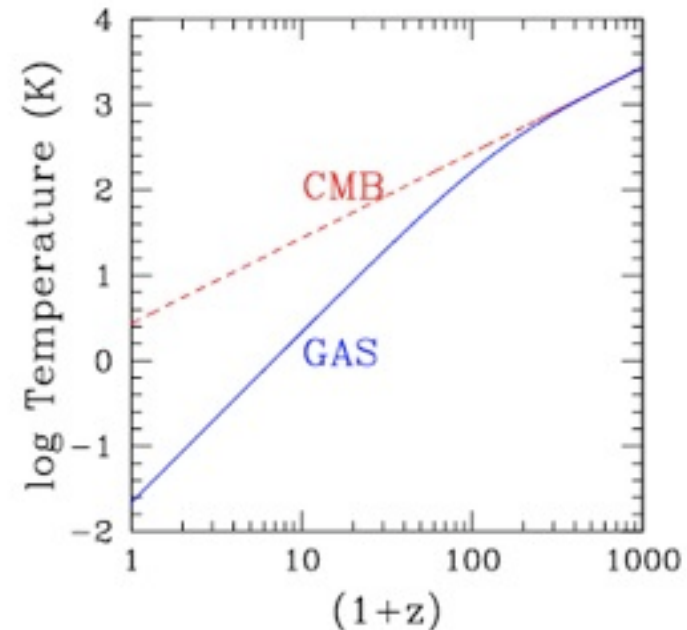
Thus far, we have considered only the evolution of fluctuations in the dark matter. But of course we have to consider also the ordinary matter, known in cosmology as “baryons” (implicitly including the electrons). See Madau’s lectures “The Astrophysics of Early Galaxy Formation (<http://arxiv.org/abs/0706.0123v1> ) for a recent summary. We have already seen that the baryons are primarily in the form of atoms after  $z \sim 1000$ , with a residual ionization fraction of a few  $\times 10^{-4}$ . They become fully reionized by  $z \sim 6$ , but they were not reionized at  $z \sim 20$  since the COBE satellite found that “Compton parameter”  $y \leq 1.5 \times 10^{-5}$ , where

$$y = \int_0^z \frac{k_B T_e}{m_e c^2} \frac{d\tau_e}{dz} dz$$

This implies that  $\langle x_e T_e \rangle [(1+z)^{3/2} - 1] < 4 \times 10^7$  K. Thus, for example, a universe that was reionized and reheated at  $z = 20$  to  $(x_e, T_e) = (1, > 4 \times 10^5$  K) would violate the COBE  $y$ -limit.

The figure at right shows the evolution of the radiation (dashed line, labeled **CMB**) and matter (solid line, labeled **GAS**) temperatures after recombination, in the absence of any reheating mechanism.

(From Madau’s lectures.)



The linear evolution of sub-horizon density perturbations in the dark matter-baryon fluid is governed in the matter-dominated era by two second-order differential equations:

$$\ddot{\delta}_{\text{dm}} + 2H\dot{\delta}_{\text{dm}} = \frac{3}{2}H^2\Omega_m^z (f_{\text{dm}}\delta_{\text{dm}} + f_b\delta_b) \quad (1)$$

for the dark matter, and

$$\ddot{\delta}_b + 2H\dot{\delta}_b = \frac{3}{2}H^2\Omega_m^z (f_{\text{dm}}\delta_{\text{dm}} + f_b\delta_b) - \frac{c_s^2}{a^2}k^2\delta_b$$

for the baryons, where  $\delta_{\text{dm}}(\mathbf{k})$  and  $\delta_b(\mathbf{k})$  are the Fourier components of the density fluctuations in the dark matter and baryons,  $f_{\text{dm}}$  and  $f_b$  are the corresponding mass fractions,  $c_s$  is the gas sound speed,  $k$  is the (comoving) wavenumber, and the derivatives are taken with respect to cosmic time. Here

$$\Omega_m^z \equiv 8\pi G\rho(t)/3H^2 = \Omega_m(1+z)^3/[\Omega_m(1+z)^3 + \Omega_\Lambda] \quad (2)$$

is the time-dependent matter density parameter, and  $\rho(t)$  is the total background matter density. Because there is  $\sim 5$  times more dark matter than baryons, it is the former that defines the pattern of gravitational wells in which structure formation occurs. In the case where  $f_b \approx 0$  and the universe is static ( $H = 0$ ), equation (1) above becomes

† For each fluid component ( $i = b, \text{dm}$ ) the real space fluctuation in the density field,

$\delta_i(\mathbf{x}) \equiv \delta\rho_i(\mathbf{x})/\rho_i$ , can be written as a sum over Fourier modes,

$$\delta_i(\mathbf{x}) = \int d^3\mathbf{k} (2\pi)^{-3} \delta_i(\mathbf{k}) \exp i\mathbf{k}\cdot\mathbf{x}.$$

$$\ddot{\delta}_{\text{dm}} = 4\pi G\rho\delta_{\text{dm}} \equiv \frac{\delta_{\text{dm}}}{t_{\text{dyn}}^2},$$

where  $t_{\text{dyn}}$  denotes the dynamical timescale. This equation admits solution

$$\delta_{\text{dm}} = A_1 \exp(t/t_{\text{dyn}}) + A_2 \exp(-t/t_{\text{dyn}}).$$

After a few dynamical times, only the exponentially growing term is significant: gravity tends to make small density fluctuations in a static pressureless medium grow exponentially with time. Sir James Jeans (1902) was the first to discuss this.

The additional term  $\neq H\dot{\delta}_{\text{dm}}$  present in an expanding universe can be thought as a “**Hubble friction**” term that acts to slow down the growth of density perturbations. Equation (1) admits the general solution for the growing mode:

$$\delta_{\text{dm}}(a) = \frac{5\Omega_m}{2} H_0^2 H \int_0^a \frac{da'}{(\dot{a}')^3}, \quad (3)$$

so that an Einstein-de Sitter universe gives the familiar scaling  $\delta_{\text{dm}}(a) = a$  with coefficient unity. The right-hand side of equation (3) is called the linear growth factor  $D(a) = D_+(a)$ . Different values of  $\Omega_m$ ,  $\Omega_\Lambda$  lead to different linear growth factors.

Growing modes actually decrease in density, but not as fast as the average universe. Note how, in contrast to the exponential growth found in the static case, the growth of perturbations even in the case of an Einstein-de Sitter ( $\Omega_m = 1$ ) universe is just algebraic. This was discovered by the Russian physicist Lifshitz (1946).



Since cosmological curvature is at most marginally important at the present epoch, it was negligible during the radiation-dominated era and at least the beginning of the matter-dominated era. But for  $k = -1$ , i.e.  $\Omega < 1$ , the growth of  $\delta$  slows for  $(R/R_o) \gtrsim \Omega_o$ , as gravity becomes less important and the universe begins to expand freely. To discuss this case, it is convenient to introduce the variable

$$x \equiv \Omega^{-1}(t) - 1 = (\Omega_o^{-1} - 1)R(t)/R_o. \quad (2.55)$$

(Note that  $\Omega(t) \rightarrow 1$  at early times.) The general solution in the matter-dominated era is then (Peebles, 1980, §11)

$$\delta = \tilde{A}D_1(t) + \tilde{B}D_2(t), \quad (2.56)$$

where the growing solution is

$$D_1 = 1 + \frac{3}{x} + \frac{3(1+x)^{1/2}}{x^{3/2}} \ln \left[ (1+x)^{1/2} - x^{1/2} \right] \quad (2.57)$$

and the decaying solution is

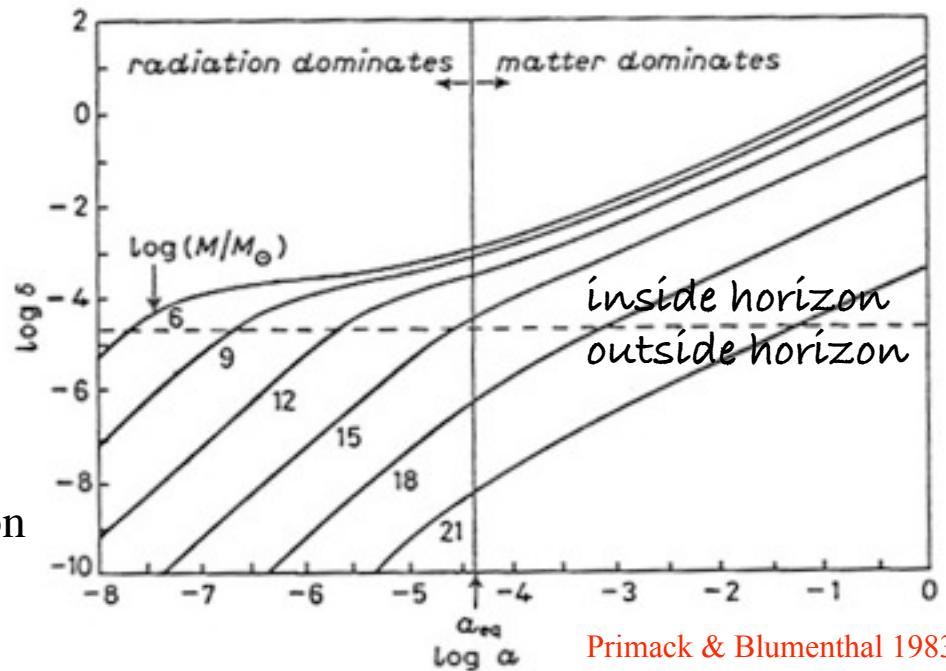
$$D_2 = (1+x)^{1/2}/x^{3/2}. \quad (2.58)$$

These agree with the Einstein-de Sitter results (2.53) at early times ( $t \ll t_o, x \ll 1$ ). For late times ( $t \gg t_o, x \gg 1$ ) the solutions approach

$$D_1 = 1, D_2 = x^{-1}; \quad (2.59)$$

in this limit the universe is expanding freely and the amplitude of fluctuations stops growing.

The consequence is that dark matter fluctuations grow proportionally to the scale factor  $a(t)$  when matter is the dominant component of the universe, but only logarithmically when radiation is dominant. Thus there is not much difference in the amplitudes of fluctuations of mass  $M < 10^{15} M_{\text{sun}}$ , which enter the horizon before  $z_{\text{mr}} \sim 4 \times 10^3$ , while there is a stronger dependence on  $M$  for fluctuations with  $M > 10^{15} M_{\text{sun}}$ .

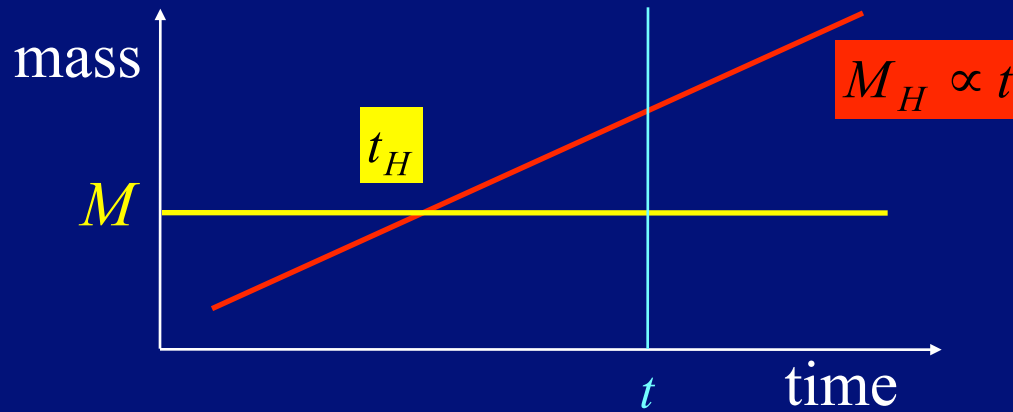


There is a similar suppression of the growth of matter fluctuations once the gravitationally dominant component of the universe is the dark energy, for example a cosmological constant. Lahav, Lilje, Primack, & Rees (1991) showed that the growth factor in this case is well approximated by

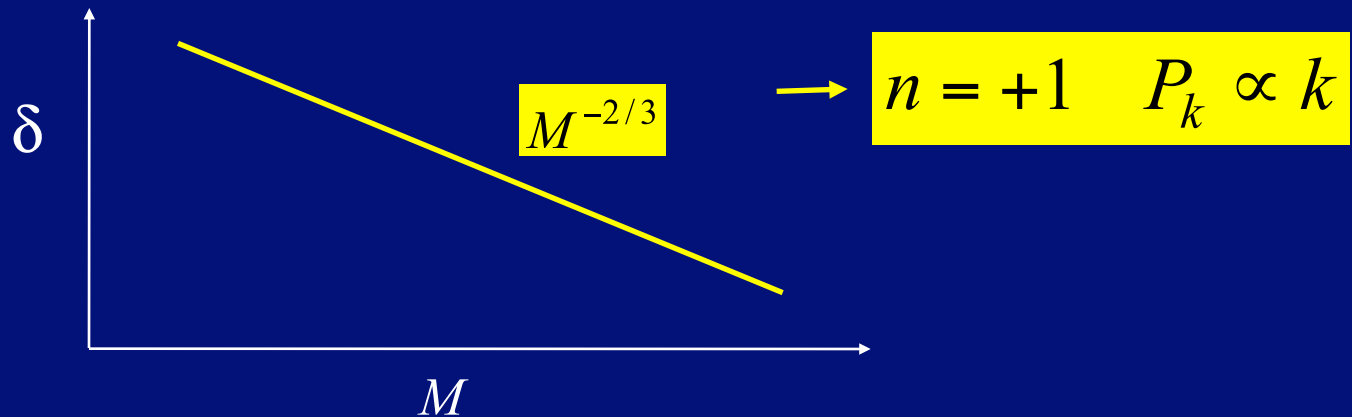
$$\delta_{\text{dm}}(a) = D(a) \simeq \frac{5\Omega_m^z}{2(1+z)} \left[ (\Omega_m^z)^{4/7} - \frac{(\Omega_m^z)^2}{140} + \frac{209}{140}\Omega_m^z + \frac{1}{70} \right]^{-1}.$$

Here  $\Omega_m^z$  is again given by  $\Omega_m^z \equiv 8\pi G\rho(t)/3H^2 = \Omega_m(1+z)^3/[\Omega_m(1+z)^3 + \Omega_\Lambda]$

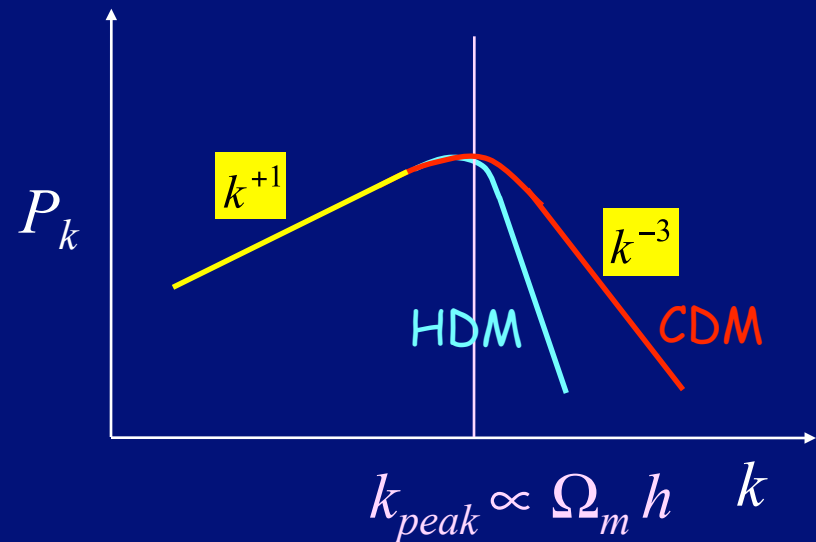
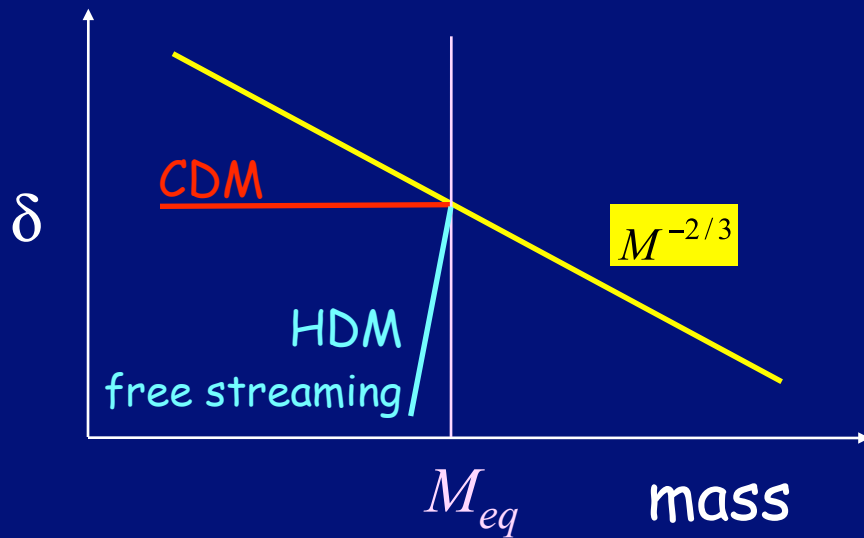
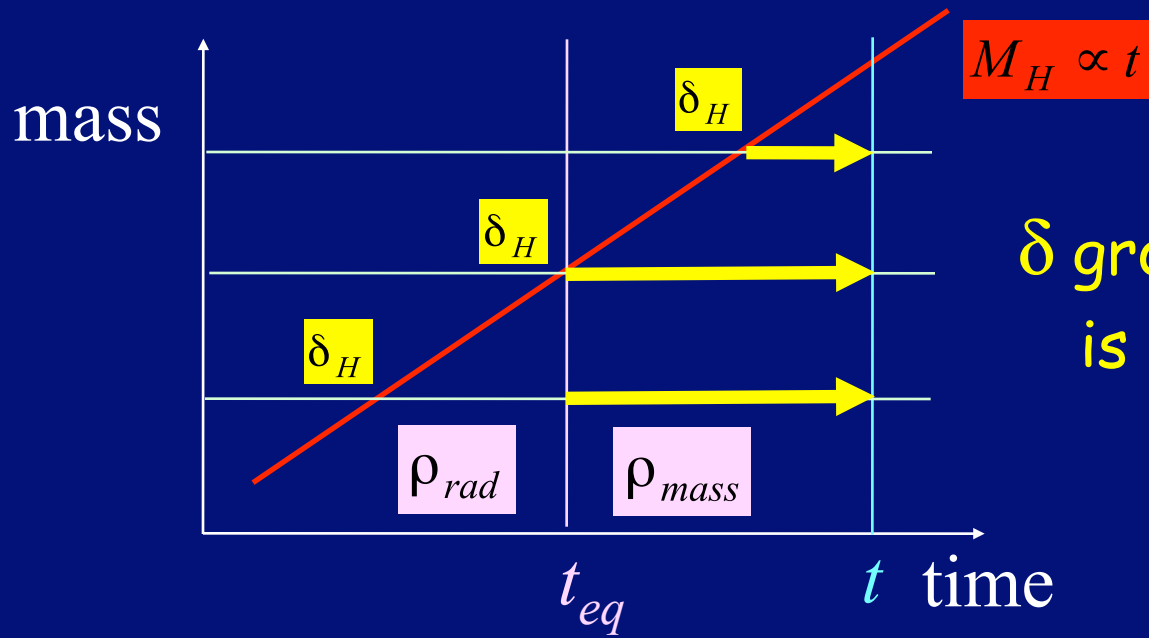
# Scale-Invariant Spectrum (Harrison-Zel'dovich)



$$\delta(M, t) = \delta_H \left( \frac{t}{t_H(M)} \right)^{2/3} \propto M^{-2/3} t^{2/3}$$



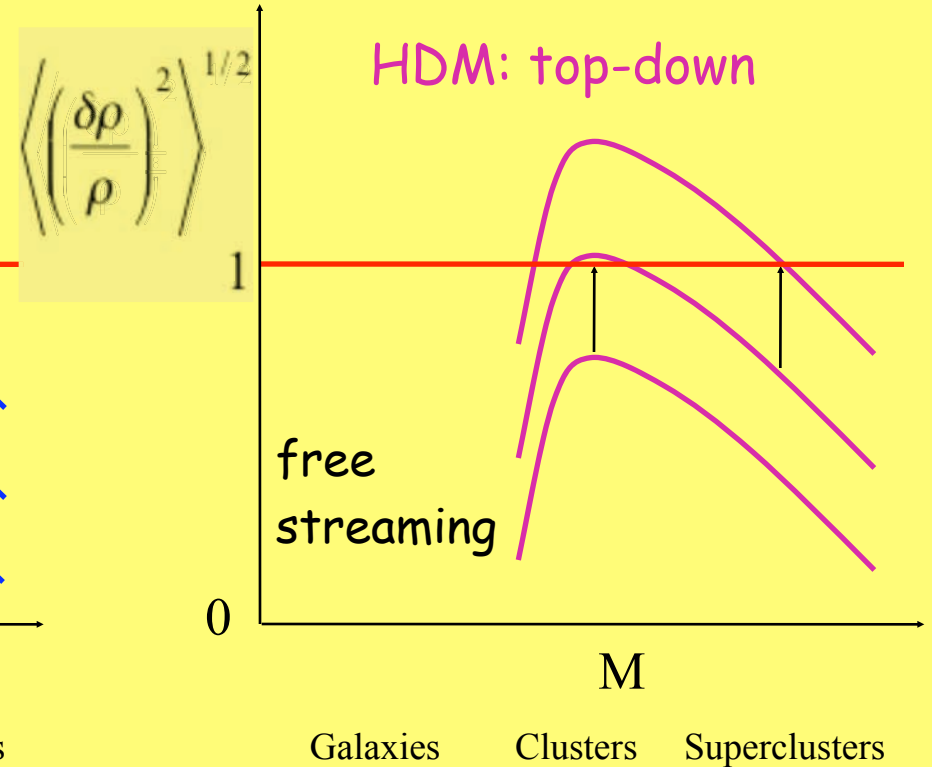
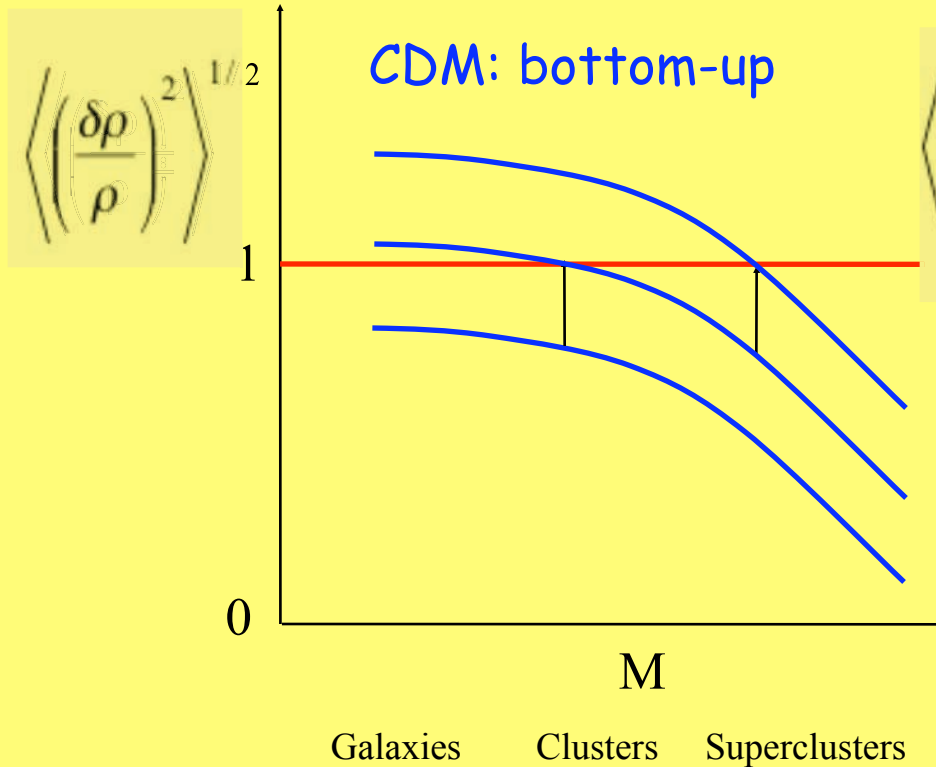
# CDM Power Spectrum



# Formation of Large-Scale Structure

Fluctuation growth in the linear regime:  $\delta \ll 1 \rightarrow \delta \propto t^{2/3}$

rms fluctuation at mass scale  $M$ :  $\delta \propto M^{-\alpha} \quad 0 < \alpha \leq 2/3$



The observed uniformity of the CMB guarantees that density fluctuations must have been quite small at decoupling, implying that the evolution of the density contrast can be studied at  $z \lesssim z_{\text{dec}}$  using linear theory, and each mode  $\delta(k)$  evolves independently. The inflationary model predicts a scale-invariant primordial power spectrum of density fluctuations  $P(k) \equiv \langle |\delta(k)|^2 \rangle \propto k^n$ , with  $n \approx 1$  (the so-called Harrison-Zel'dovich spectrum). It is the index  $n$  that governs the balance between large and small-scale power. In the case of a Gaussian random field with zero mean, the power spectrum contains the complete statistical information about the density inhomogeneity. It is often more convenient to use the dimensionless quantity  $\Delta_k^2 \equiv [k^3 P(k)/2\pi^2]$ , which is the power per logarithmic interval in wavenumber  $k$ . In the matter-dominated epoch, this quantity retains its initial primordial shape ( $\Delta_k^2 \propto k^{n+3}$ ) only on very large scales. Small wavelength modes enter the horizon earlier on and their growth is suppressed more severely during the radiation-dominated epoch: on small scales the amplitude of  $\Delta_k^2$  is essentially suppressed by four powers of  $k$  (from  $k^{n+3}$  to  $k^{n-1}$ ). If  $n = 1$ , then small scales will have nearly the same power except for a weak, logarithmic dependence. Departures from the initially scale-free form are described by the transfer function  $T(k)$ , defined such that  $T(0) = 1$ :

$$P(k, z) = Ak^n \left[ \frac{D(z)}{D(0)} \right]^2 T^2(k),$$

where  $A$  is the normalization.

An approximate fitting function for  $T(k)$  in a  $\Lambda$ CDM universe is (Bardeen et al. 1986)

$$T_k = \frac{\ln(1 + 2.34q)}{2.34q} [1 + 3.89q + (16.1q)^2 + (5.46q)^3 + (6.71q)^4]^{-1/4},$$

where (Sugayama 1995)

$$q \equiv \frac{k/\text{Mpc}^{-1}}{\Omega_m h^2 \exp(-\Omega_b - \Omega_b/\Omega_m)}.$$

For accurate work, for example for starting high-resolution N-body simulations, it is best to use instead of fitting functions the numerical output of highly accurate integration of the Boltzmann equations, for example from CMBFast

<http://cfa-www.harvard.edu/~mzaldarr/CMBFAST/cmbfast.html>

## **W e l c o m e to the CMBFAST Website!**

This is the most extensively used code for computing cosmic microwave background anisotropy, polarization and matter power spectra. The code has been tested over a wide range of cosmological parameters. We are continuously testing and updating the code based on suggestions from the cosmological community. Do not hesitate to contact us if you have any questions or suggestions.

U. Seljak & M. Zaldarriaga

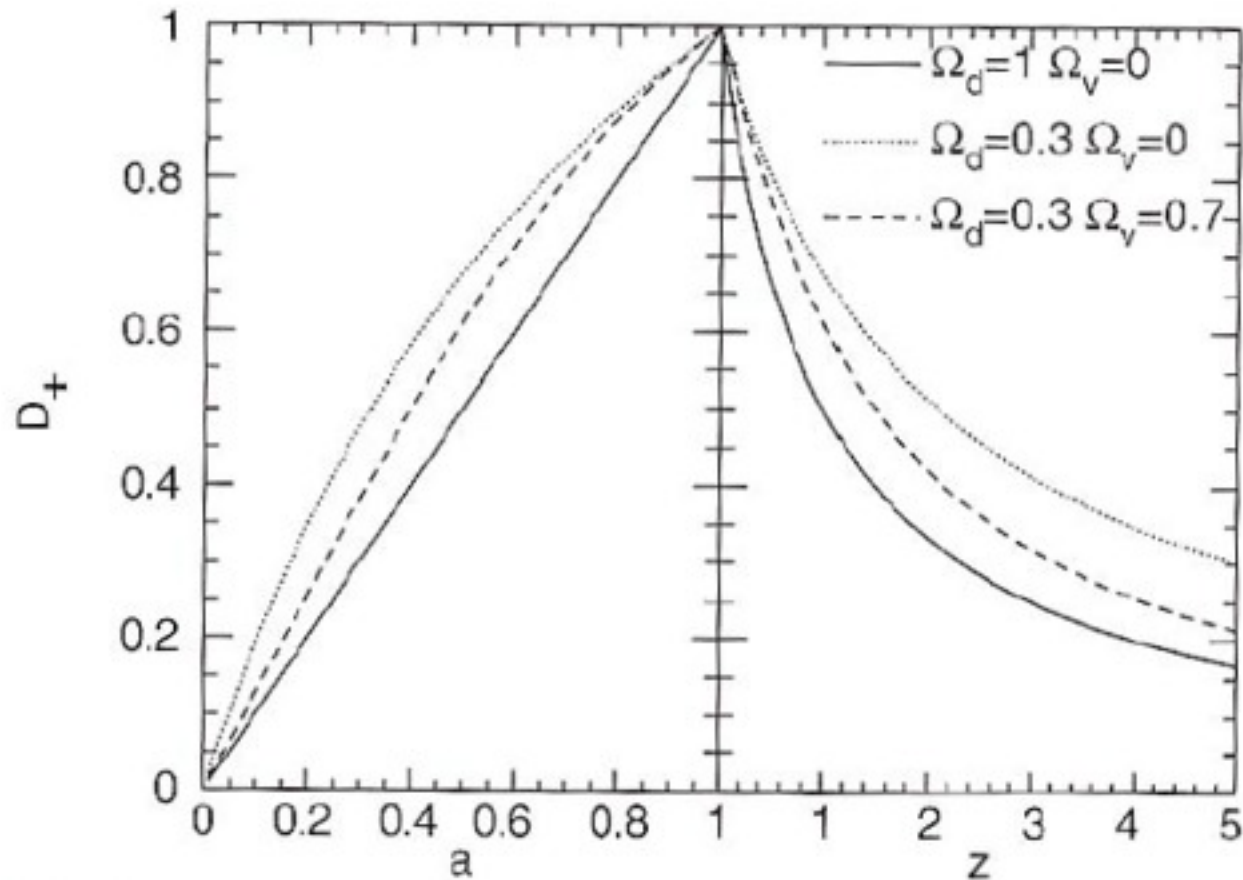


**Fig. 7.3.** Growth factor  $D_+$  for three different cosmological models, as a function of the scale factor  $a$  (left panel) and of redshift (right panel). It is clearly visible how quickly  $D_+$  decreases with increasing redshift in the EdS model, in comparison to the models of lower density

From Peter Schneider, *Extragalactic Astronomy and Cosmology* (Springer, 2006)



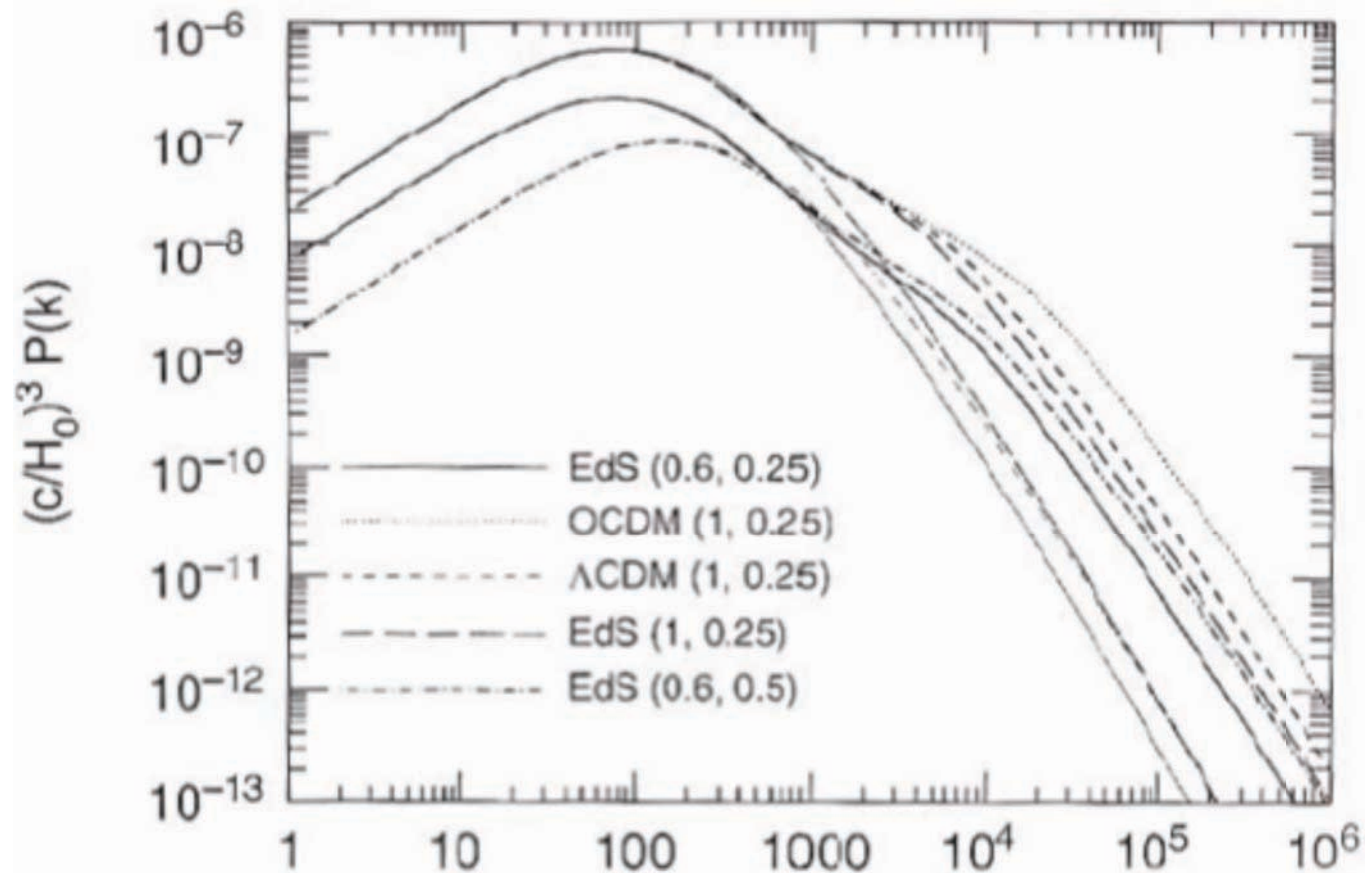


**Fig. 7.6.** The current power spectrum of density fluctuations for CDM models. The wave number  $k$  is given in units of  $H_0/c$ , and  $(H_0/c)^3 P(k)$  is dimensionless. The various curves have different cosmological parameters: EdS:  $\Omega_m = 1$ ,  $\Omega_\Lambda = 0$ ; OCDM:  $\Omega_m = 0.3$ ,  $\Omega_\Lambda = 0$ ;  $\Lambda$ CDM:  $\Omega_m = 0.3$ ,  $\Omega_\Lambda = 0.7$ . The values in parentheses specify  $(\sigma_8, \Gamma)$ , where  $\sigma_8$  is the normalization of the power spectrum (which will be discussed below), and where  $\Gamma$  is the shape parameter. The thin curves correspond to the power spectrum  $P_0(k)$  linearly extrapolated to the present day, and the bold curves take the non-linear evolution into account

From Peter Schneider,  
*Extragalactic Astronomy and  
 Cosmology* (Springer, 2006)

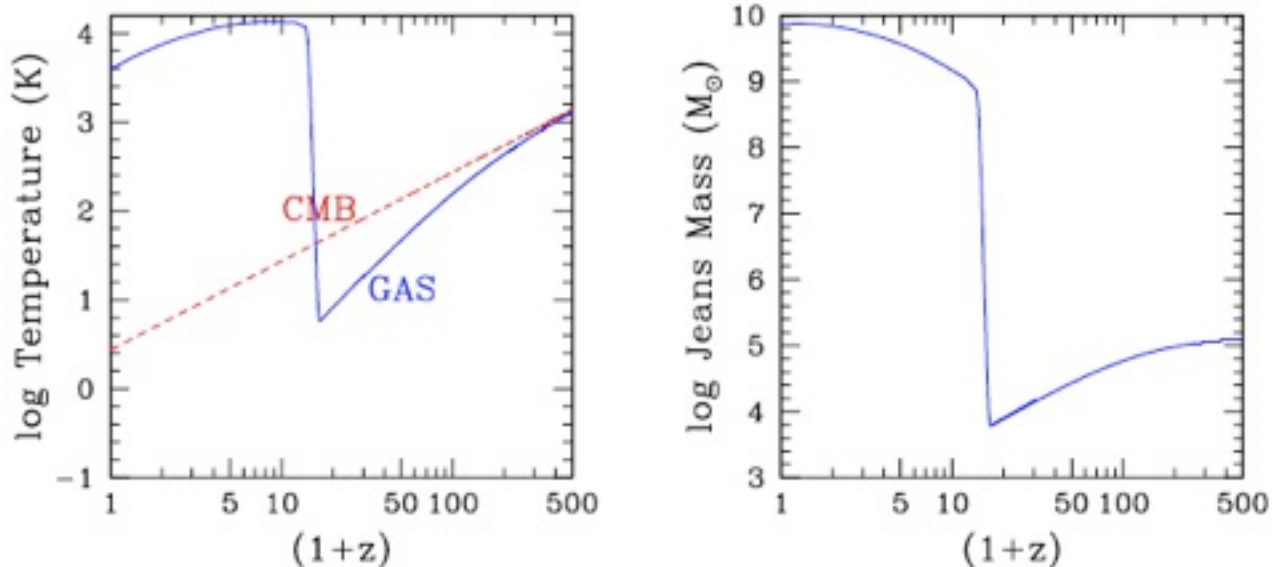
On large scales ( $k$  small), the gravity of the dark matter dominates. But on small scales, pressure dominates and growth of baryonic fluctuations is prevented. Gravity and pressure are equal at the Jeans scale

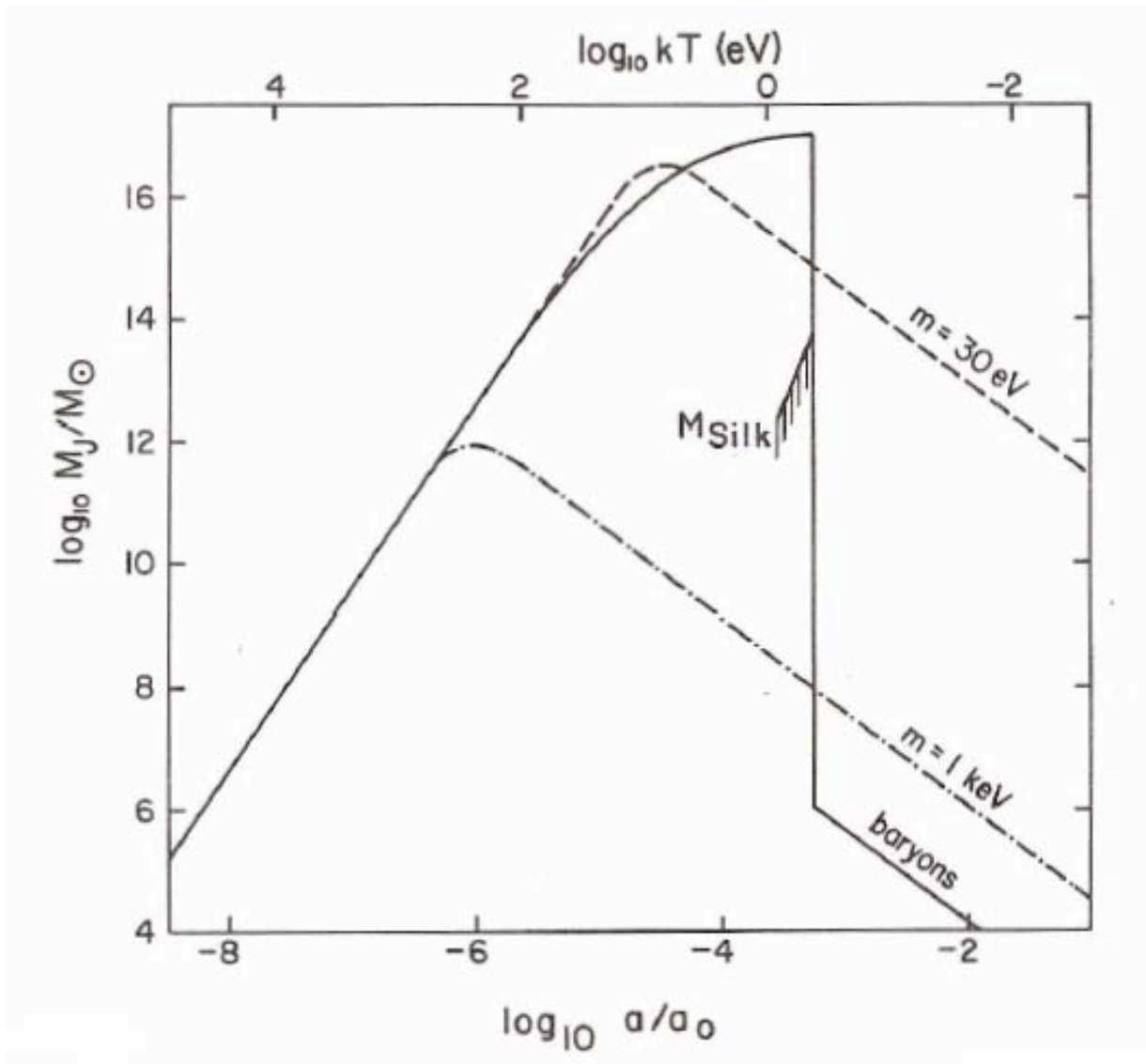
$$k_J = \frac{a}{c_s} \sqrt{4\pi G \rho}.$$

The Jeans mass is the dark matter + baryon mass enclosed within a sphere of radius  $\pi a/k_J$ ,

$$M_J = \frac{4\pi}{3} \rho \left( \frac{\pi a}{k_J} \right)^3 = \frac{4\pi}{3} \rho \left( \frac{5\pi k_B T_e}{12G\rho m_p \mu} \right)^{3/2} \approx 8.8 \times 10^4 M_\odot \left( \frac{a T_e}{\mu} \right)^{3/2},$$

where  $\mu$  is the mean molecular weight. The evolution of  $M_J$  is shown below, assuming that reionization occurs at  $z=15$ :

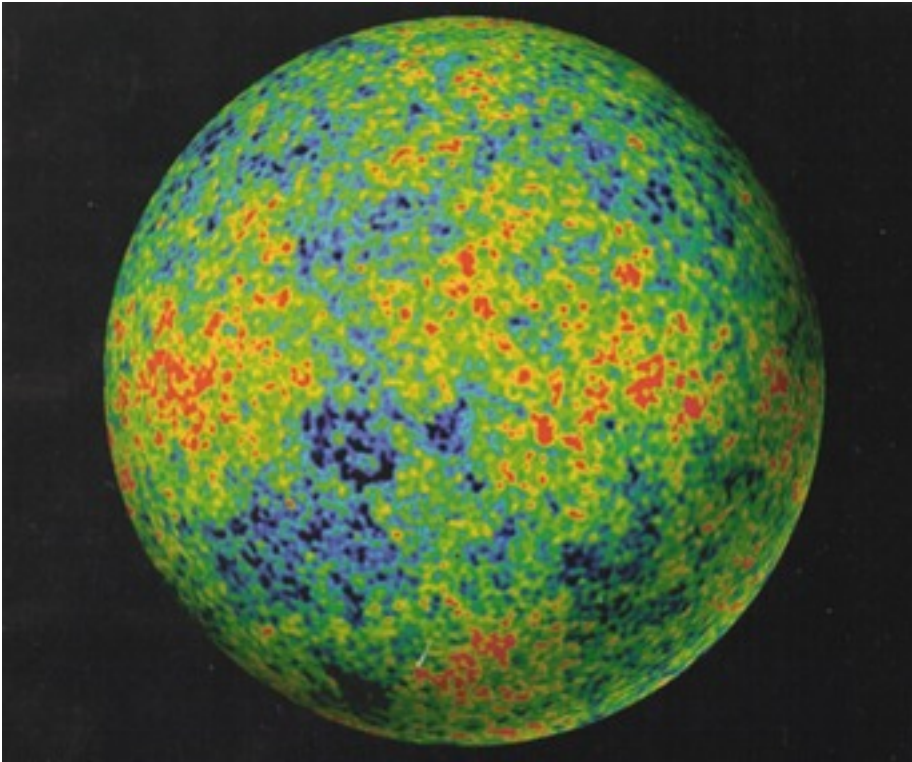




Jeans-type analysis for HDM, WDM, and CDM

# GRAVITY – The Ultimate Capitalist Principle

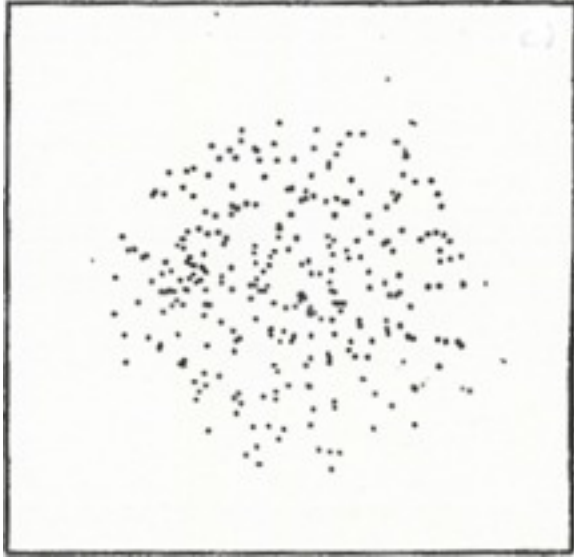
Astronomers say that a region of the universe with more matter is “richer.” Gravity magnifies differences—if one region is slightly denser than average, it will expand slightly more slowly and grow relatively denser than its surroundings, while regions with less than average density will become increasingly less dense. The rich always get richer, and the poor poorer.



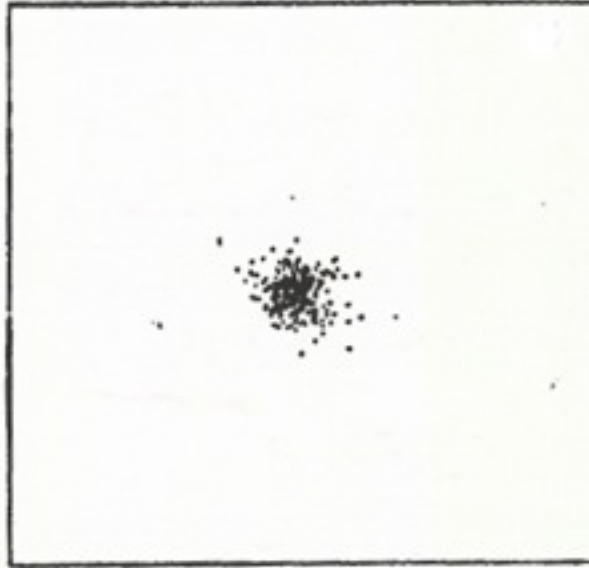
Temperature map at 380,000 years after the Big Bang. **Blue** (cooler) regions are slightly denser. From NASA's **WMAP** satellite, 2003.

The early universe expands *almost* perfectly uniformly. But there are small differences in density from place to place (about 30 parts per million). Because of gravity, denser regions expand more slowly, less dense regions more rapidly. Thus gravity amplifies the contrast between them, until...

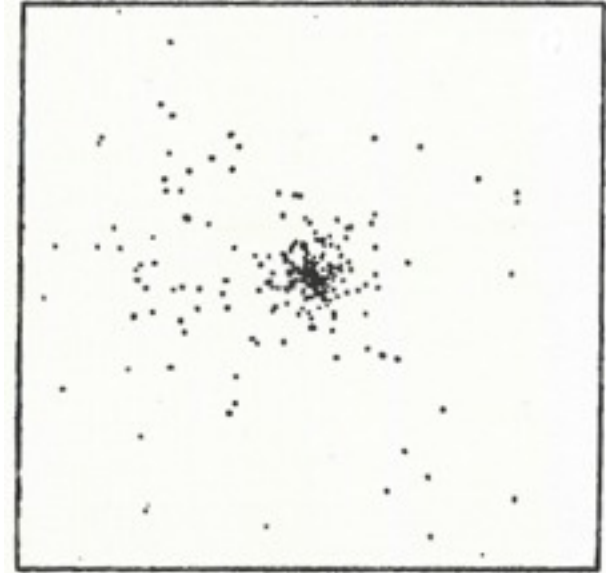
# Structure Formation by Gravitational Collapse



When any region becomes about twice as dense as typical regions its size, it reaches a maximum radius, *stops expanding,*

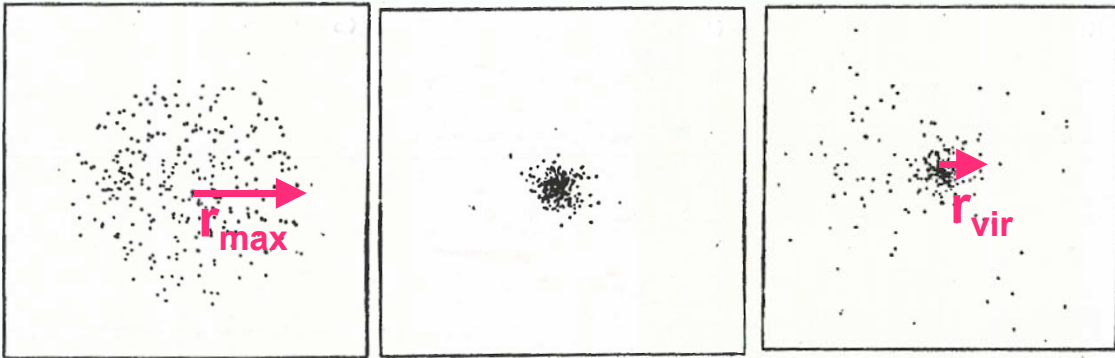


and starts falling together. The forces between the subregions generate velocities which *prevent* the material from *all falling toward the center.*



Through Violent Relaxation the dark matter quickly reaches a *stable configuration* that's about half the maximum radius but denser in the center.

Simulation of top-hat collapse:  
P.J.E. Peebles 1970, ApJ, 75, 13.



TOP HAT  
Max Expansion

VIOLENT  
RELAXATION

VIRIALIZED

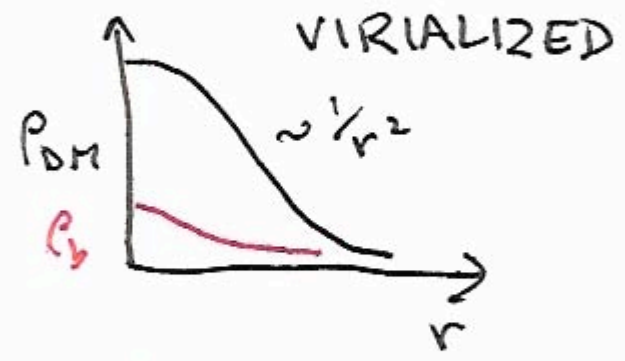
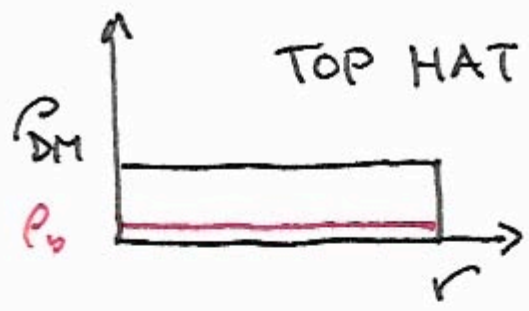
Virial Theorem:  $\langle K \rangle = -\frac{1}{2} \langle W \rangle$

$W_m = \frac{C}{r_m}$ , so after virialization

$$\frac{C}{r_m} = E = W + K = \frac{1}{2} \langle W \rangle = \frac{C}{2r_v}$$

$$\Rightarrow r_v = \frac{1}{2} r_m, \quad \rho_v = 8\rho_m \approx 50 \bar{\rho}(t_m)$$

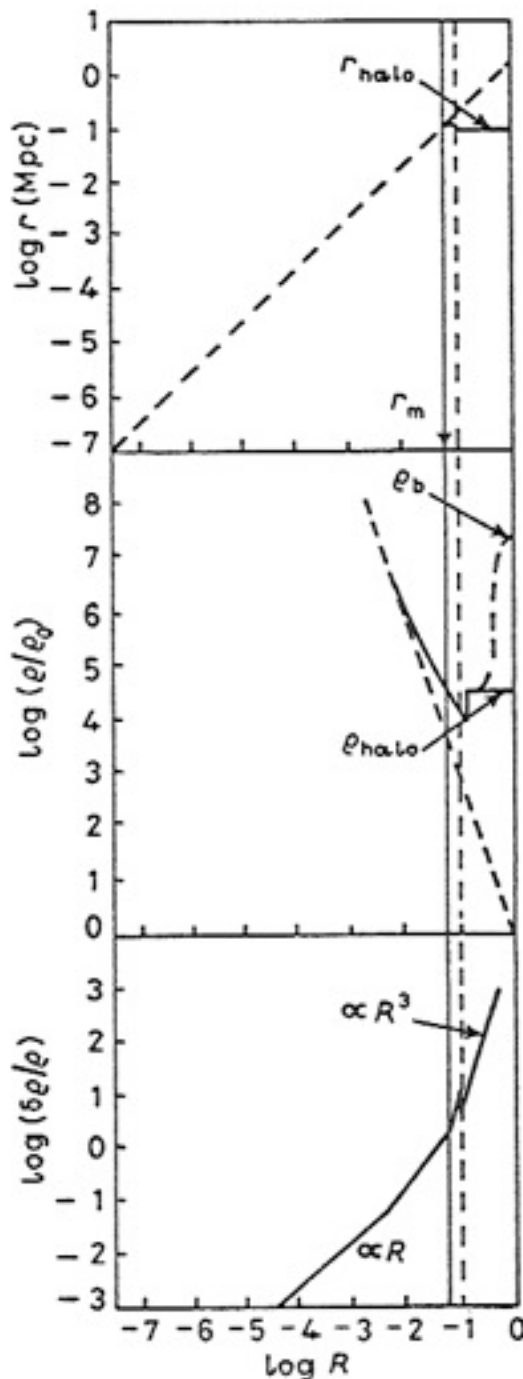
$$\langle v^2 \rangle \approx \frac{GM}{r_v}$$



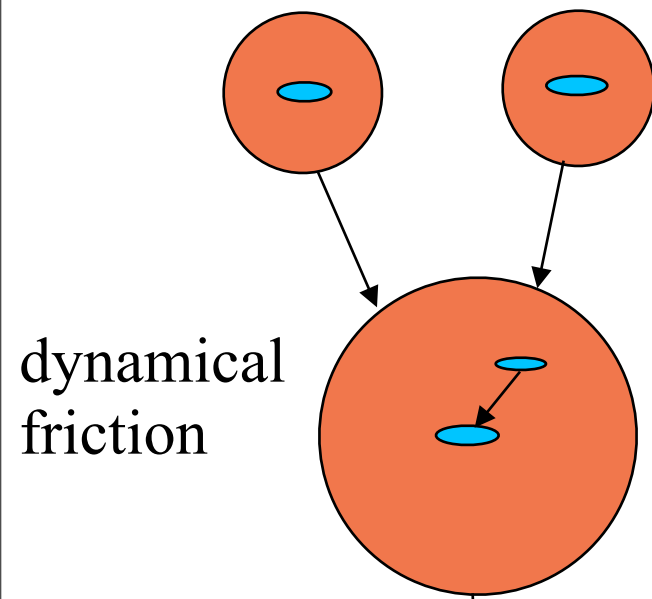
# Growth and Collapse of Fluctuations

Schematic sketches of radius, density, and density contrast of an overdense fluctuation. It initially expands with the Hubble expansion, reaches a maximum radius (solid vertical line), and undergoes violent relaxation during collapse (dashed vertical line), which results in the dissipationless matter forming a stable halo. Meanwhile the ordinary matter  $\rho_b$  continues to dissipate kinetic energy and contract, thereby becoming more tightly bound, until dissipation is halted by star or disk formation, explaining the origin of galactic spheroids and disks.

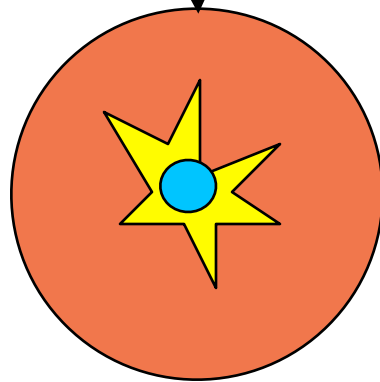
(This was the simplified discussion of [BFPR84](#); the figure is from my 1984 lectures at the Varenna school. Now we take into account halo growth by accretion, and the usual assumption is that spheroids form mostly as a result of galaxy mergers [Toomre 1977](#).)



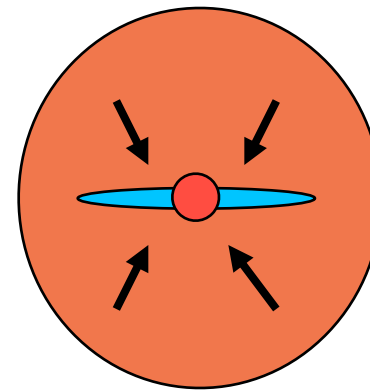
# Halo and Galaxy Merging and Spheroid Formation



dynamical friction



mergers can trigger starburst, forming spheroid



subsequent cooling forms disk



# Filamentary Structure: Zel'dovich Approximation

displacement from initial position:  $x(q, t) = q - D(t) \nabla \phi(q)$

continuity:

$$\rho(x, t) d^3x = \rho_q d^3q \rightarrow$$

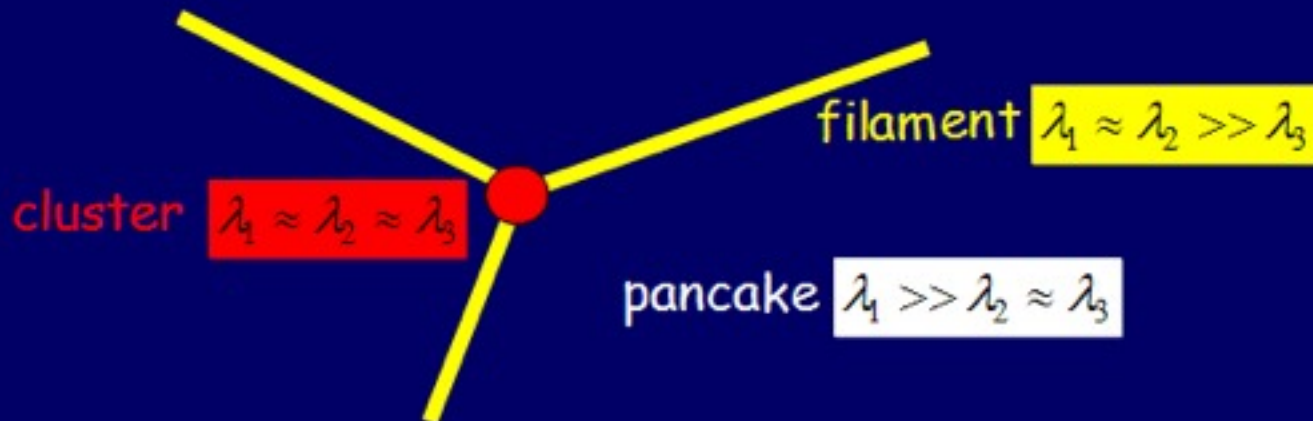
$$\rightarrow \rho(x, t) = \rho_q / \|\partial \vec{x} / \partial \vec{q}\|$$

$$= \frac{\rho_q}{(1 - D(t)\lambda_1)(1 - D(t)\lambda_2)(1 - D(t)\lambda_3)}$$

Growth Factor

eigenvalues of deformation tensor:

$$\lambda_i \equiv \frac{\partial^2 \phi}{\partial^2 q_i}, \quad \lambda_1 \geq \lambda_2 \geq \lambda_3$$



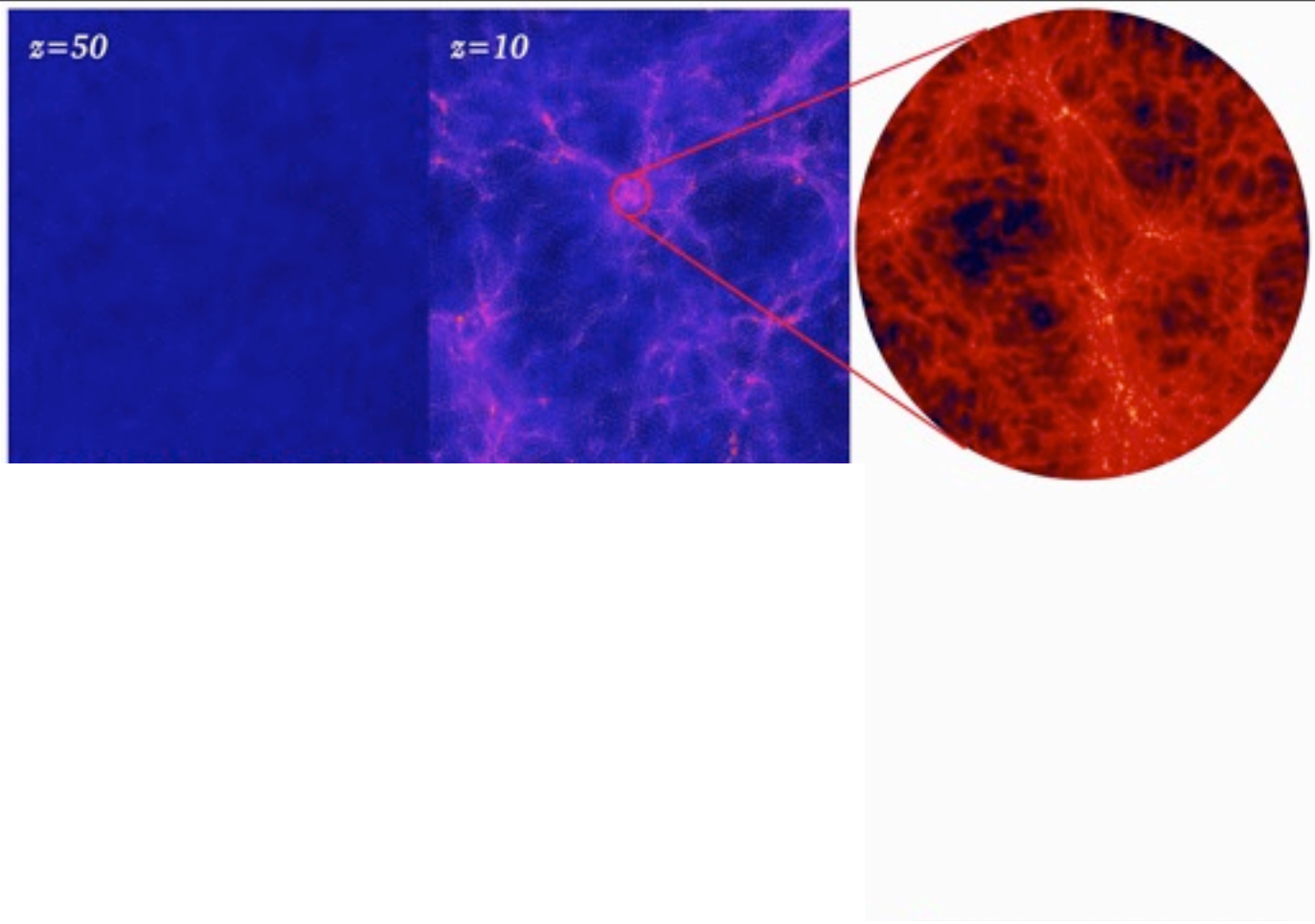
$z=50$

N-body simulation

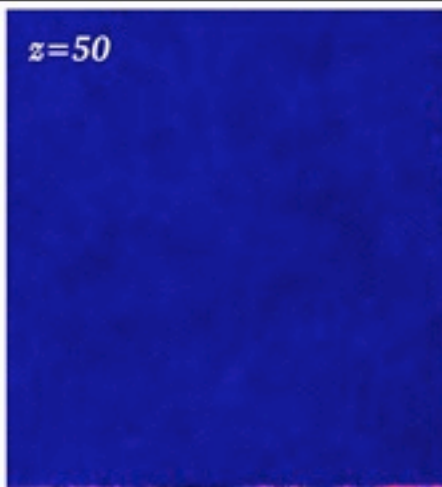
$\Lambda$ CDM

$z=50$

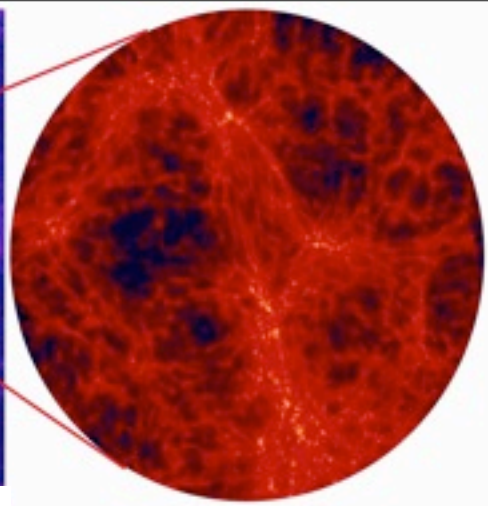
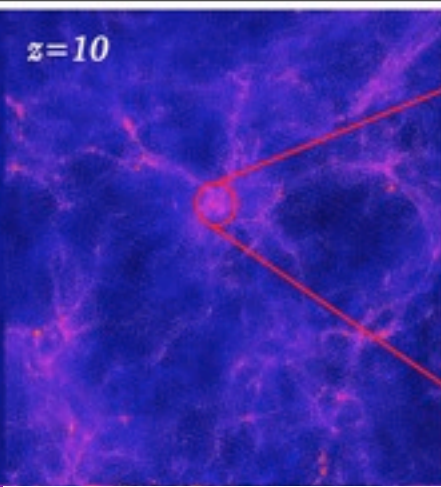
$z=10$



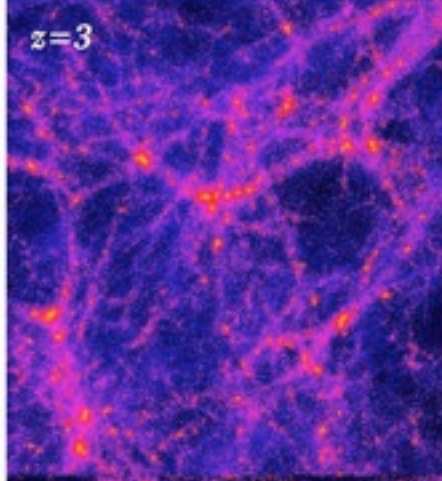
$z=50$



$z=10$

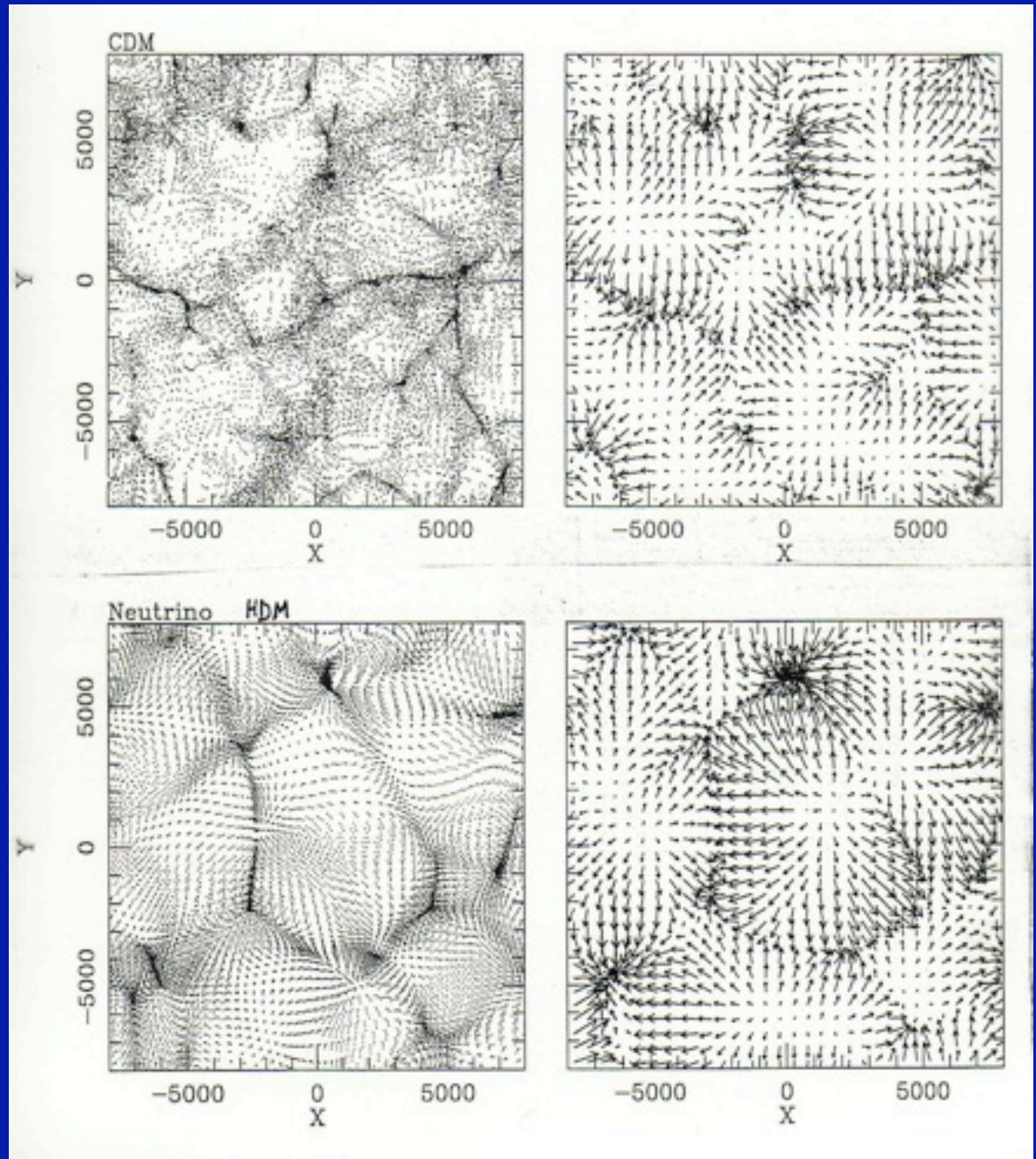


$z=3$



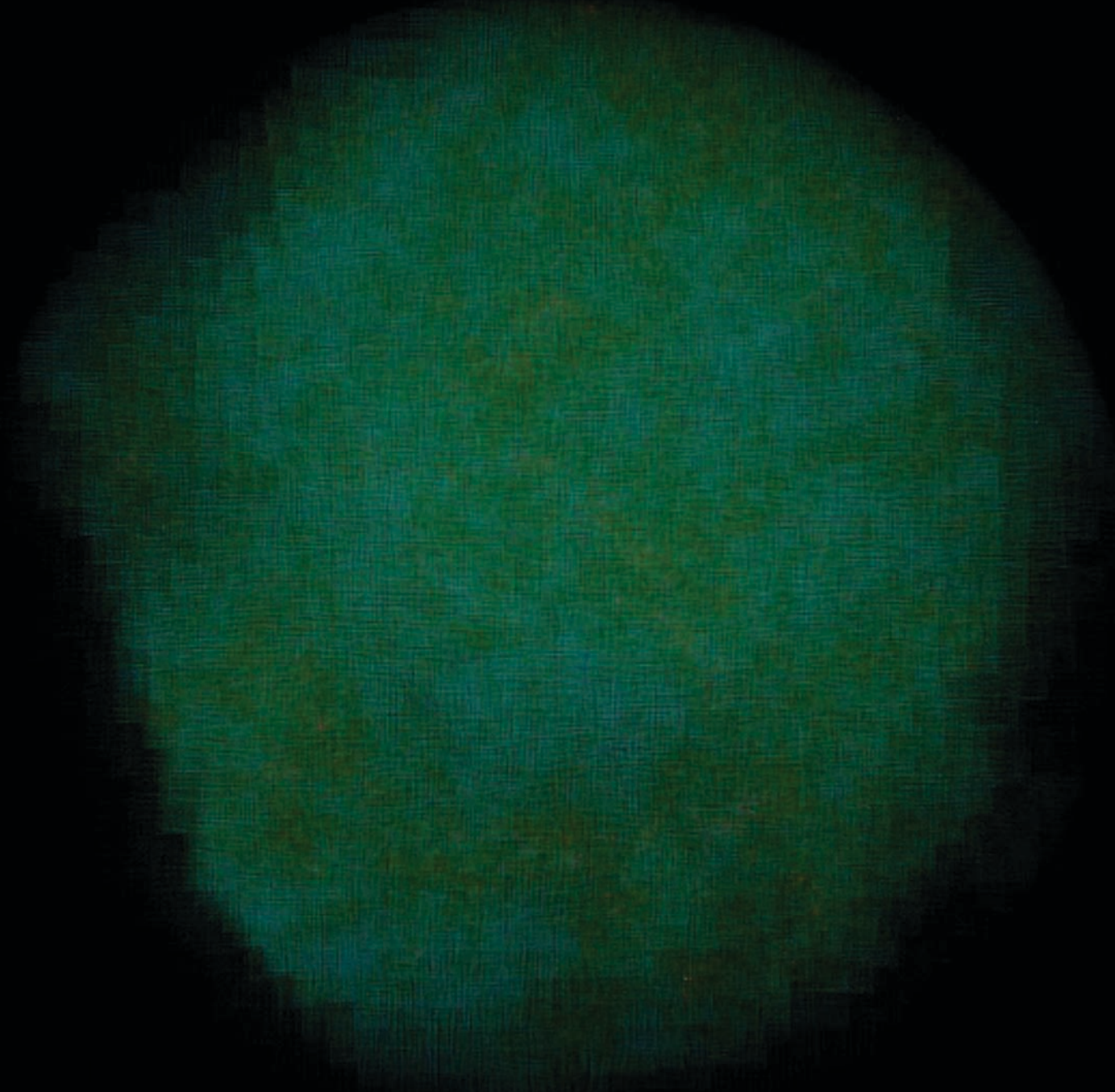
# Micro-Macro Connection

Cold Dark Matter



Hot Dark Matter

$\nu$

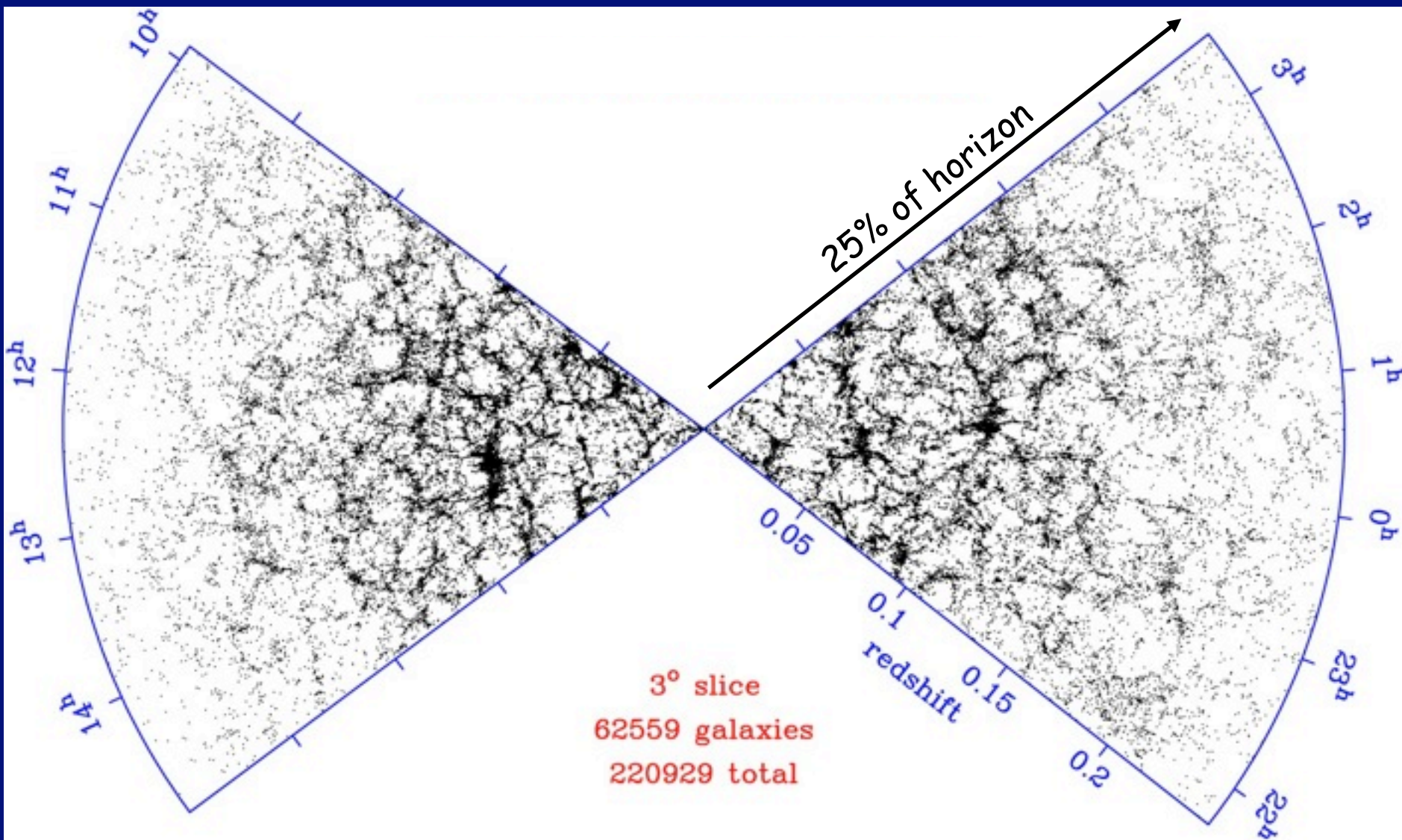


Columbia  
Super  
computer  
NASA  
Ames

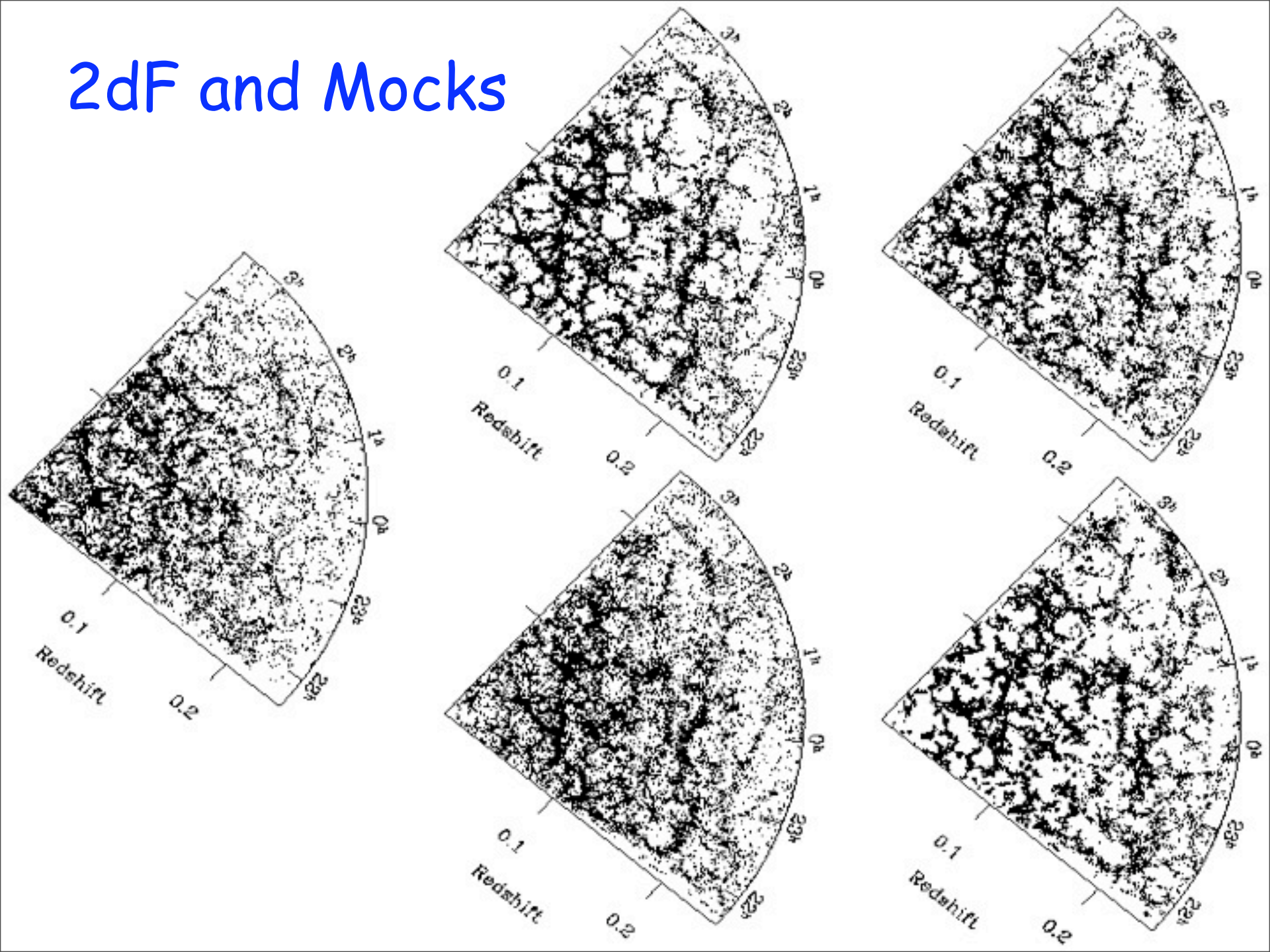
Simulation:  
Brandon  
Allgood  
& Joel  
Primack

Visualization:  
Chris  
Henze

# 2dF redshift survey



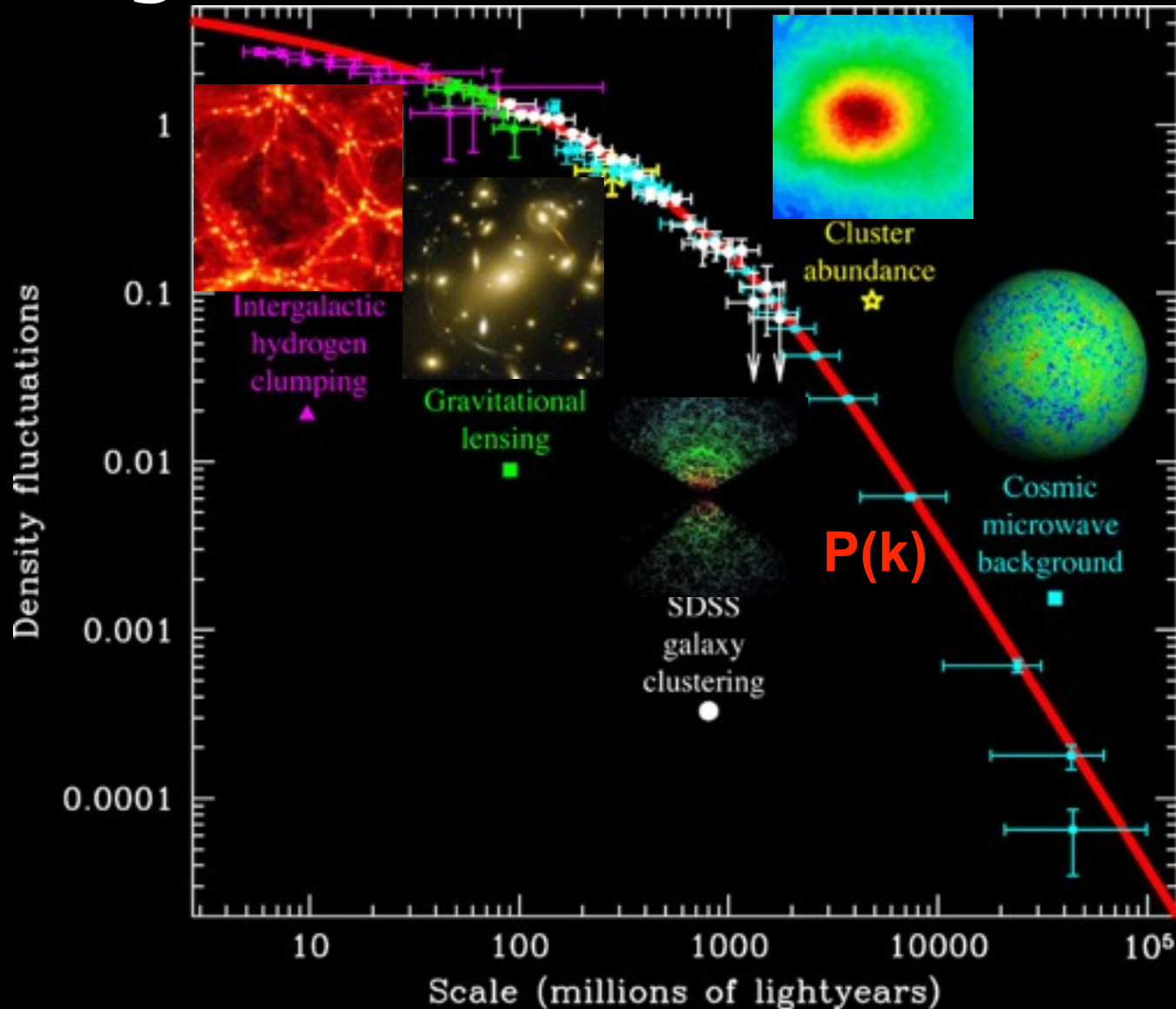
# 2dF and Mocks





# $\Lambda$ CDM Fluctuation Spectrum

Agrees with Observations!



We define the characteristic properties of a dark halo within a sphere of radius  $r_{200}$  chosen so that the mean enclosed density is 200 times the mean cosmic value. Then

$$r_{200} = \left[ \frac{GM}{100\Omega_m(z)H^2(z)} \right]^{1/3}, \quad \text{and} \quad V_c = \left( \frac{GM}{r_{200}} \right)^{1/2}, \quad R(M) \equiv \left( \frac{3M}{4\pi\bar{\rho}_0} \right)^{1/3}, \quad \sigma^2(R) = \frac{1}{2\pi^2} \int_0^\infty k^3 P(k) \bar{W}^2(kR) \frac{dk}{k},$$

According to the argument first given by Press & Schechter (1974, hereafter PS), the abundance of haloes as a function of mass and redshift, expressed as the number of haloes per unit comoving volume at redshift  $z$  with mass in the interval  $(M, M + dM)$ , may be written as

$$n(M, z) dM = \sqrt{\frac{2}{\pi}} \frac{\bar{\rho}_0}{M} \frac{d\nu}{dM} \exp\left(-\frac{\nu^2}{2}\right) dM. \quad (9)$$

Here  $\nu \equiv \delta_c/[D(z)\sigma(M)]$ , where  $\delta_c \approx 1.69$  and the growth factor is  $D(z) = g(z)/[g(0)(1+z)]$  with

$$g(z) \approx \frac{5}{2} \Omega_m \left[ \Omega_m^{4/7} - \Omega_\Lambda + (1 + \Omega_m/2)(1 + \Omega_\Lambda/70) \right]^{-1}, \quad \Omega_m \equiv \Omega_m(z), \quad \Omega_\Lambda \equiv \Omega_\Lambda(z) = \frac{\Omega_{\Lambda,0}}{E^2(z)}.$$

$$E(z) = \left[ \Omega_{\Lambda,0} + (1 - \Omega_0)(1+z)^2 + \Omega_{m,0}(1+z)^3 \right]^{1/2}. \quad \text{Lahav, Lilje, Primack, & Rees 1991}$$

Press & Schechter derived the above mass function from the *Ansatz* that the fraction  $F$  of all cosmic mass which at redshift  $z$  is in haloes with masses exceeding  $M$  is *twice* the fraction of randomly placed spheres of radius  $R(M)$  which have linear overdensity at that time exceeding  $\delta_c$ , the value at which a spherical perturbation collapses. Since the linear fluctuation distribution is gaussian this hypothesis implies

$$F(> M, z) = \text{erfc}\left(\frac{\nu}{\sqrt{2}}\right), \quad (12)$$

and equation (9) then follows by differentiation.

The PS formula is 
$$n(M, z)dM = \sqrt{\frac{2}{\pi}} \frac{\bar{\rho}_0}{M} \frac{d\nu}{dM} \exp\left(-\frac{\nu^2}{2}\right) dM \quad (9)$$

Numerical simulations show that although the scaling properties implied by the PS argument hold remarkably well for a wide variety of hierarchical cosmogonies, substantially better fits to simulated mass functions are obtained if the error function in equation (12) is replaced by a function of slightly different shape. Sheth & Tormen (1999) suggested the following modification of equation (9)

$$n(M, z)dM = A \left(1 + \frac{1}{\nu'^{2q}}\right) \sqrt{\frac{2}{\pi}} \frac{\bar{\rho}}{M} \frac{d\nu'}{dM} \exp\left(-\frac{\nu'^2}{2}\right) dM, \quad (14)$$

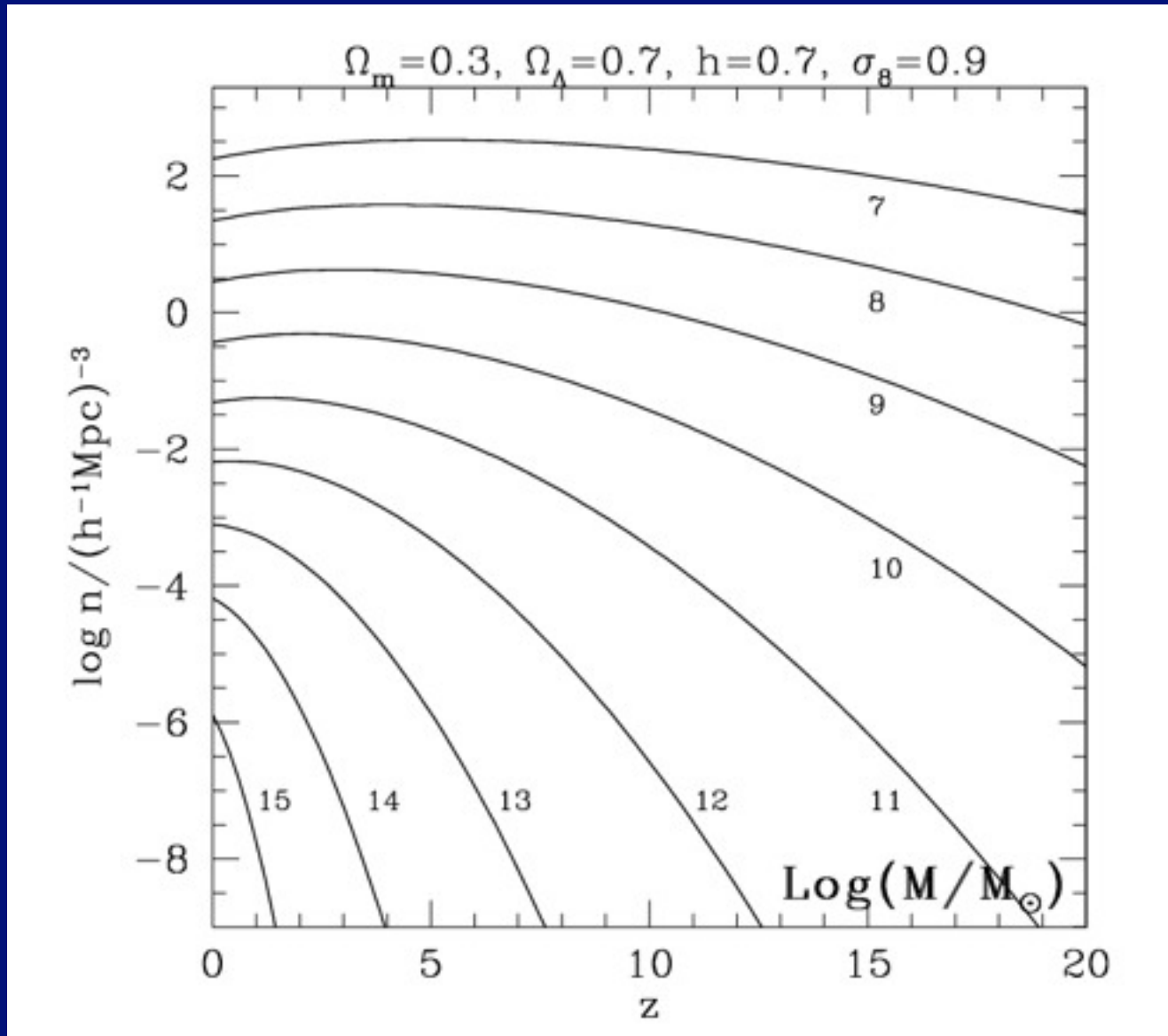
where  $\nu' = \sqrt{a}\nu$ ,  $a = 0.707$ ,  $A \approx 0.322$  and  $q = 0.3$ .

[See Sheth, Mo & Tormen (2001) and Sheth & Tormen (2002) for a justification of this formula in terms of an ellipsoidal model for perturbation collapse.] The fraction of all matter in haloes with mass exceeding  $M$  can be obtained by integrating equation (14). To good approximation,

$$F(> M, z) \approx 0.4 \left(1 + \frac{0.4}{\nu^{0.4}}\right) \operatorname{erfc}\left(\frac{0.85\nu}{\sqrt{2}}\right)$$

In a detailed comparison with a wide range of simulations, Jenkins et al. (2001) confirmed that this model is indeed a good fit provided haloes are defined at the same density contrast relative to the mean in all cosmologies.

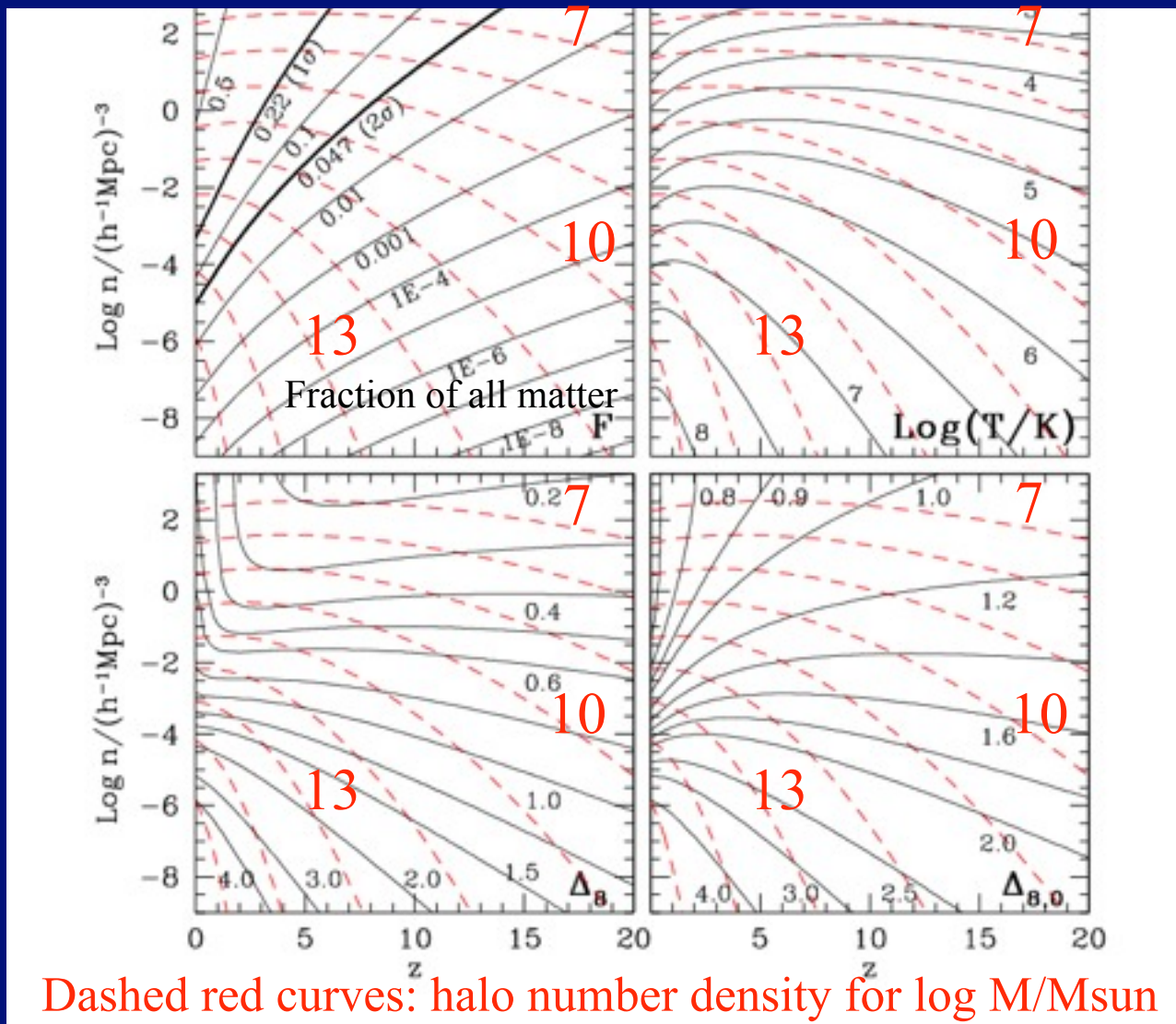
# Improved Press-Schechter Halo Number Density



Mo &  
White  
2002

# Comoving Halo Number Density vs. Mass

$M^*$



Standard  
LCDM

Mo &  
White  
2002

Dashed red curves: halo number density for  $\log M/M_{\text{sun}}$

# Cosmological Simulation Methods

## Dissipationless Simulations

Particle-Particle (PP) - Aarseth NbodyN,  $N=1, \dots, 6$

Particle Mesh (PM) - see Klypin & Holtzman 1997

Adaptive PM (P3M) - Efstathiou et al.

Tree - Barnes & Hut 1986, PKDGRAV Stadel

TreePM - GADGET2, Springel 2005

Adaptive Mesh Refinement (AMR) - Klypin (ART)

## Hydrodynamical Simulations

Fixed grid - Cen & Ostriker

Smooth Particle Hydrodynamics (SPH) - GADGET2, Springel 2005

- Gasoline, Wadsley, Stadel, & Quinn

Adaptive grid - ART+hydro - Klypin & Kravtsov

## Initial Conditions

Standard: Gaussian  $P(k)$  realized uniformly, Zel'dovich displacement

Multimass - put lower mass particles in a small part of sim volume

Constrained realization - small scale: simulate individual halos (NFW)

large scale: simulate particular region

## Reviews

Bertschinger ARAA 1998, Klypin lectures 2002, U Washington website

# Structure of Dark Matter Halos

Navarro, Frenk, White

1996

1997 →

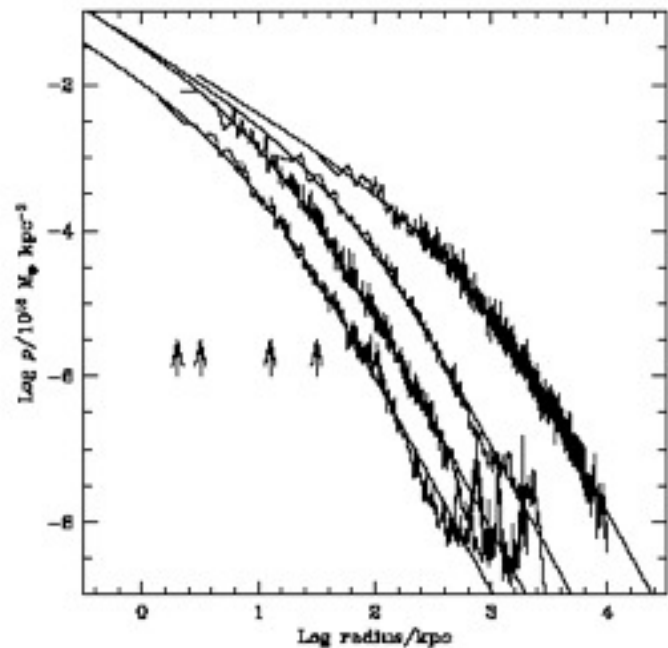
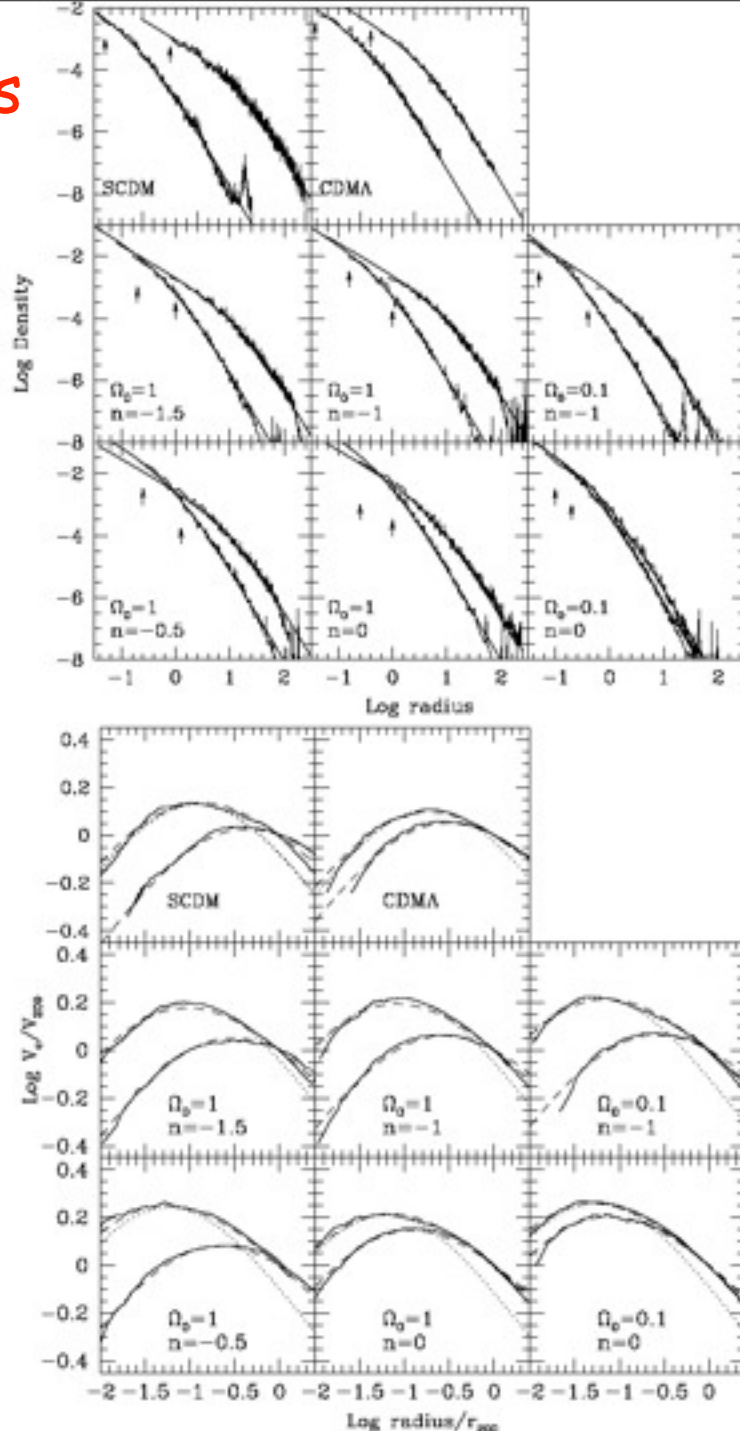


Fig. 3.— Density profiles of four halos spanning four orders of magnitude in mass. The arrows indicate the gravitational softening,  $h_g$ , of each simulation. Also shown are fits from eq.3. The fits are good over two decades in radius, approximately from  $h_g$  out to the virial radius of each system.

$$\frac{\rho(r)}{\rho_{crit}} = \frac{\delta_c}{(r/r_s)(1+r/r_s)^2}, \quad (3)$$

NFW formula works for all models



# Dark Matter Halo Radial Profile

COMPARISON OF NFW AND MOORE ET AL. PROFILES

Parameter	NFW	Moore et al.
Density $x = r/r_s$	$\rho = \frac{\rho_s}{x(1+x)^2}$ $\rho \propto x^{-3} \text{ for } x \gg 1$ $\rho \propto x^{-1} \text{ for } x \ll 1$ $\rho/\rho_s = 1/4 \quad \text{at } x = 1$	$\rho = \frac{\rho_s}{x^{1.5}(1+x)^{1.5}}$ $\rho \propto x^{-3} \text{ for } x \gg 1$ $\rho \propto x^{-1.5} \text{ for } x \ll 1$ $\rho/\rho_s = 1/2 \quad \text{at } x = 1$
Mass $M = 4\pi\rho_s r_s^3 f(x)$ $= M_{\text{vir}} f(x)/f(C)$ $M_{\text{vir}} = \frac{4\pi}{3} \rho_{\text{cr}} \Omega_0 \delta_{\text{top-hat}} r_{\text{vir}}^3$	$f(x) = \ln(1+x) - \frac{x}{1+x}$	$f(x) = \frac{2}{3} \ln(1+x^{3/2})$
Concentration $C = r_{\text{vir}}/r_s$	$C_{\text{NFW}} = 1.72 C_{\text{Moore}}$ for halos with the same $M_{\text{vir}}$ and $r_{\text{max}}$ $C_{1/5} \approx \frac{C_{\text{NFW}}}{0.86 f(C_{\text{NFW}}) + 0.1363}$ error less than 3% for $C_{\text{NFW}} = 5-30$ $C_{\gamma=-2} = C_{\text{NFW}}$	$C_{\text{Moore}} = C_{\text{NFW}}/1.72$ $C_{1/5} = \frac{C_{\text{Moore}}}{[(1+C_{\text{Moore}}^{3/2})^{1/5} - 1]^{2/3}}$ $\approx \frac{C_{\text{Moore}}}{[C_{\text{Moore}}^{3/10} - 1]^{2/3}}$ $C_{\gamma=-2} = 2^{3/2} C_{\text{Moore}}$ $\approx 2.83 C_{\text{Moore}}$
Circular Velocity $v_{\text{circ}}^2 = \frac{GM_{\text{vir}}}{r_{\text{vir}}} \frac{C}{x} \frac{f(x)}{f(C)}$ $= v_{\text{max}}^2 \frac{x_{\text{max}}}{x} \frac{f(x)}{f(x_{\text{max}})}$ $v_{\text{vir}}^2 = \frac{GM_{\text{vir}}}{r_{\text{vir}}}$	$x_{\text{max}} \approx 2.15$ $v_{\text{max}}^2 \approx 0.216 v_{\text{vir}}^2 \frac{C}{f(C)}$ $\rho/\rho_s \approx 1/21.3 \text{ at } x = 2.15$	$x_{\text{max}} \approx 1.25$ $v_{\text{max}}^2 \approx 0.466 v_{\text{vir}}^2 \frac{C}{f(C)}$ $\rho/\rho_s \approx 1/3.35 \text{ at } x = 1.25$

Klypin, Kravtsov, Bullock & Primack 2001



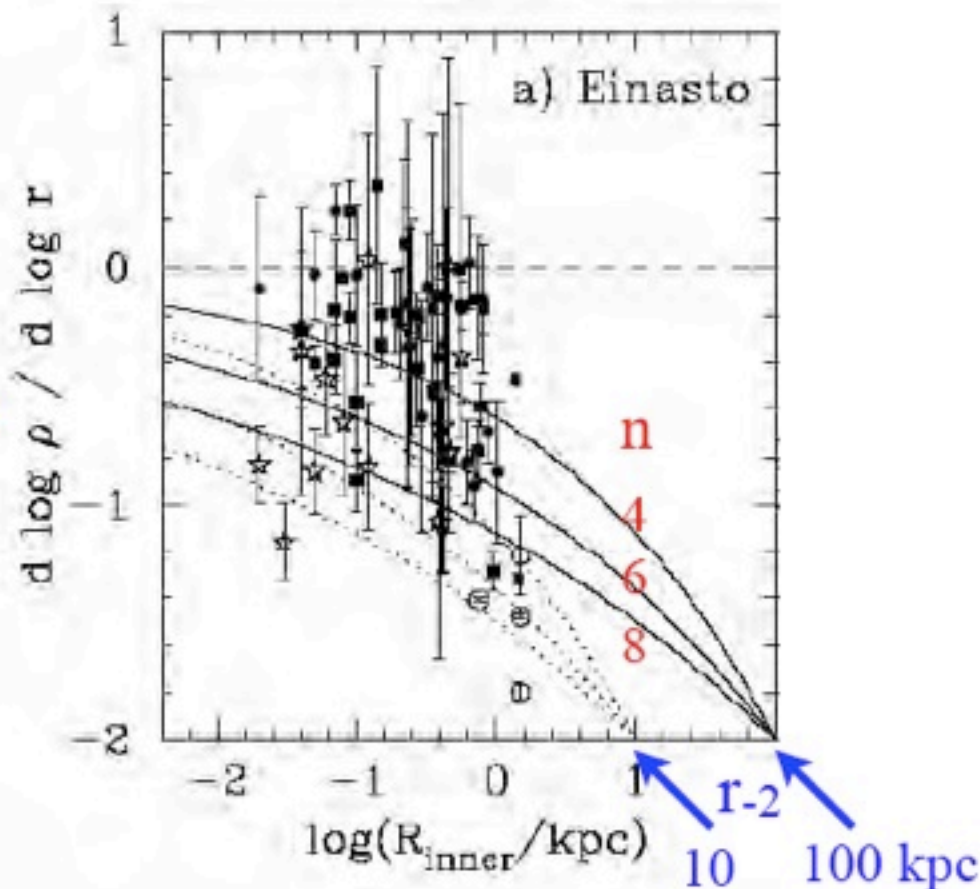
# Empirical Models for Dark Matter Halos. II. Inner profile slopes, dynamical profiles, and $\rho/\sigma^3$

Alister Graham, David Merritt, Ben Moore, Jürg Diemand, Balša Terzić

Einasto's model is given by the equation

$$\rho(r) = \rho_e \exp \left\{ -d_n \left[ (r/r_e)^{1/n} - 1 \right] \right\}.$$

Data on log slopes from innermost resolved radius of observed galaxies, not corrected for observational effects -- adapted from de Blok (2004).



# Evolution of Halo Maximum Circular Velocity

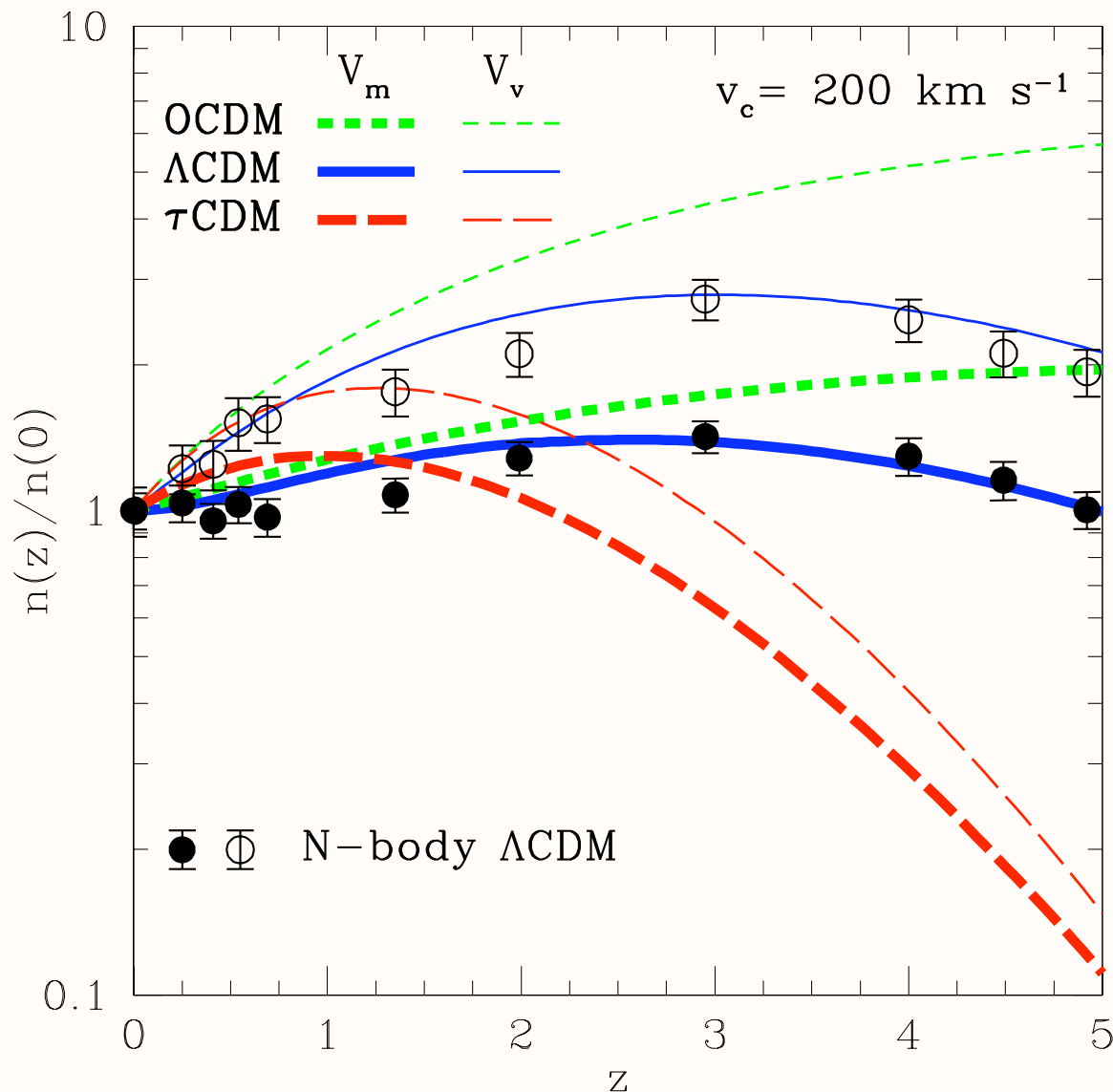


FIG. 1.— Evolution of relative comoving number density for fixed  $v_m = 200 \text{ km s}^{-1}$  (bold curves) and  $v_v = 200 \text{ km s}^{-1}$  halos in three cosmologies.

Bullock, Dekel, Kolatt,  
Primack, & Somerville  
2001, ApJ, 550, 21

# Dependence of Halo Concentration on Mass and Redshift

## Profiles of dark haloes: evolution, scatter, and environment

J. S. Bullock<sup>1,2</sup>, T. S. Kolatt<sup>1,3</sup>, Y. Sigad<sup>3</sup>, R.S. Somerville<sup>3,4</sup>, A. V. Kravtsov<sup>2,5\*</sup>,  
A. A. Klypin<sup>5</sup>, J. R. Primack<sup>1</sup>, and A. Dekel<sup>3</sup> 2001 MNRAS 321, 559

### ABSTRACT

We study dark-matter halo density profiles in a high-resolution N-body simulation of a  $\Lambda$ CDM cosmology. Our statistical sample contains  $\sim 5000$  haloes in the range  $10^{11} - 10^{14} h^{-1} M_{\odot}$  and the resolution allows a study of subhaloes inside host haloes. The profiles are parameterized by an NFW form with two parameters, an inner radius  $r_s$  and a virial radius  $R_{\text{vir}}$ , and we define the halo concentration  $c_{\text{vir}} \equiv R_{\text{vir}}/r_s$ . We find that, for a given halo mass, the redshift dependence of the median concentration is  $c_{\text{vir}} \propto (1+z)^{-1}$ . This corresponds to  $r_s(z) \sim \text{constant}$ , and is contrary to earlier suspicions that  $c_{\text{vir}}$  does not vary much with redshift. The implications are that high-redshift galaxies are predicted to be more extended and dimmer than expected before. Second, we find that the scatter in halo profiles is large, with a  $1\sigma$   $\Delta(\log c_{\text{vir}}) = 0.18$  at a given mass, corresponding to a scatter in maximum rotation velocities of  $\Delta V_{\text{max}}/V_{\text{max}} = 0.12$ . We discuss implications for modelling the Tully-Fisher relation, which has a smaller reported intrinsic scatter. Third, subhaloes and haloes in dense environments tend to be more concentrated than isolated haloes, and show a larger scatter. These results suggest that  $c_{\text{vir}}$  is an essential parameter for the theory of galaxy modelling, and we briefly discuss implications for the universality of the Tully-Fisher relation, the formation of low surface brightness galaxies, and the origin of the Hubble sequence. We present an improved analytic treatment of halo formation that fits the measured relations between halo parameters and their redshift dependence, and can thus serve semi-analytic studies of galaxy formation.

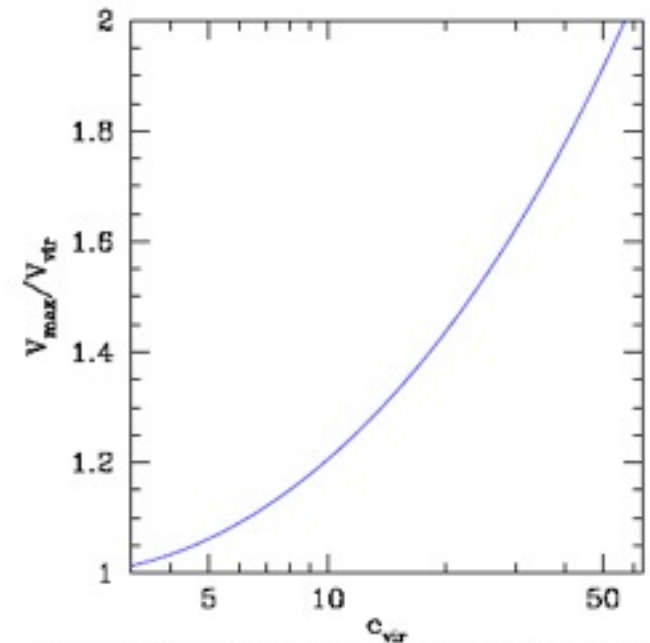


Figure 1. Maximum velocity versus concentration. The maximum rotation velocity for an NFW halo in units of the rotation velocity at its virial radius as a function of halo concentration.

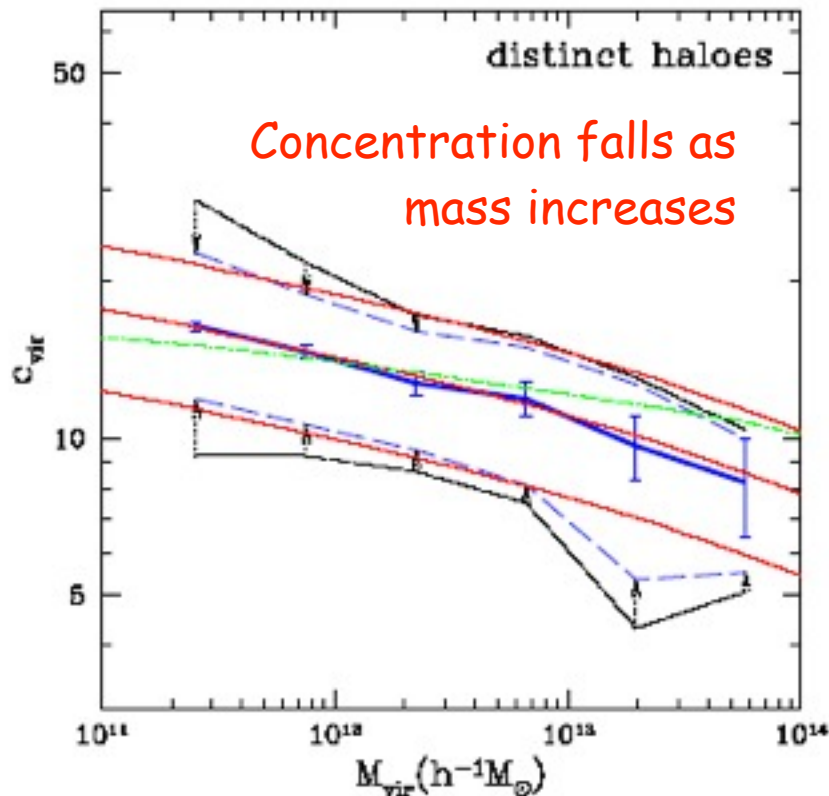


Figure 4. Concentration versus mass for distinct haloes at  $z = 0$ . The thick solid curve is the median at a given  $M_{\text{vir}}$ . The error bars represent Poisson errors of the mean due to the sampling of a finite number of haloes per mass bin. The outer dot-dashed curves encompass 68% of the  $c_{\text{vir}}$  values as measured in the simulations. The inner dashed curves represent only the true, intrinsic scatter in  $c_{\text{vir}}$ , after eliminating both the Poisson scatter and the scatter due to errors in the individual profile fits due, for example, to the finite number of particles per halo. The central and outer thin solid curves are the predictions for the median and 68% values by the toy model outlined in the text, for  $F = 0.01$  and three different values of  $K$ . The thin dot-dashed line shows the prediction of the toy model of NFW97 for  $f = 0.01$  and  $k = 3.4 \times 10^3$ .

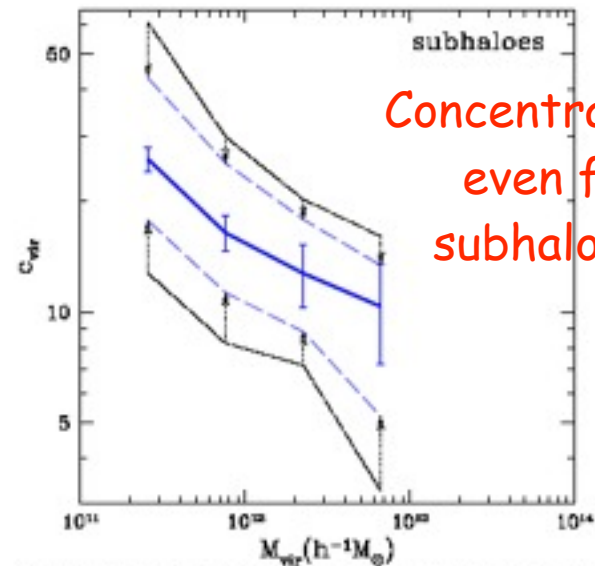


Figure 5. Concentration versus mass for subhaloes at  $z = 0$ . The curves and errors are the same as in Figure 4.

Concentration rises as density increases

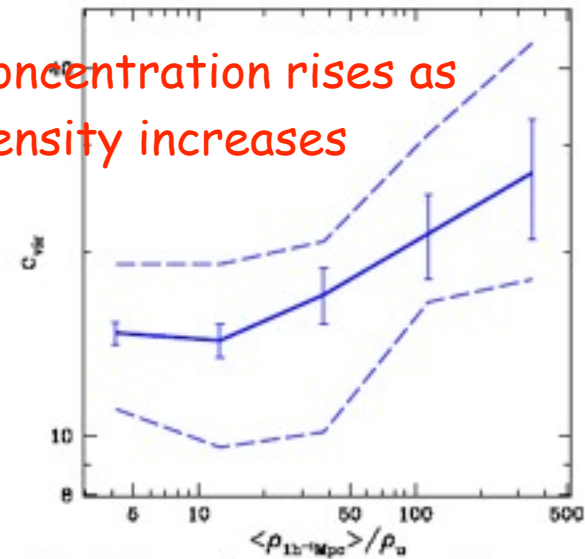
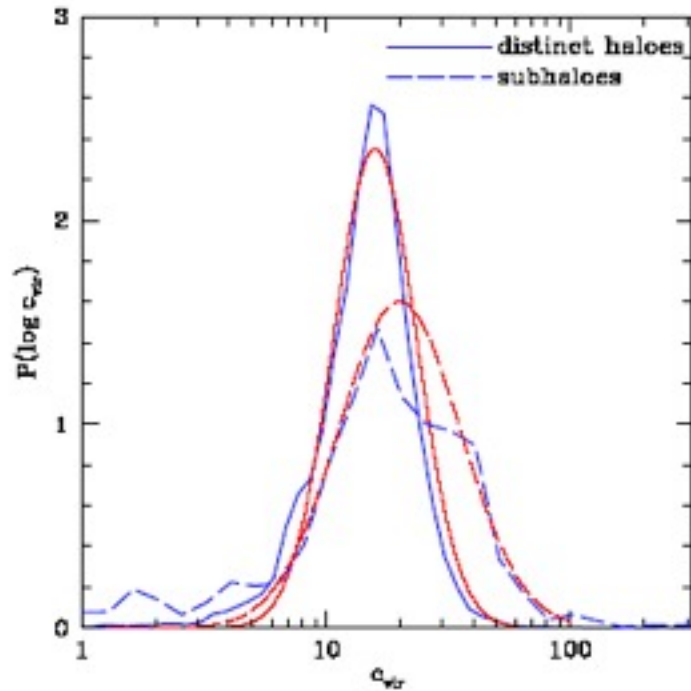
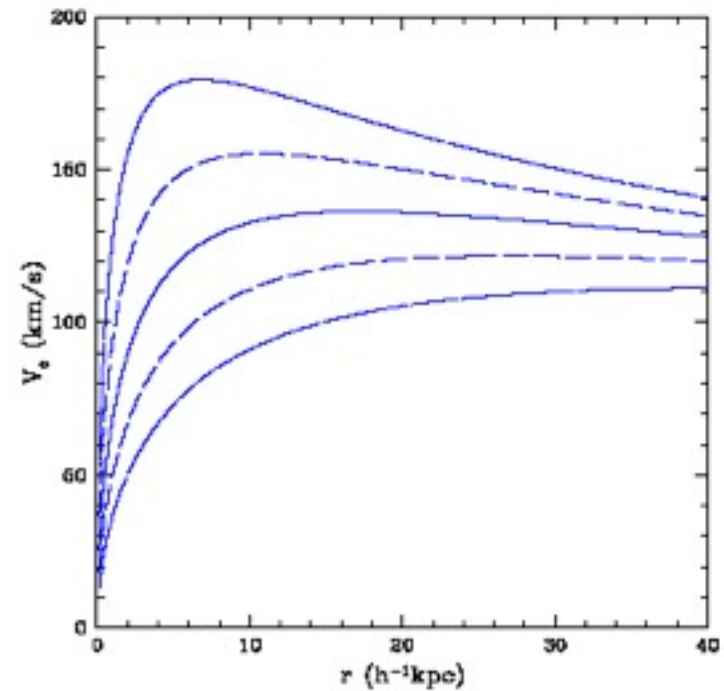


Figure 6. Concentrations versus environment. The concentration at  $z = 0$  of all haloes in the mass range  $0.5 - 1.0 \times 10^{12} h^{-1} M_{\odot}$  as a function of local density in units of the average density of the universe. The local density was determined within spheres of radius  $1 h^{-1} \text{Mpc}$ . The solid line represents the median  $c_{\text{vir}}$  value, the error bars are Poisson based on the number of haloes, and the dashed line indicates our best estimate of the intrinsic scatter.

# Spread of Halo Concentrations



**Figure 7.** The probability distributions of distinct haloes (solid line) and subhaloes (dashed line) at  $z = 0$  within the mass range  $(0.5 - 1.0) \times 10^{12} h^{-1} M_{\odot}$ . The simulated distributions (thick lines) include the  $\sim 2,000$  distinct haloes and  $\sim 200$  subhaloes within this mass range. Log-normal distributions with the same median and standard deviation as the measured distributions are shown (thin lines). Subhaloes are, on average, more concentrated than distinct haloes and they show a larger spread.



**Figure 8.** The spread in NFW rotation curves corresponding to the spread in concentration parameters for distinct haloes of  $3 \times 10^{11} h^{-1} M_{\odot}$  at  $z = 0$ . Shown are the median (solid),  $\pm 1\sigma$  (long dashed), and  $\pm 2\sigma$  (dot-dashed) curves. The corresponding median rotation curve for subhaloes is comparable to the upper  $1\sigma$  curve of distinct haloes.

# Evolution of Halo Concentration with Redshift

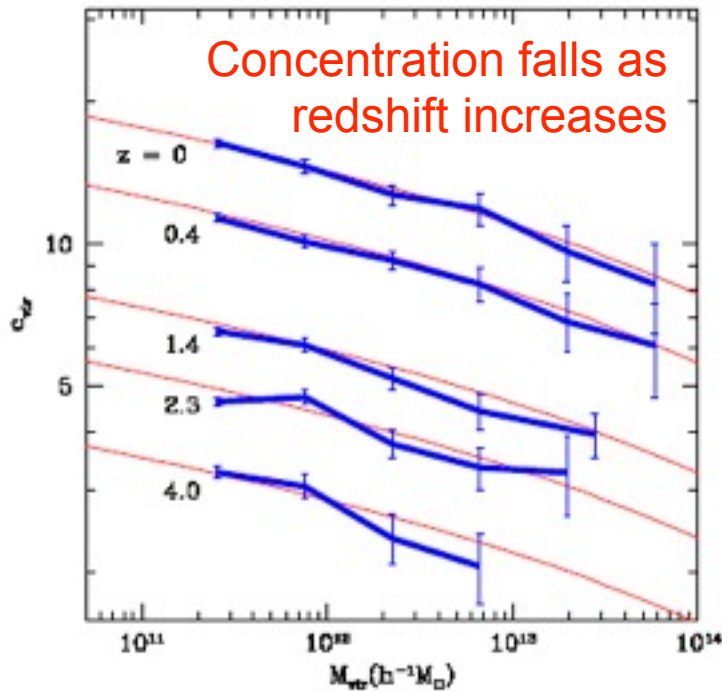


Figure 10. Median  $C_{vir}$  values as a function of  $M_{vir}$  for distinct haloes at various redshifts. The error bars are the Poisson errors due to the finite number of haloes in each mass bin. The thin solid lines show our toy model predictions.

$$C_{vir} \propto 1/(1+z)$$

at fixed mass

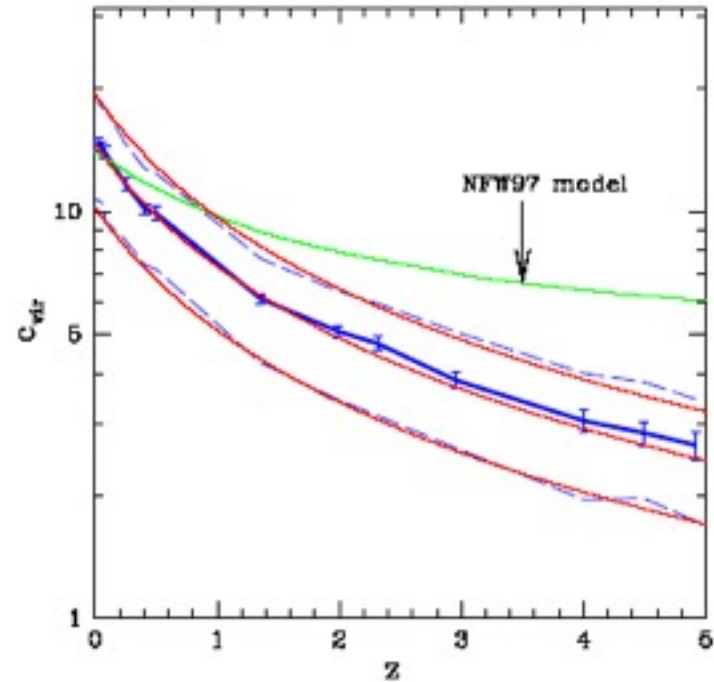
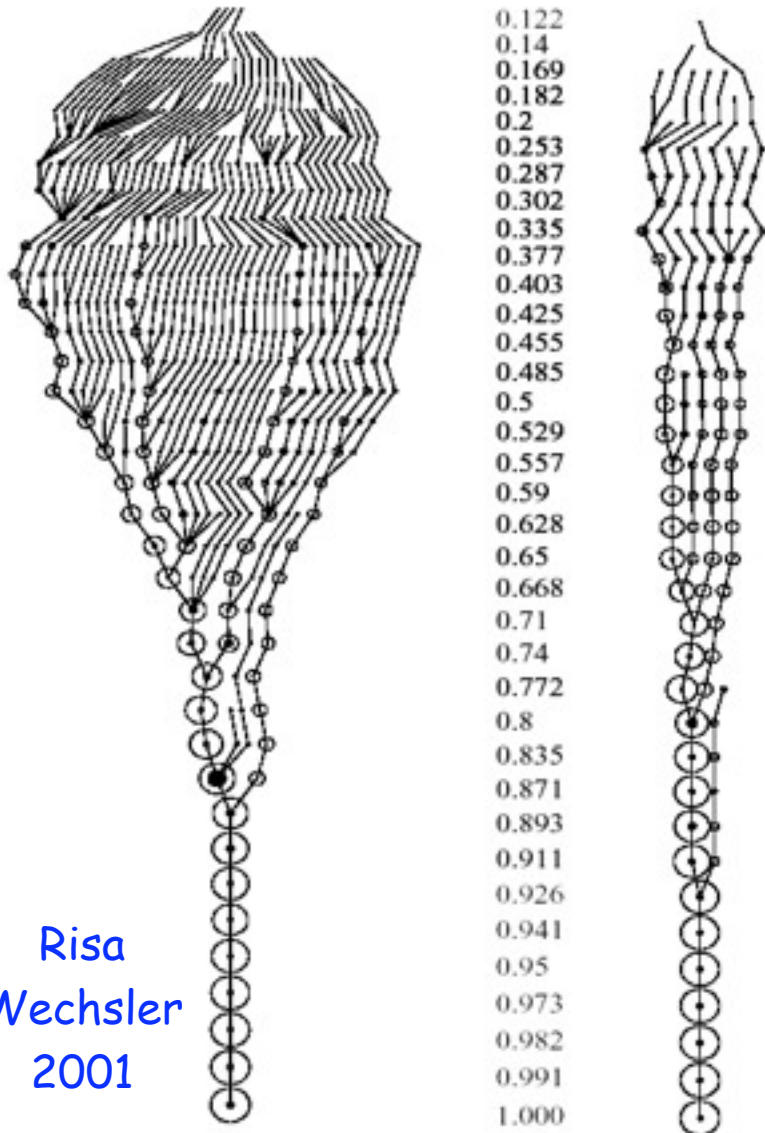


Figure 11. Concentration as a function of redshift for distinct haloes of a fixed mass,  $M_{vir} = 0.5 - 1.0 \times 10^{12} h^{-1} M_{\odot}$ . The median (heavy solid line) and intrinsic 68% spread (dashed line) are shown. The behavior predicted by the NFW97 toy model is marked. Our revised toy model for the median and spread for  $8 \times 10^{11} h^{-1} M_{\odot}$  haloes (thin solid lines) reproduces the observed behavior rather well.

# Merger Trees



Risa  
Wechsler  
2001

Based on our ART simulations, Wechsler created the first structural merger trees tracing the merging history of thousands of halos with structural information on their higher-redshift progenitors, including their radial profiles and spins. This led to the discovery that a halo's merging history can be characterized by a single parameter  $a_c$  which describes the scale factor at which the halo's mass accretion slows, and that this parameter correlates very well with the halo concentration, thus showing that the distribution of dark matter halo concentrations reflects mostly the distribution of their mass accretion rates. We found that the radius of the inner part of the halo, where the density profile is roughly  $1/r$ , is established during the early, rapid-accretion phase of halo growth (a result subsequently confirmed and extended by other groups, e.g., Zhao et al. 2003, Reed et al. 2004).

$$\rho_{\text{NFW}}(r) = \frac{\rho_s}{(r/R_s)(1+r/R_s)^2}, \quad (1)$$

where  $R_s$  is a characteristic ‘‘inner’’ radius, and  $\rho_s$  a corresponding inner density. One of the inner parameters can be replaced by a ‘‘virial’’ parameter, either the virial radius ( $R_{\text{vir}}$ ), mass ( $M_{\text{vir}}$ ), or velocity ( $V_{\text{vir}}$ ), defined such that the mean density inside the virial radius is  $\Delta_{\text{vir}}$  times the mean universal density  $\rho_u$  at that redshift:

$$M_{\text{vir}} \equiv \frac{4\pi}{3} \Delta_{\text{vir}} \rho_u R_{\text{vir}}^3. \quad (2)$$

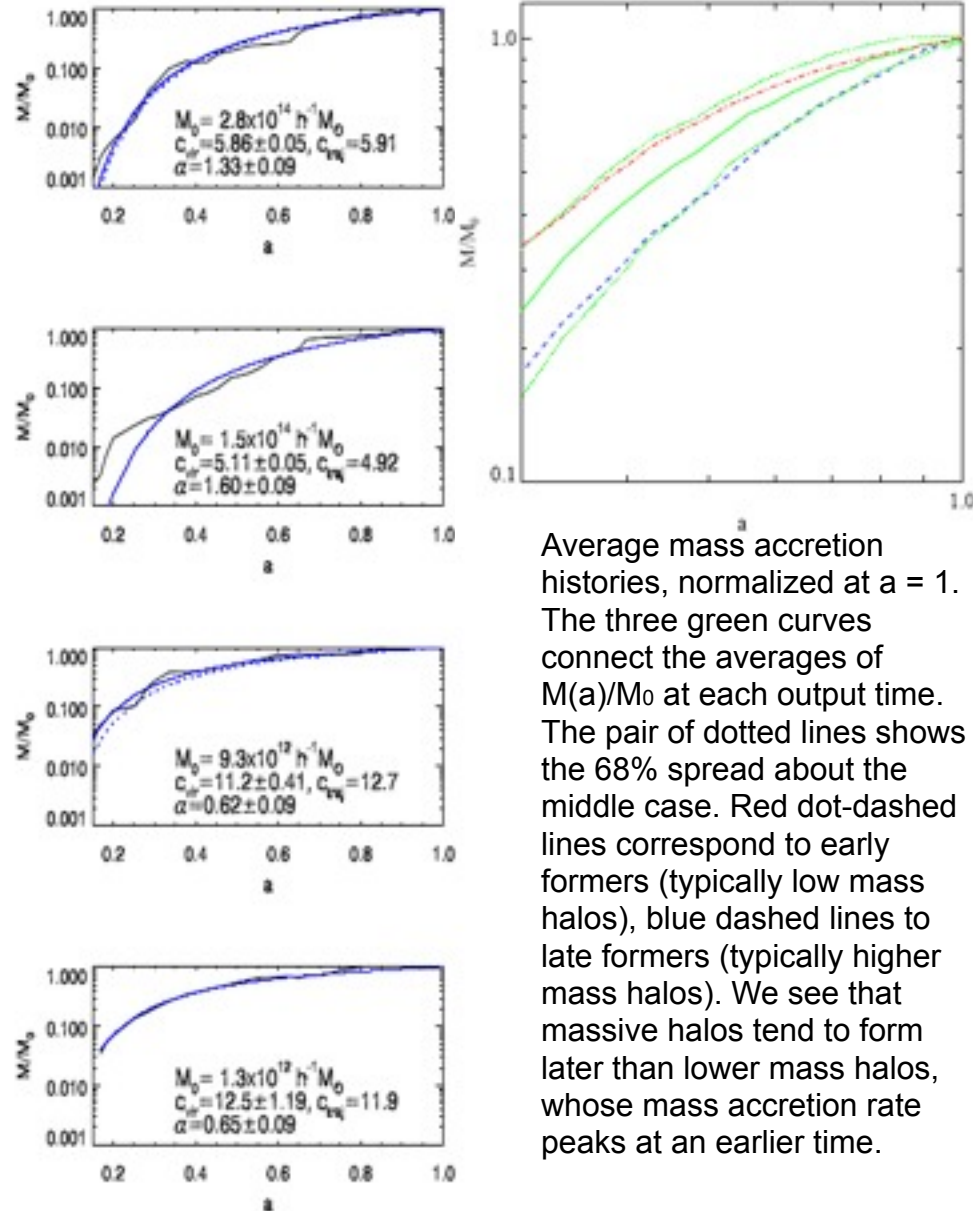
The critical overdensity at virialization,  $\Delta_{\text{vir}}$ , is motivated by the spherical collapse model; it has a value  $\simeq 180$  for the Einstein-deSitter cosmology, and  $\simeq 340$  for the  $\Lambda$ CDM cosmology assumed here. A useful alternative parameter for describing the shape of the profile is the concentration parameter  $c_{\text{vir}}$ , defined as  $c_{\text{vir}} \equiv R_{\text{vir}}/R_s$ .

(Bryan & Norman 1998)  $\Delta_{\text{vir}} \simeq (18\pi^2 + 82x - 39x^2)/\Omega(z)$  where  $x \equiv \Omega(z) - 1$ .

By examining a range of full mass assembly histories for our sample of halos, we have found a useful parameterized form that captures many essential aspects of halo growth over time. Remarkably, we find that both average mass accretion histories and mass accretion histories for individual halos, as observed at  $z = 0$ , can be characterized by a simple function:

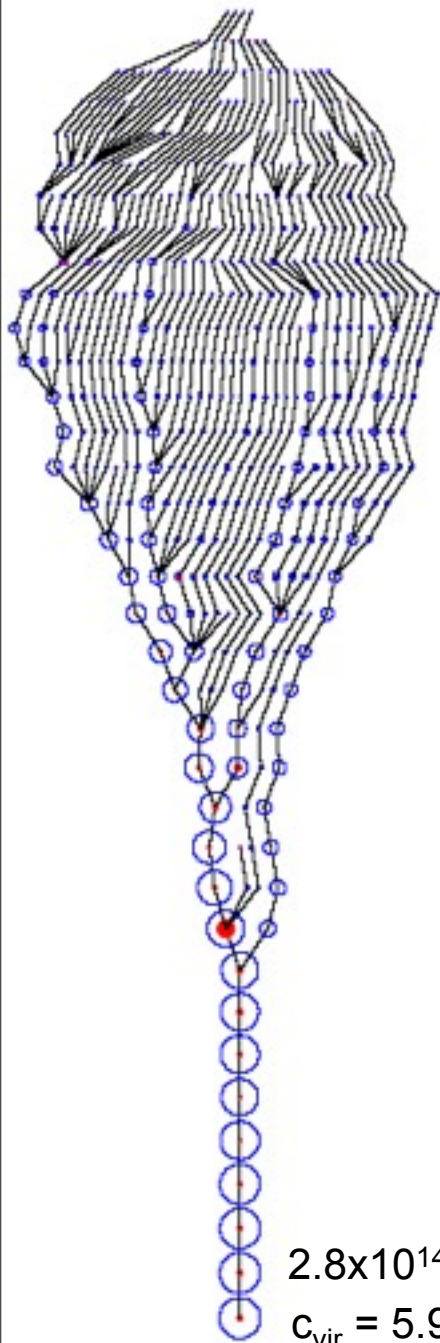
$$M(a) = M_0 e^{-\alpha z}, \quad a = (1+z)^{-1}. \quad (3)$$

The single free parameter in the model,  $\alpha$ , can be related to a characteristic epoch for formation,  $a_c$ , defined as the expansion scale factor  $a$  when the logarithmic slope of the accretion rate,  $d \log M/d \log a$ , falls below some specified value,  $S$ . The functional form defined in Eq. 3 implies  $a_c = \alpha/S$ . In what follows we have chosen  $S = 2$ .



Average mass accretion histories, normalized at  $a = 1$ . The three green curves connect the averages of  $M(a)/M_0$  at each output time. The pair of dotted lines shows the 68% spread about the middle case. Red dot-dashed lines correspond to early formers (typically low mass halos), blue dashed lines to late formers (typically higher mass halos). We see that massive halos tend to form later than lower mass halos, whose mass accretion rate peaks at an earlier time.

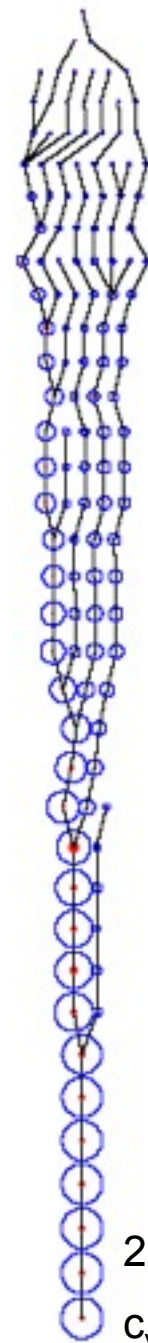




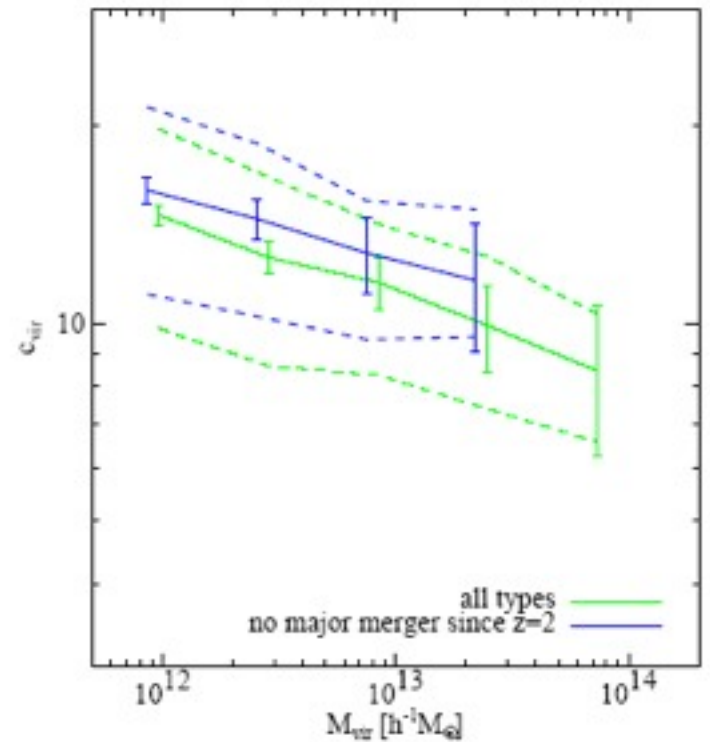
Structural merger trees for two halos. The radii of the outer and inner (filled) circles are proportional to the virial and inner NFW radii,  $R_{\text{vir}}$  and  $R_s$ , respectively, scaled such that the two halos have equal sizes at  $a = 1$ . Lines connect halos with their progenitor halos.

$2.8 \times 10^{14} M_{\text{sun}}/h$   
 $c_{\text{vir}} = 5.9$

a ↓  
 0.122  
 0.14  
 0.169  
 0.182  
 0.2  
 0.253  
 0.287  
 0.302  
 0.335  
 0.377  
 0.403  
 0.425  
 0.455  
 0.485  
 0.5  
 0.529  
 0.557  
 0.59  
 0.628  
 0.65  
 0.668  
 0.71  
 0.74  
 0.772  
 0.8  
 0.835  
 0.871  
 0.893  
 0.911  
 0.926  
 0.941  
 0.95  
 0.973  
 0.982  
 0.991  
 1.000



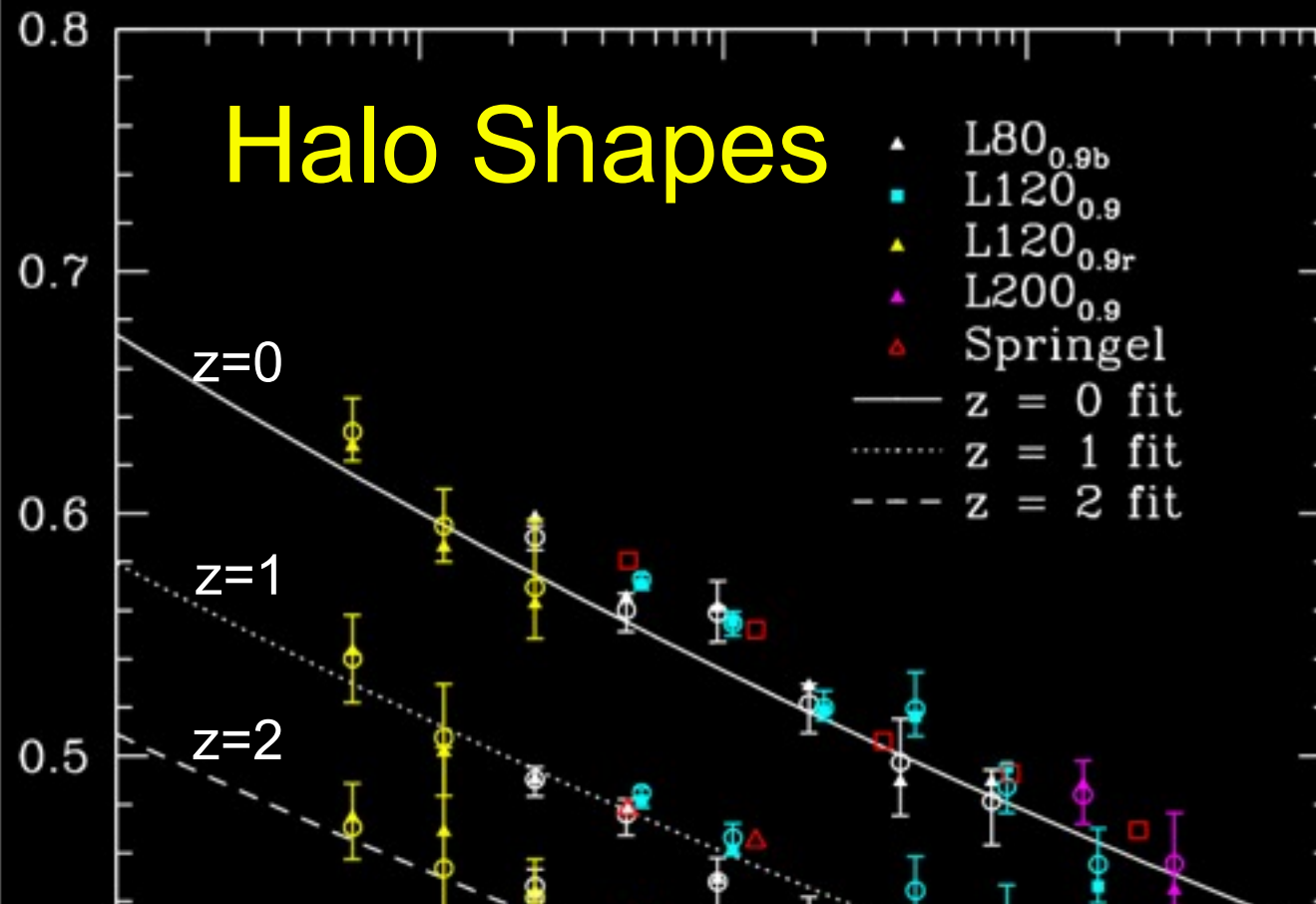
$2.9 \times 10^{12} M_{\text{sun}}/h$   
 $c_{\text{vir}} = 12.5$



For halos without recent mergers,  $c_{\text{vir}}$  is higher and the scatter is reduced to  $\log c_{\text{vir}} \approx 0.10$ .

Wechsler et al. 2002

# Halo Shapes



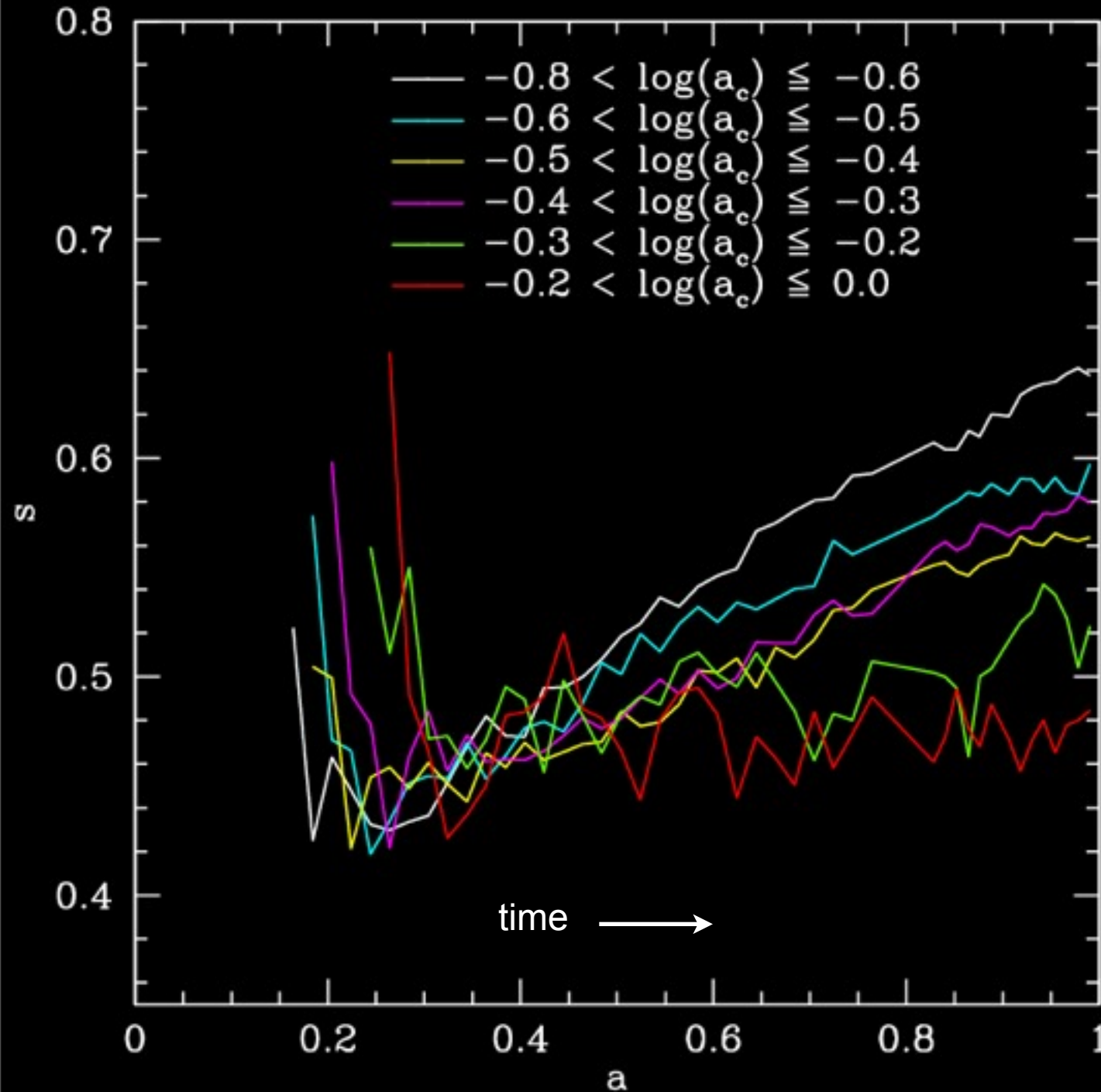
$\langle s \rangle$  = short / long axis of dark halos vs. mass and redshift. Dark halos are more elongated the more massive they are and the earlier they form. We found that the halo  $\langle s \rangle$  scales as a power-law in  $M_{\text{halo}}/M^*$ . Halo shape is also related to the Wechsler halo formation scale factor  $a_c$ .

A simple formula describes these results, as well dependence on epoch and cosmological parameter  $\sigma_8$  :

$$\langle s \rangle (M_{\text{vir}}, z = 0) = \alpha \left( \frac{M_{\text{vir}}}{M_*} \right)^\beta$$

with best fit values

$$\alpha = 0.54 \pm 0.03, \quad \beta = -0.050 \pm 0.003.$$



Halo shape  $s = c / a$  vs. scale factor  $a = 1 / (1 + \text{redshift})$  for halos of mass between  $3.2$  and  $6.4 \times 10^{12} M_{\text{sun}}$  that form at different scale factors  $a_c$ . Halos become more spherical after they form, and those that form earlier (at lower  $a_c$ ) become more spherical faster.

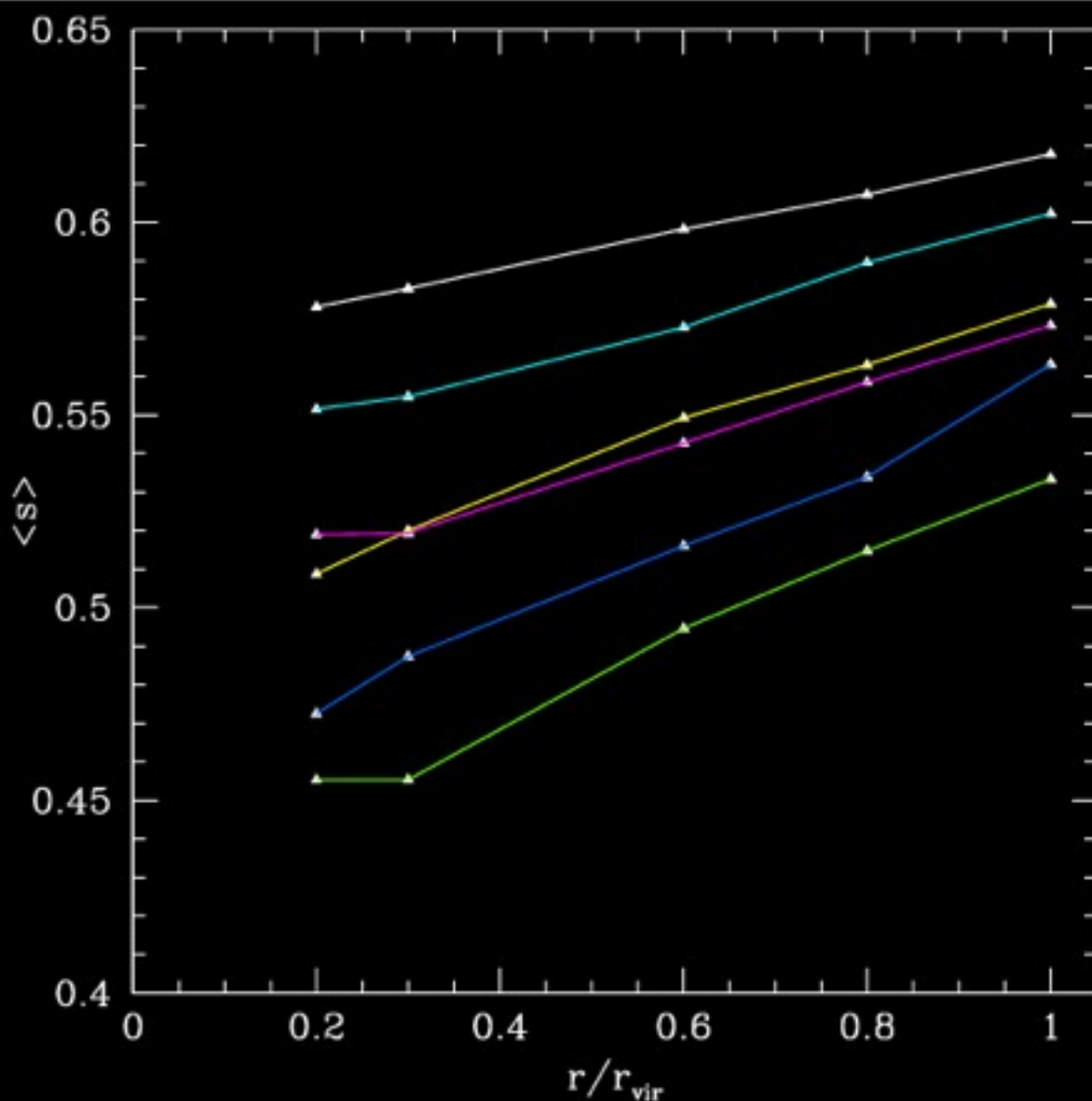
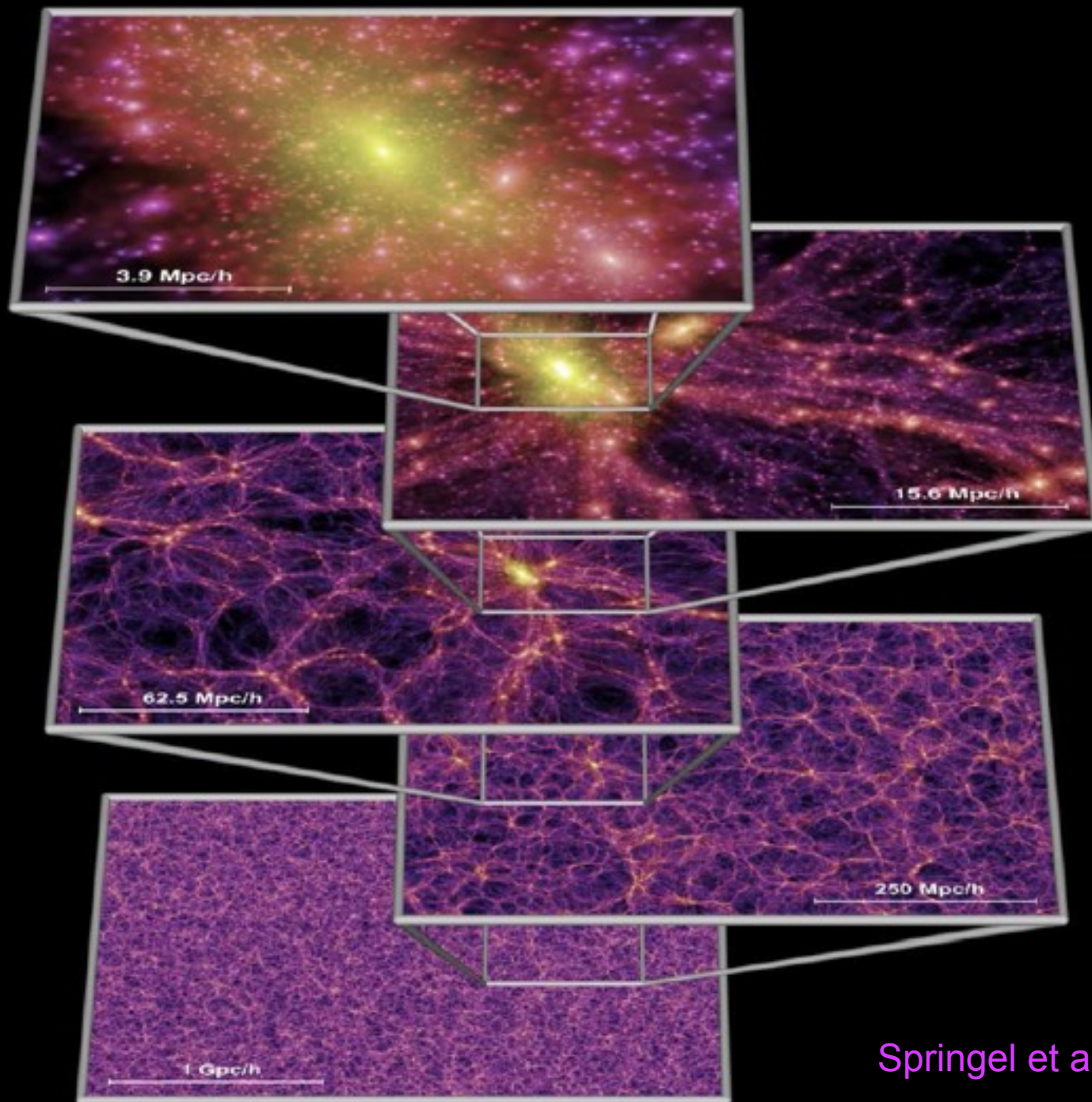


FIG. 7.—  $\langle s \rangle$  with radius at  $z = 0$ . black:  $1.6 \times 10^{12} < M < 3.2 \times 10^{12}$ , red:  $3.2 \times 10^{12} < M < 6.4 \times 10^{12}$ , blue:  $6.4 \times 10^{12} < M < 1.28 \times 10^{13}$ , green:  $1.28 \times 10^{13} < M < 2.56 \times 10^{13}$ , orange:  $2.56 \times 10^{13} < M < 5.12 \times 10^{13}$ , violet:  $5.12 \times 10^{13} < M$ . These are the same mass bins as in Figure 3.

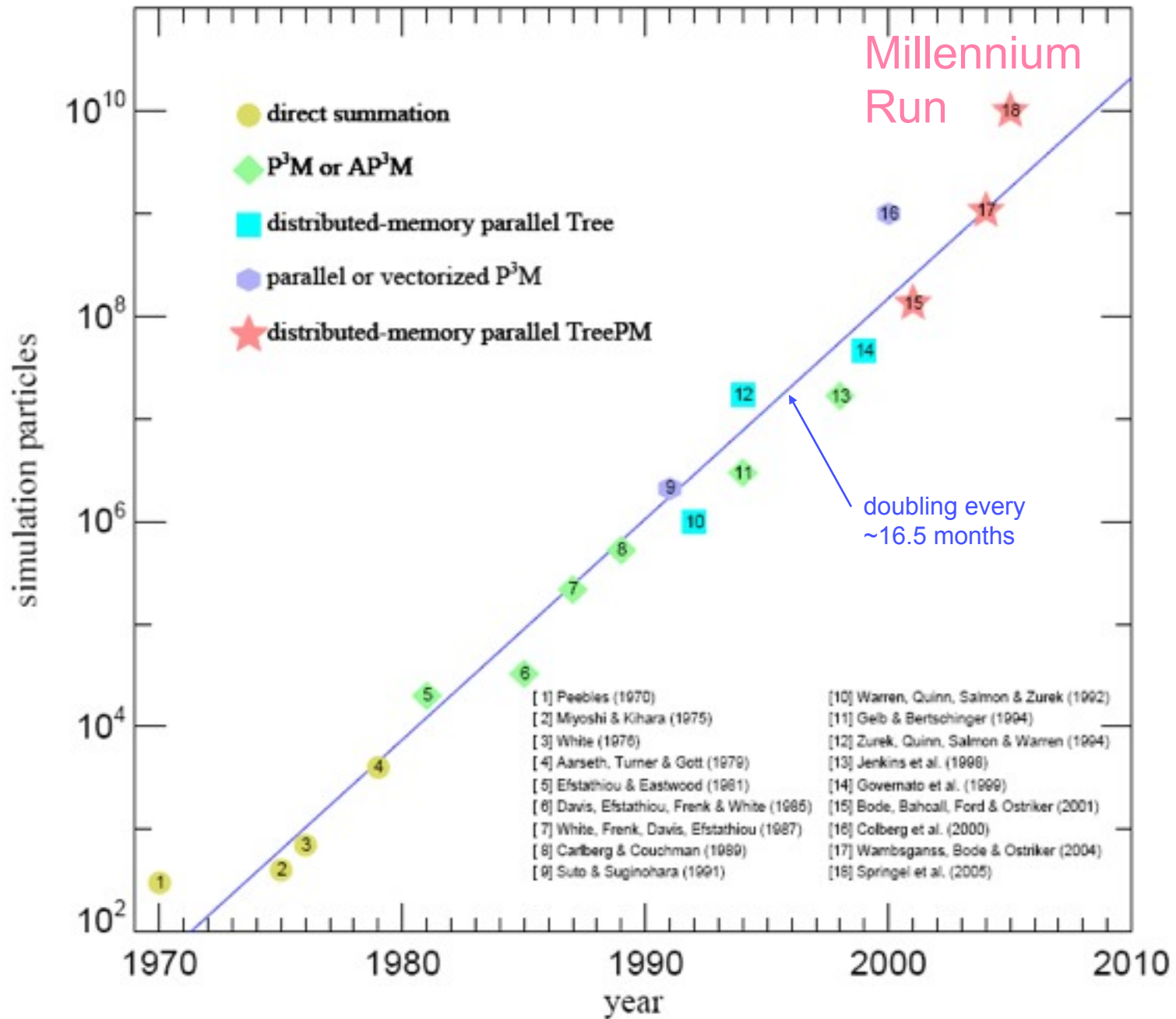
Halos become more spherical at larger radius and smaller mass. As before,  $s$  = short / long axis. These predictions can be tested against cluster X-ray data and galaxy weak lensing data.

[These figures are from Brandon Allgood's PhD dissertation.]

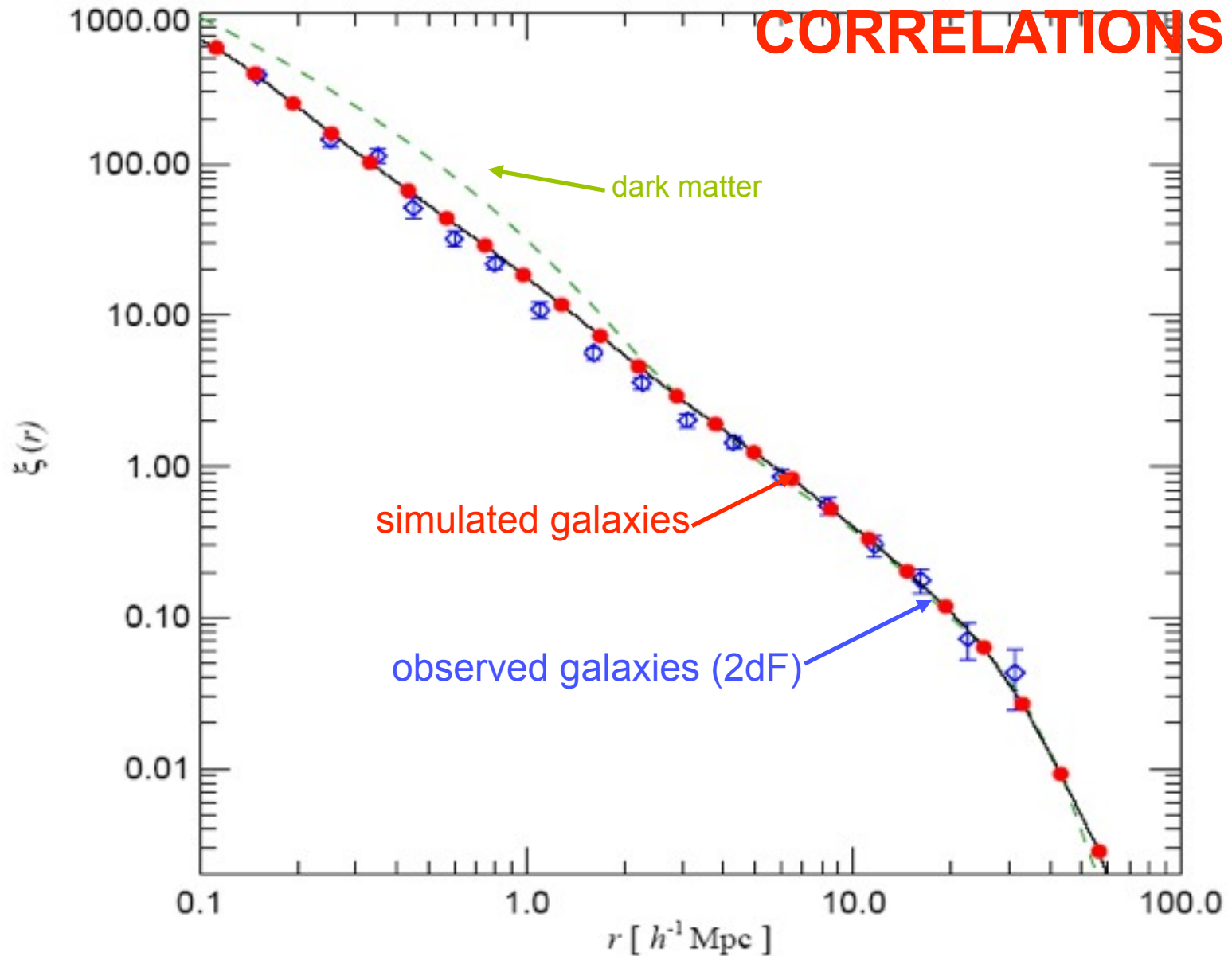


Springel et al. 2005

# Particle number in cosmological N-body simulations vs. pub date

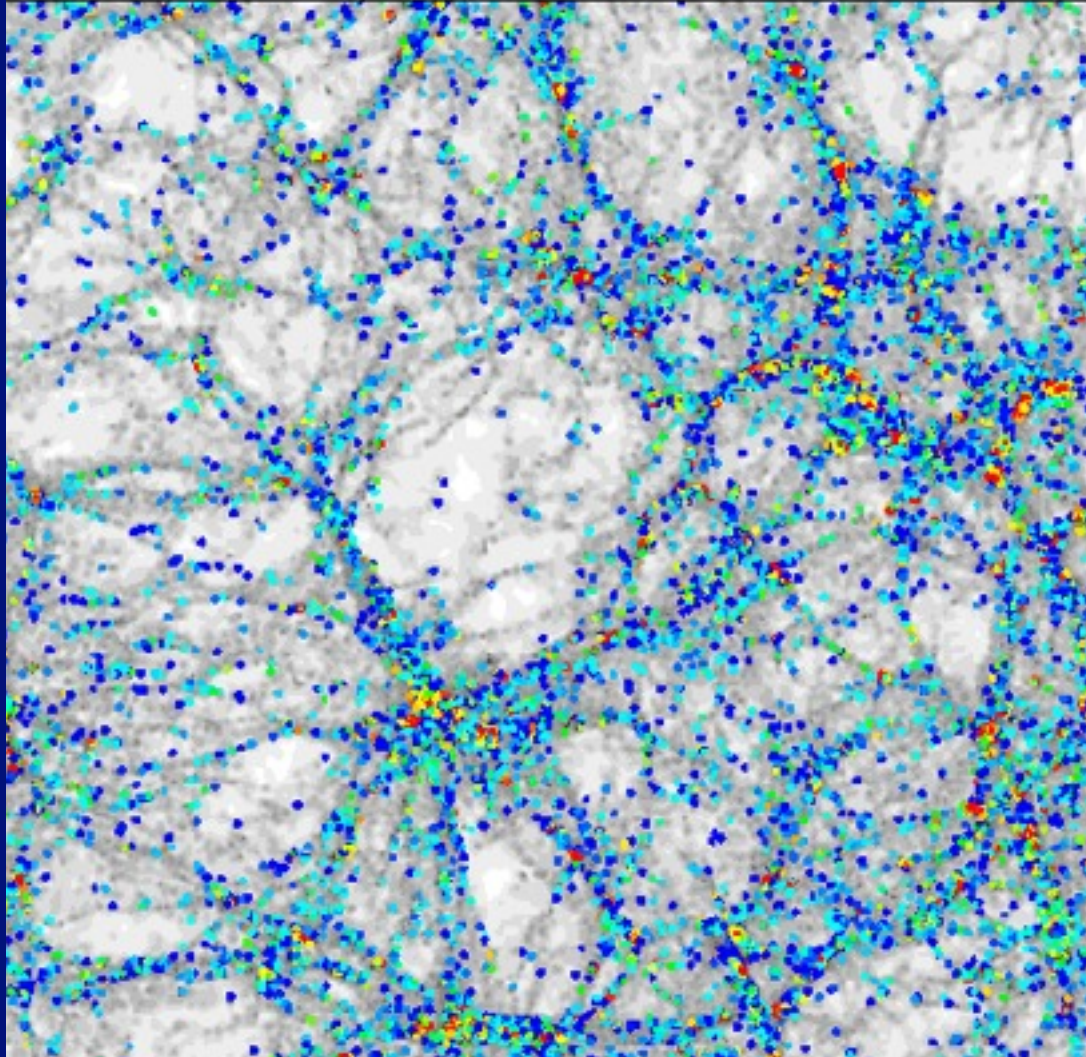


# UNDERSTANDING GALAXY CORRELATIONS



Galaxy 2-point correlation function at the present epoch.

# Galaxy type correlated with large scale structure



elliptical

elliptical

bulge+disk

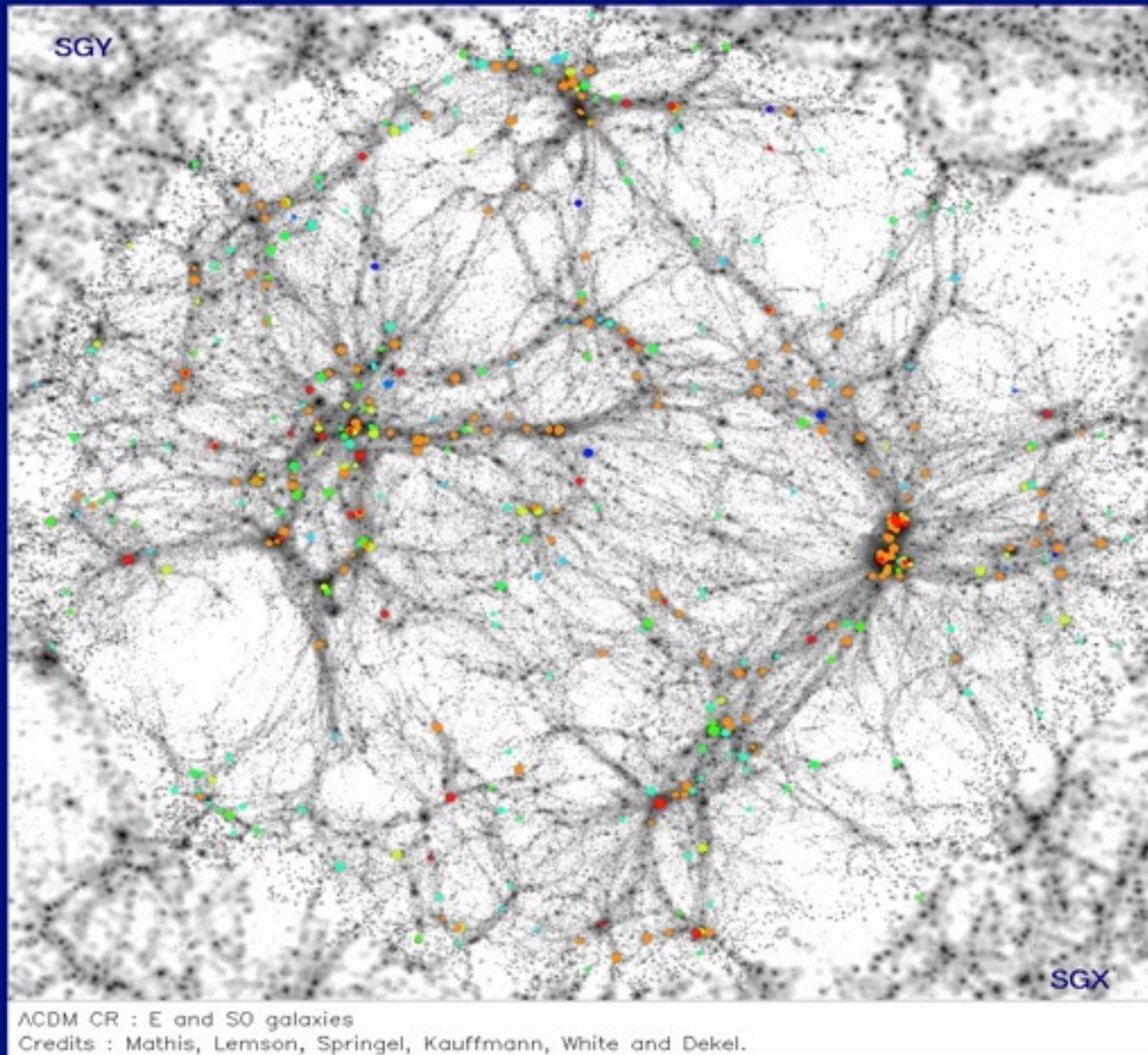
disk

Semi-Analytic  
Modeling

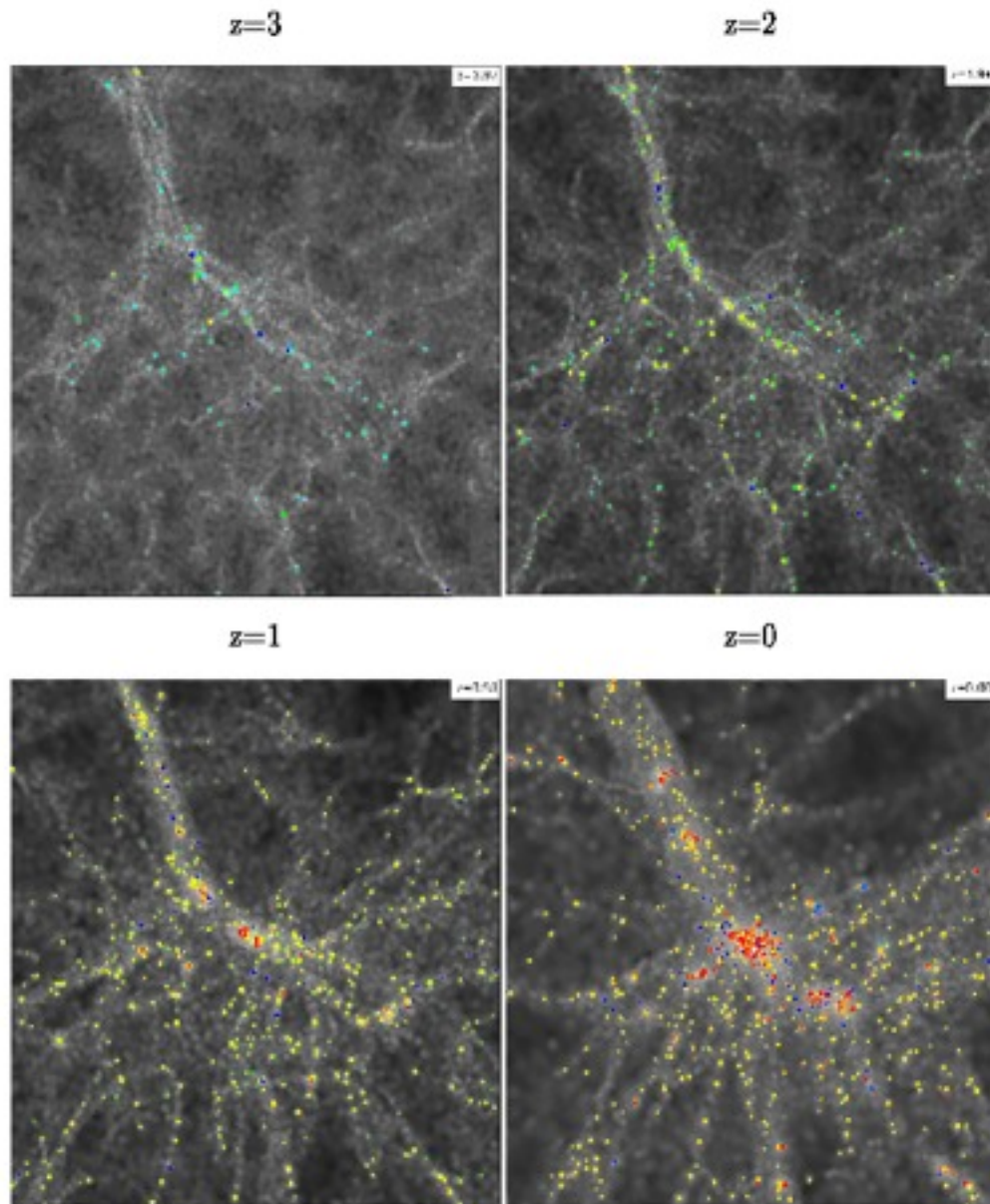
Kauffmann et al.



# Elliptical galaxies in clusters in the local universe



# Formation of galaxies in a cluster



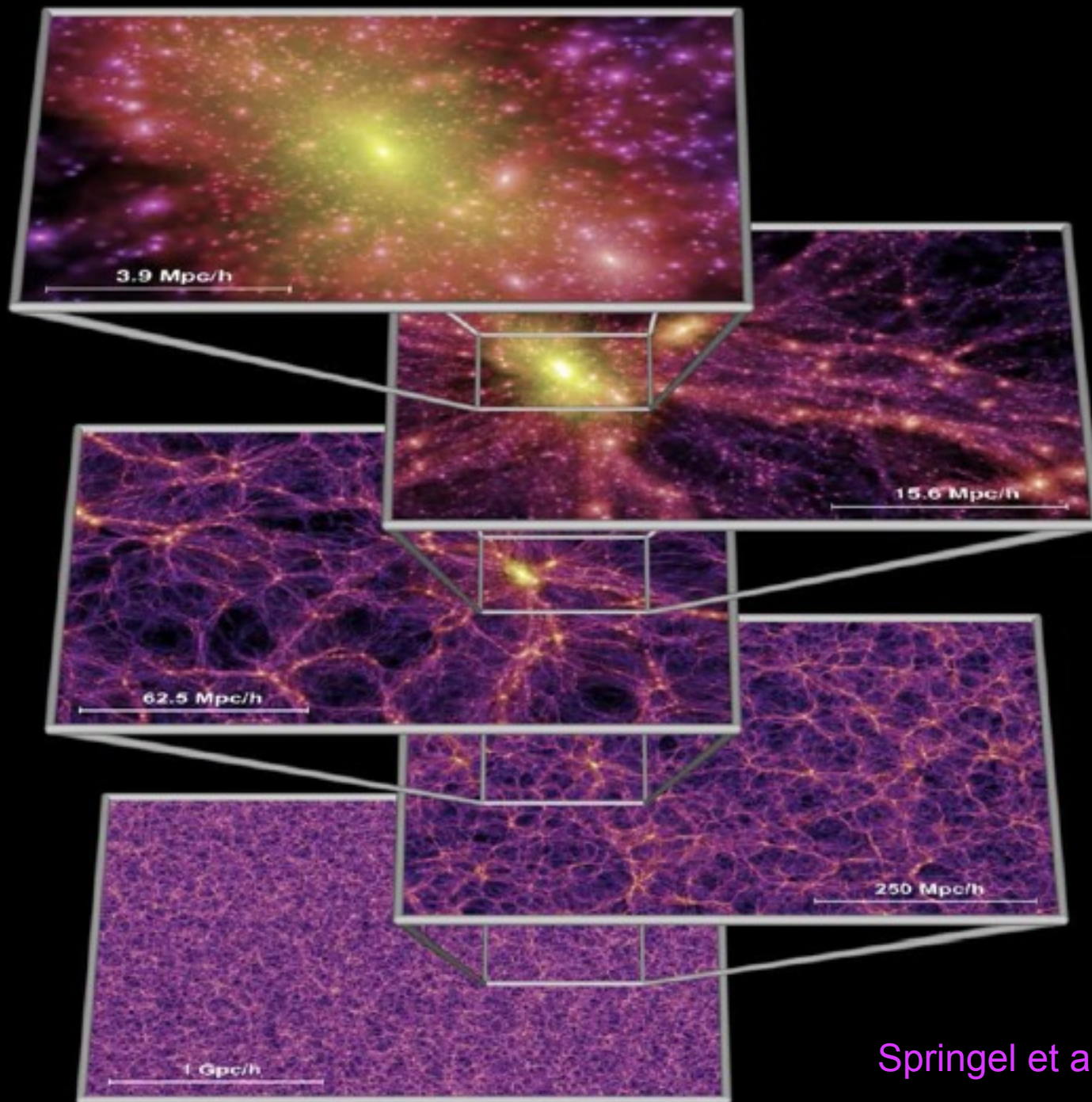
A visualization of the Millennium Simulation, showing a complex, interconnected network of dark purple and blue filaments and nodes, representing the large-scale structure of the universe. The filaments form a dense, web-like pattern, with nodes representing galaxy clusters and groups. The overall appearance is that of a highly structured, hierarchical distribution of matter.

1 Gpc/h

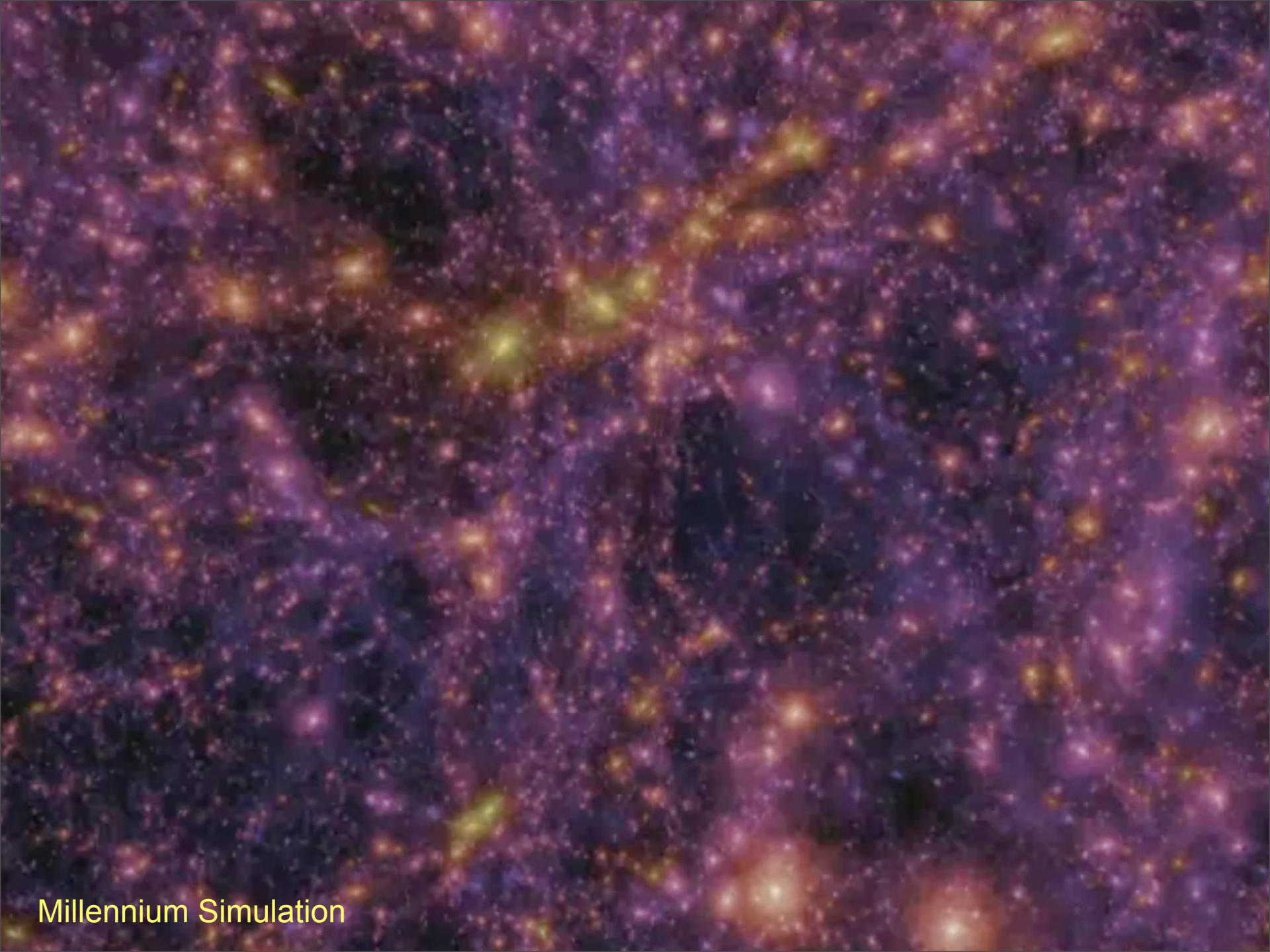
**Millennium Simulation**

10,077,696,000 particles

( $z = 0$ )



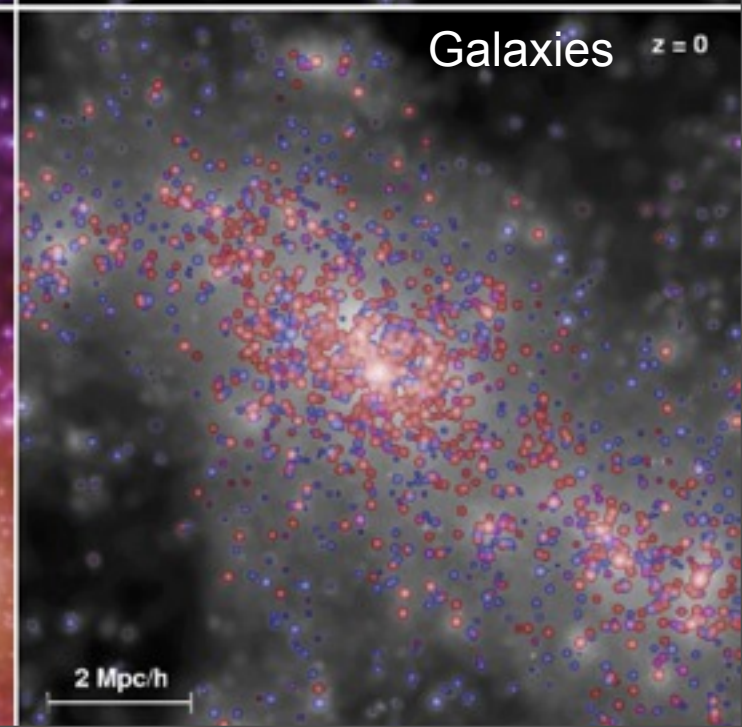
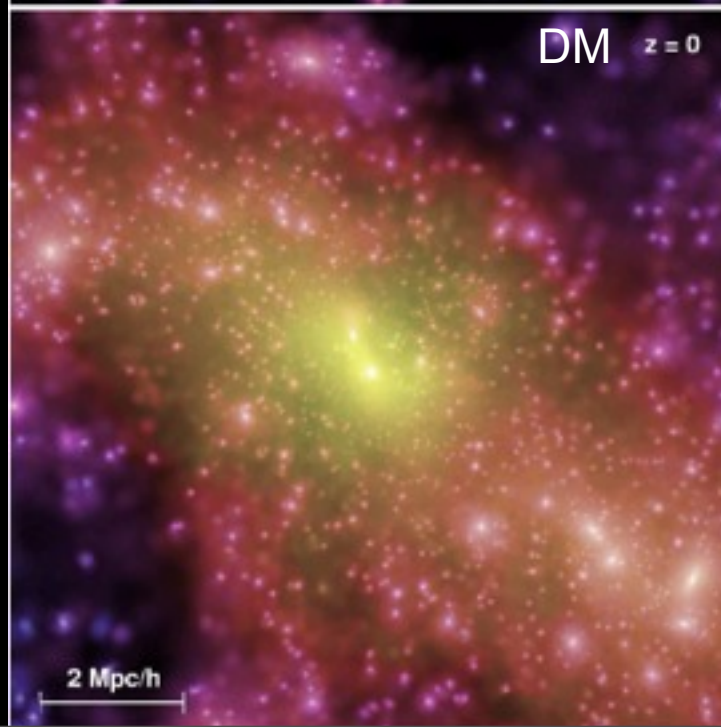
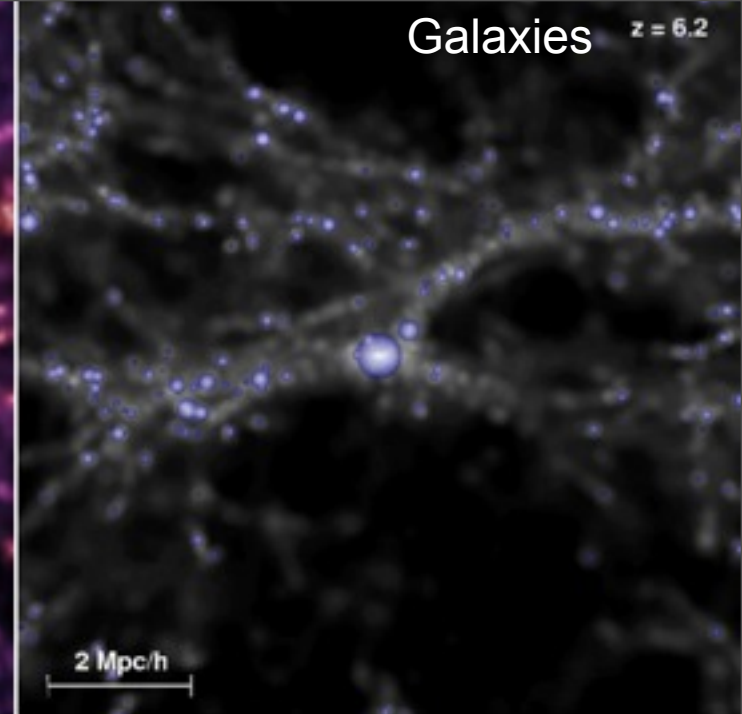
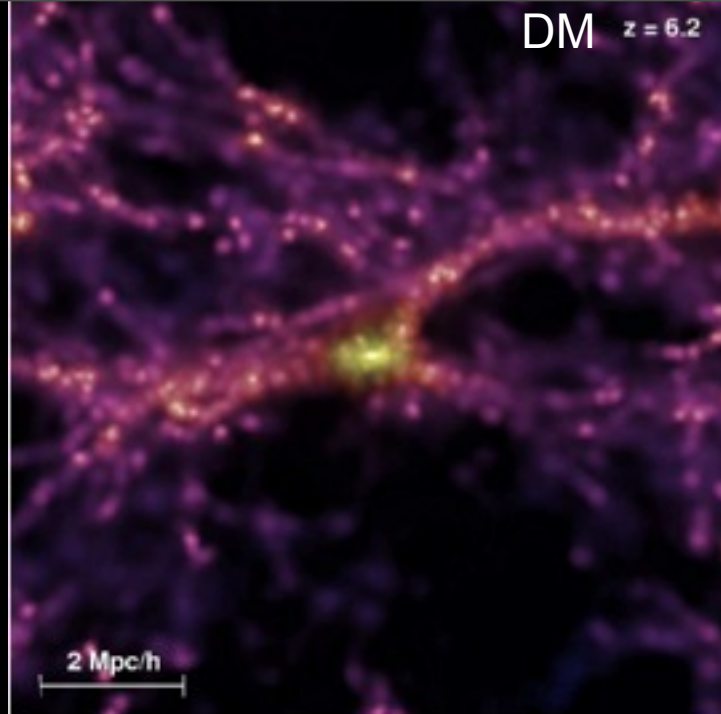
Springel et al. 2005



Millennium Simulation

Environment of a 'first quasar candidate' at high and low redshifts. The two panels on the left show the projected dark matter distribution in a cube of comoving sidelength  $10h^{-1}$  Mpc, colourcoded according to density and local dark matter velocity dispersion. The panels on the right show the galaxies of the semi-analytic model overlaid on a gray-scale image of the dark matter density. The volume of the sphere representing each galaxy is proportional to its stellar mass, and the chosen colours encode the restframe stellar  $B-V$  colour index. While at  $z = 6.2$  (top) all galaxies appear blue due to ongoing star formation, many of the galaxies that have fallen into the rich cluster at  $z = 0$  (bottom) have turned red.

Springel et al. 2005



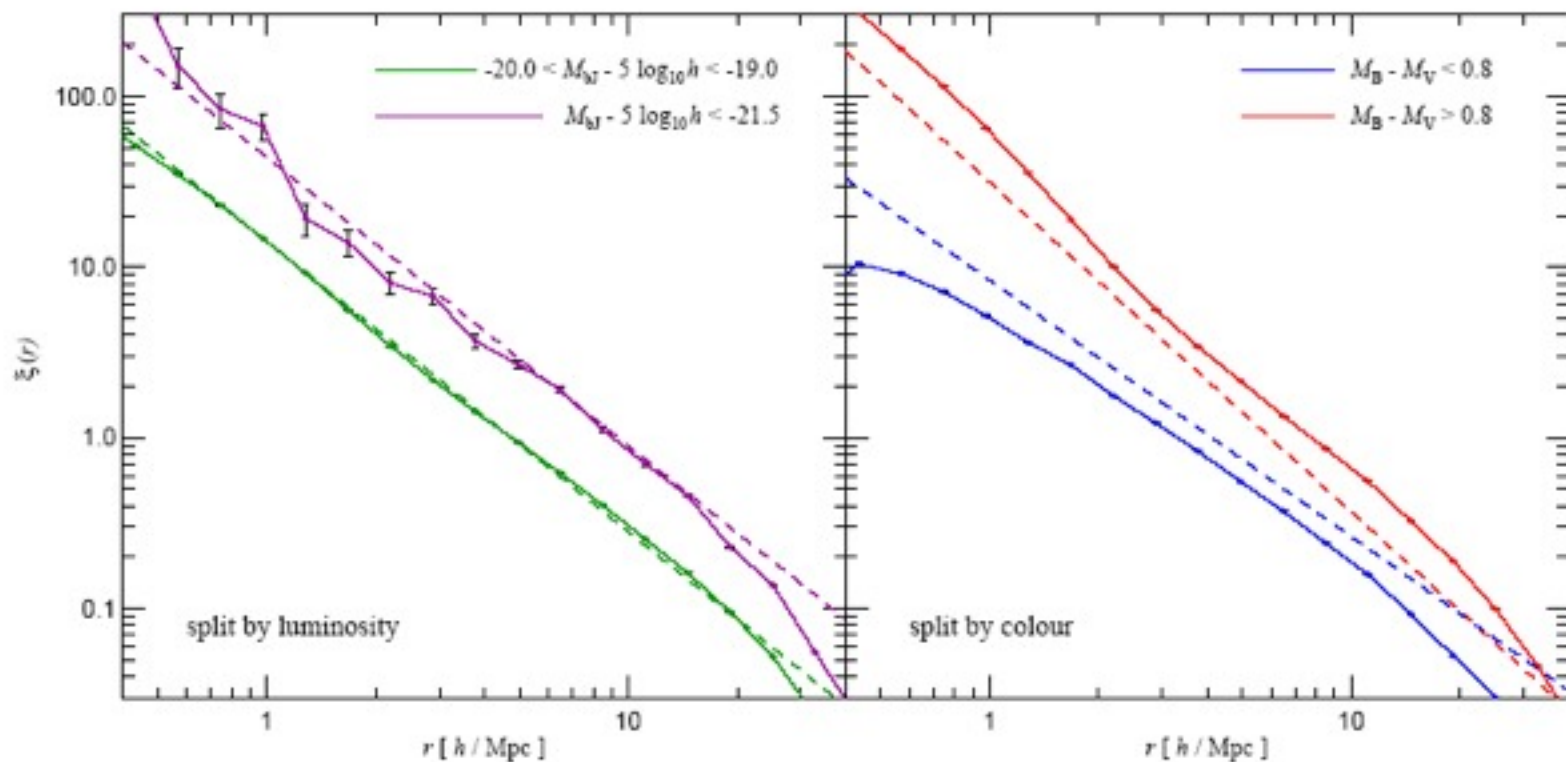


**Figure 5:** Galaxy clustering as a function of luminosity and colour. In the panel on the left, we show the 2-point correlation function of our galaxy catalogue at  $z = 0$  split by luminosity in the bJ-band (symbols). Brighter galaxies are more strongly clustered, in quantitative agreement with observations<sup>33</sup> (dashed lines). Splitting galaxies according to colour (right panel), we find that red galaxies are more strongly clustered with a steeper correlation slope than blue galaxies. Observations<sup>35</sup> (dashed lines) show a similar trend, although the difference in clustering amplitude is smaller than in this particular semi-analytic model.

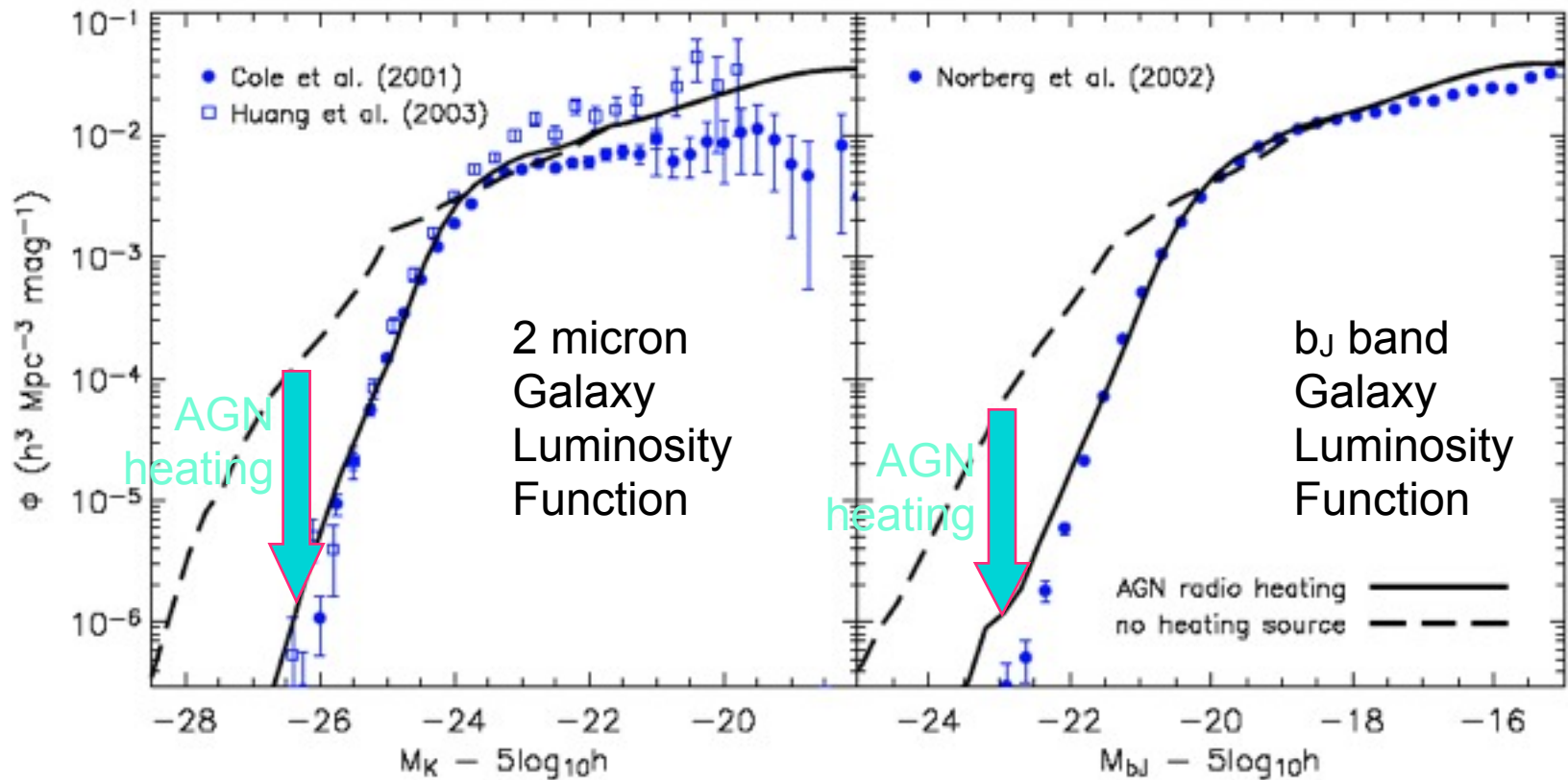


**Figure 8.** Galaxy luminosity functions in the K (left) and  $b_J$  (right) photometric bands, plotted with and without ‘radio mode’ feedback (solid and long dashed lines respectively – see Section 3.4). Symbols indicate observational results as listed in each panel. As can be seen, the inclusion of AGN heating produces a good fit to the data in both colours. Without this heating source our model overpredicts the luminosities of massive galaxies by about two magnitudes and fails to reproduce the sharp bright end cut-offs in the observed luminosity functions.

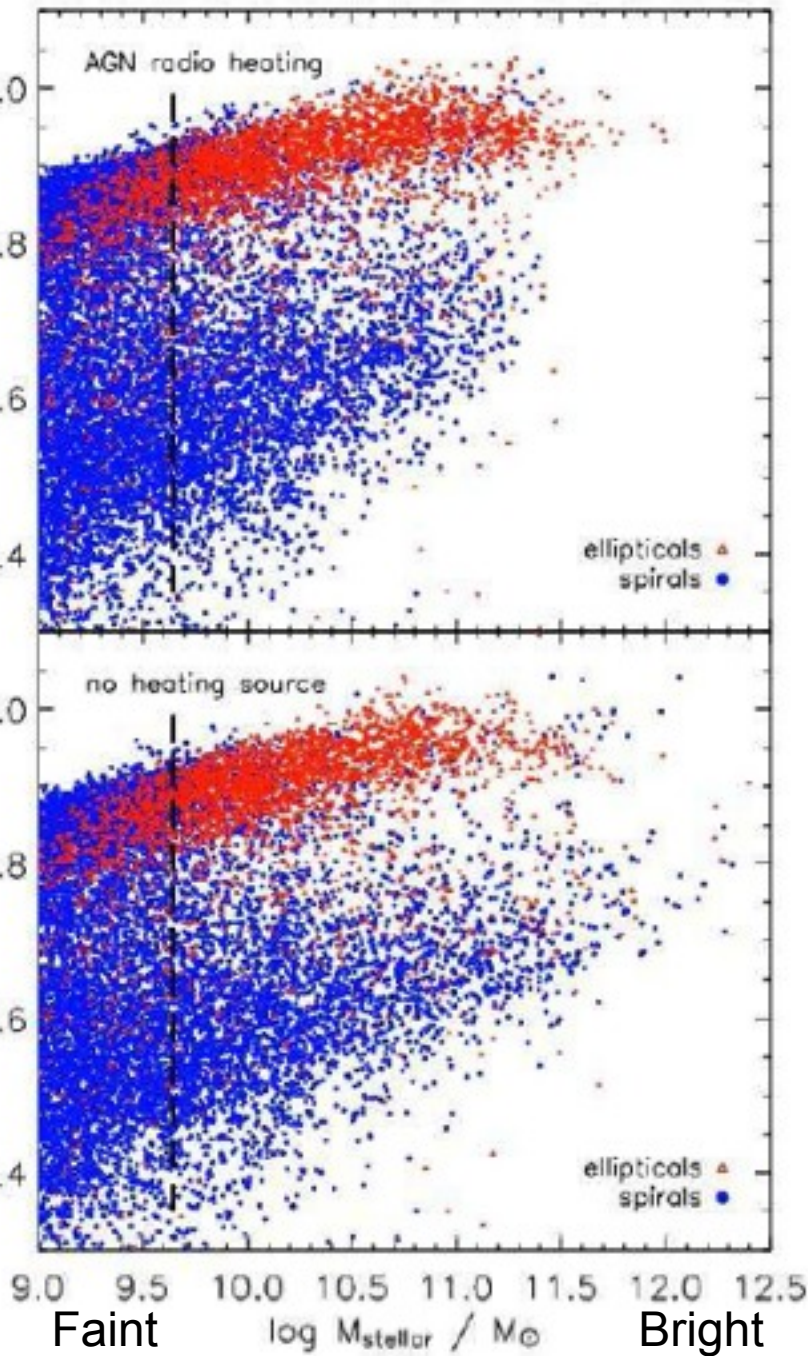


Red

Blue

Red

Blue



## Color Magnitude Diagram

With AGN heating – brightest galaxies are red, as observed

Without heating – brightest galaxies are blue

Croton et al. 2006

(see also Cattaneo et al. 2006)